8-2009

Multiscale Modeling of the Electronic, Optical, and Magnetic Properties of Low-dimensional Metal Systems

Ke Zhao
University of Tennessee - Knoxville

To the Graduate Council:

I am submitting herewith a dissertation written by Ke Zhao entitled "Multiscale Modeling of the Electronic, Optical, and Magnetic Properties of Low-dimensional Metal Systems." I have examined the final electronic copy of this dissertation for form and content and recommend that it be accepted in partial fulfillment of the requirements for the degree of Doctor of Philosophy, with a major in Physics.

Zhenyu Zhang, Major Professor

We have read this dissertation and recommend its acceptance:

Adolfo Eguiluz, Hanno Weitering, Robert Compton

Accepted for the Council:

Carolyn R. Hodges

Vice Provost and Dean of the Graduate School

(Original signatures are on file with official student records.)

To the Graduate Council:

I am submitting herewith a dissertation written by Ke Zhao entitled "Multiscale Modeling of the Electronic, Optical, and Magnetic Properties of Low-dimensional Metal Systems." I have examined the final electronic copy of this dissertation for form and content and recommend that it be accepted in partial fulfillment of the requirements for the degree of Doctor of Philosophy, with a major in Physics.

Zhenyu Zhang, Major Professor

We have read this dissertation
and recommend its acceptance:

Adolfo Eguiluz

Hanno Weitering

Robert Compton

Accepted for the Council:

Carolyn R. Hodges

Vice Provost and Dean of the Graduate School

Multiscale Modeling of the Electronic, Optical, and Magnetic Properties of Low-dimensional Metal Systems

A Dissertation

Presented for the

Doctor of Philosophy

Degree

The University of Tennessee, Knoxville

Ke Zhao

August 2009

Dedication

To My Parents

Acknowledgements

My deepest appreciation should go to my Ph.D advisor, Professor Zhenyu Zhang, for his great guidance and enourmous inspirations. His physical insight and unique way of solving physical problems will definitely make a great impact to my future research work. But what I benefited from Prof. Zhang is not only how to solve physical problems, but more generally how to persistently approach the ultimate goal of any kind. The fact that Prof. Zhang is willing to face the challenges that look impossible to many others will always inspire me to conquer any difficulties.

I also appreciate my collaborators:

Prof. Hongxing Xu, who gave me detailed directions on my very first project. As an expert in surface-enhanced Raman scattering (SERS) and surface plasmon, Prof. Xu quickly led me into the frontier of these two highly related fields;

Dr. Bo Persson, who instructed me in two different fields: SERS and contact mechanics. Dr. Persson's creativity in developing beautiful analytic models are very enlighening to my research.

Dr. Claudia Troparevsky, who helped me heavily with the electronic structure study of nanostructures with density functional theory (DFT). When I have difficuties in DFT, I can always reliably seek for help from Dr. Troparevsky;

Dr. Di Xiao, who has discussed with me on many details of the physical pictures related to electronic structure of low-dimensional systems;

Prof. Adolfo Eguiluz, who likes to raise interesting questions very enlightening to my research.

Dr. Baohua Gu, who is an experimentalist on SERS. Through the discussion with Dr. Gu, I got direct feelings on how SERS works in the laboratory.

Prof. Robert Compton, who is also an experimentalist on SERS and had quite some discussions with me in this field.

In addition, I want to thank my doctoral committee members for their directions.

My gratitude also extends to all the other faculty members, staff, fellow graduate students and group members, who helped make my five and a half years at the University of Tennessee a great time.

Finally, special thanks are due to my parents, who inspired me to complete my journey of Ph.D study when I nearly lost confidence.

Abstract

This thesis presents a study of the electronic, optical and magnetic properties of low-dimensional metal systems across multiple scales, using a variety of theoretical techniques including microscopic phenomenological model, *ab initio* density functional theory (DFT) and classical electromagnetics.

In the study of the interaction between a molecule and metal substrate, a new mechanism of the chemical enhancement for surface-enhanced Raman scattering (SERS) was discovered. Through a microscopic phenomenological model, it has been demonstrated that 10^2-10^4 chemical enhancement may originate from the coupling between an electric field *parallel* to the surface of a metal substrate and the perpendicular vibration mode of the Raman active molecule adsorbed on the substrate.

When extended to aggregates of metal nanostructures, the electronic coupling between two nanoparticles was studied using DFT with real atoms. It has been shown that when the two nanoparticles are separated from touching contact, the dimer undergoes a bond-breaking step, which establishes the striking existence of an optimal gap size defined by a maximal static polarizability in the linear response regime. For some dimers, the electronic coupling before the bond breaking can be strong enough to lift the spin degeneracy and induce a net magnetic moment in the dimer although each nanoparticle is nonmagnetic. The response of a dimer to a finite electric field may become nonlinear as the field energy is high enough. Interestingly, in the nonlinear regime, the magnetic property of a specific dimer can be easily tuned by the electric field magnitude.

Finally, using the classical electromagnetic (EM) theory, one-dimensional (1D) and 2D nanoparticle dimer arrays were studied within the context of SERS. It has been shown that the local EM enhancement in an array can reach 10^{14} at the resonant frequency and with the optimal geometry,

due to the collective photonic effect constructively superposed onto the intrinsic enhancement associated with an isolated dimer. This photonic effect is also responsible for the oscillation of EM enhancement with the length of a 1D array or along an array with a fixed length.

Contents

List of Figures

Chapter 1

Introduction

Low-dimensional systems have been gaining increasing interests over the last few decades, due to their intriguing physical and chemical properties, such as surface-enhanced spectroscopy [1], surface plasmon [2–4] and surface catalysis [5]. "Low-dimensional", generally speaking, refers to the breaking of translational symmetry in the crystal bulk, which means the interface becomes important and may support intriguing phenomena. With the rapidly developing nano-fabrication techniques, many types of low-dimensional systems, such as atomically smooth surface, nanowires [6] and nanoparticles [7], have been realized. On the other hand, metals often play an important role in the low-dimensional systems, which is also the major topic in this dissertation.

1.1 Surface and Nanoparticles

Surfaces can have different orientations, as shown in Fig. 1.1, where Fig. 1.1(a) is the (111) surface and Fig. 1.1(b) is the (100) surface of fcc structure. Physical and chemical properties may be sensitive to surface directions. One example is the different intensity of enhanced Raman spectra of the molecule pyromellitic dianhydride (PMDA) adsorbed on the Cu(111) and Cu(100) surfaces [8–10].

A special type of low-dimensional system is a nanoparticle, which has a large surface-to-volume ratio. The scale of a nanoparticle considered usually ranges between 1-100 nm and consists of tens

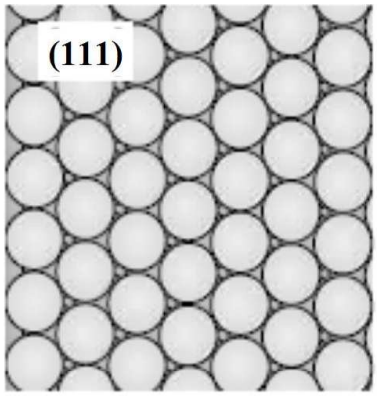

(a)

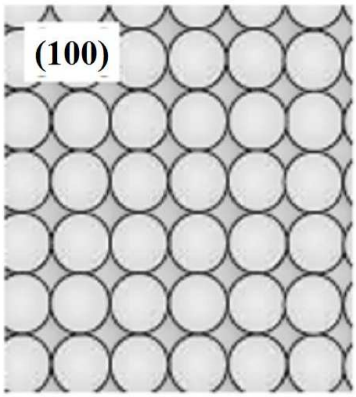

(b)

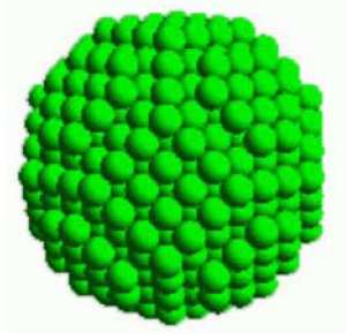

(c)

Figure 1.1: (a)(b) Surfaces of fcc structure with (111) and (100) orientations (c) Nanoparticle.

to millions of atoms, as illustrated in Fig. 1.1(c) [11]. Because the electrons are all confined in the nanoparticle, the energy levels are clearly discretized, rendering the properties of nanoparticle significantly different from bulk or two-dimensional flat surfaces. The nearly spherical symmetry of nanoparticles also influences their properties, such as the coupling with light. Mie resonance is an example of light scattering from nanoparticles [12].

More intriguing phenomena often occur when the nanoparticles are aggregated and electronically coupled to each other [13,14]. There are different types of coupling between the nanoparticles. When the nanoparticles are so close that they nearly touch each other, their electron waves are hybridized and electronic structure of the whole system is strongly modified, rendering the physical properties substantially changed. One example is that the induced charge distribution under external electric field is tremendously different, before and after two metal nanoparticles enter the touching contact regime, which was studied using quantum mechanical jellium model and shown in Fig. 1.2 [15]. on the other hand, when the nanoparticles are far away, long-range electromagnetic interaction will dominate. The intriguing properties of nanoparticle aggregates have been witnessed in many experimental and theoretical studies, which will be explained in the following sections.

1.2 Concepts and Applications of Surface Plasmon

In solid state physics, a plasmon refers to the collective excitation mode of electrons in conductive materials [16]. The collective excitation is translated into the strong oscillation of charge density in the real space. The surface plasmon (SP) is one kind of plasmon that was discovered in the 1950s [2–4]. SP is the electron density wave that propagates along the surface of a metal, which is depicted in Fig. 1.3(a) [17]. The electromagnetic fields shown in Fig. 1.3(a) are trapped on the surface because of their coupling with the free electron of the metal conductor, and this coupled excitation involving both electromagnetic field and electron density wave is called a surface plasmon polariton. By altering the structure of a metal's surface, the properties of SP, in particular its interaction with light, can be tailored, which offers potential for developing new types of photonic

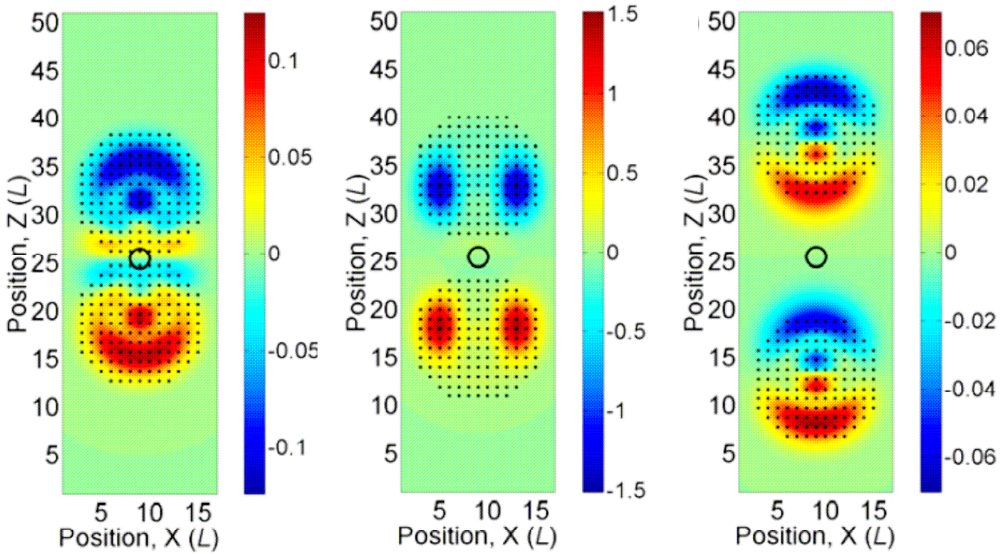

Figure 1.2: Induced charge density in systems of two metal spherical nanoparticles with different interparticle separations. Each nanoparticle has a radii of $R = 7L$, where L is the numerical grid spacing.

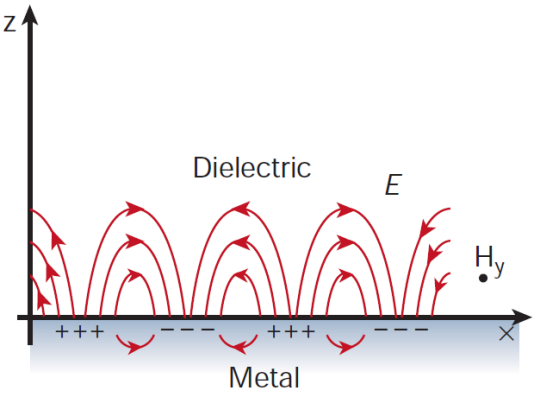

(a)

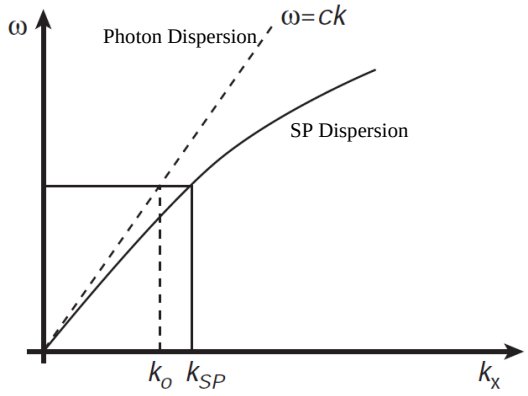

(b)

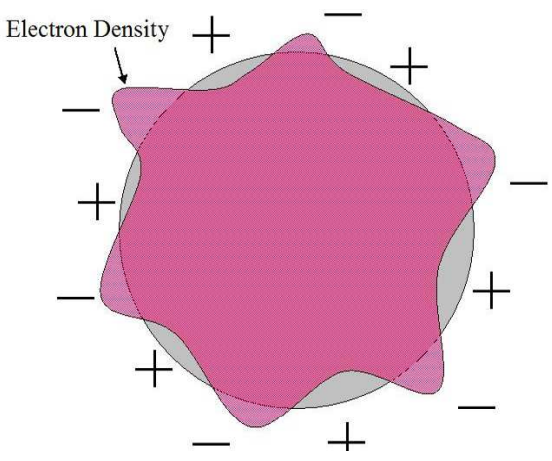

(c)

Figure 1.3: (a) Plasmon on flat surface (b) Dispersion curve for SP on flat surface (c) Plasmon on nanoparticle.

devices. SP is explored in the a variety of fields including subwavelength optics [17], surface-enhanced spectroscopy [18], heating for medical purpose [19] and microscopy [20], etc.

One of the most attractive aspects of SP is that they could help to concentrate and channel light using subwavelength structures [17], which are structures that have dimensions smaller than the wavelength of light. The involvement of the subwavelength structures give rise to the subwavelength optics. This could lead to minaturized photonic circuits with length scales much smaller than those currently achieved. These circuits convert light into SP before processing the SP, and then convert SP back into light. A variety of subwavelength components are required to build such a circuit, including waveguides, switches, couplers, etc. The emerging nanofabrication techniques have rendered all these possible.

Photonic bandgap (PBG) materials [17,21–23] is yet another application of SP in subwavelength optics. PBG has been predominantly made in periodically structured insulating and semiconducting materials. By making use of SP, metals can be used as PBG materials, but in the form of photonic surfaces. The nature of SP changes when they propagate on metal surfaces that are periodically textured on the scale of the wavelength of light. Similar as electron waves in the crystal, SP standing waves and the openining of an SP stop band may be formed when the period of the nanostructures is half that of the effective wavelength of the SP mode. When the surface is modulated in both in-plane directions, SP modes may be prevented from travelling in any in-plane direction, thus leading to a full PBG for SP modes.

The surface plasmon is also supported by the surface of nanoparticles, and in this situation, it is called localized SP (LSP), which does not propagate because of dimension restriction associated to the nanoparticles. LSP has the ability to focus (or more intuitively, "squeeze") light into nanometer dimensions, producing large local enhancements of electromagnetic fields. This large enhancement is one of the fundamental mechanism of the important and broad field called surface-enhanced spectroscopy, which will be covered in detail in section 1.4, 1.5 and 1.6.

Another application of the surface plasmon is in near-field microscopy. The ability of the SP to squeeze the light into the nanoscale allows microscopy to overcome the diffraction limit and reach subwavelength resolution. In ref. [20], the authors for the first time used a single gold nanoparticle as

a subwavelength antenna to image their sample of latex particles. Interestingly, in this experiment and other similar ones, the sample does not have to be illuminated, neither is light from sample necessary to be received, because these experiments make use of modification of SP due to its near-field interaction with the sample. In ref. [24], the authors consider theoretically a three dimensional array of closely spaced nanoparticles, which have geometry and separation that are optimized to tune the plasmonic response and transfer energy and image from one layer to the next.

1.3 Theories of Surface Plasmon

According to the work of Pines and Bohm, the bulk plasmon has the frequency $\omega_B = (4\pi ne^2/m_e)^{1/2}$, where n is the electron density, e is the electron charge, and m_e is the mass of electron [16].

On the flat metal surface, the coupling between the electromagnetic (EM) field and surface charge renders the propagation of SP to be non-radiative, which prevents the power propagating away from the surface. The attenuation of the SP is only due to the losses arising from absorption in the metal. For the low-losses metal, such as silver in the visible spectrum, the propagation distance is typically in the range of 10-100 μm. On the other hand, on a flat surface, the momentum of the SP mode $\hbar K_{sp}$ is greater than the momentum of photon in free space $\hbar K_0$ with the same frequency, which is illustrated in Fig. 1.3(b) [17]. In fact, solving Maxwell's equation for the plane surface separating dielectric media with dielectric value ϵ_d and metal with dielectric function $\epsilon_m(\omega)$, one can come up with the SP dispersion:

$$k_{sp} = \frac{\omega}{c}\sqrt{\frac{\epsilon_d \epsilon_m}{\epsilon_d + \epsilon_m}} \tag{1.1}$$

To excite the SP, the momentum difference between a plasmon and a photon has to be compensated. Three main techniques have been adopted: the use of prism coupling to enhance the momentum of the incident light [25, 26], scattering from the topological defect on the surface to generate SP locally [27], and the use of a periodic corrugation in the metal's surface [28]. If Drude model [16] is considered, the plasmon frequency for the flat surface is $\omega_s = \omega_B/\sqrt{2}$ in the nonretarded limit ($q >> \omega_s/c$) [2].

The SP supported by the nanoparticle is depicted in Fig. 1.3(c), which differs substantially from that on the flat surface in several aspects [2–4]. The induced charge density oscillating on the curved surface of the nanoparticle can strongly redistribute and focus the EM field near the particle when coupled with light, which is important to the surface-enhanced spectroscopy [1]. On the other hand, the surface plasmon in nanoparticles is damped by radiation in addition to the absorption by metal. The plasmon modes in the ideally spherical nanoparticles have the symmetry described by spherical harmonics Y_l^m [29], which are excited by the corresponding modes of light with the same symmetry. In the classical regime, the light scattering by spherical nanoparticle can be well described by Mie theory, where the SP modes are called Mie resonant modes [12]. In the long wavelength limit and using the Drude model, the Mie plasmons have the frequencies [2] $\omega_l = \omega_B \sqrt{\frac{l}{2l+1}}$. Similarly, a spherical cavity has the plasmon frequencies $\omega_l = \omega_B \sqrt{\frac{l+1}{2l+1}}$.

When the nanoparticles are aggregated but still far away from touching contact regime, their individual plasmon modes couple to each other and hybridize, as depicted in Fig. 1.4(a) [30]. There are two effects of this plasmon hybridization: first, charge density oscillation in each nanoparticle may be significantly enhanced, and the EM field intensity in the nanogap region can be much higher than twice of the individual nanoparticle; second, plasmon energies can be clearly shifted, some red-shifted and some blue-shifted, in analogy to the molecular orbital hybridization.

Similar plasmon hybridization occurs in the metal nanoshell [31]. Metal nanoshell is the structure involving a thin (1-10 nm in thickness) metal film wrapping a dielectric core, and the SP of the inner and outer surface of the shell will hybridize, as depicted in Fig. 1.4(b). The plasmon hybridization in the nanoshell has similar effects as that in the dimer, and for this reason, in surface-enhancement Raman scattering experiments, it was observed that the isolated nanoshell may induce an enhancement comparable to that generated by a dimer [32]. In the experiments performed in Ref. [32], for solid nanoparticles, only SERS signal from dimers can be observed; while for nanoshells, SERS signal for both dimer and single nanoparticle can be observed. In the long wavelength limit and using the Drude model, the plasmon frequencies of the nanoshell with an inner radius r_1 and outer radius r_2 are well established as [2, 31]:

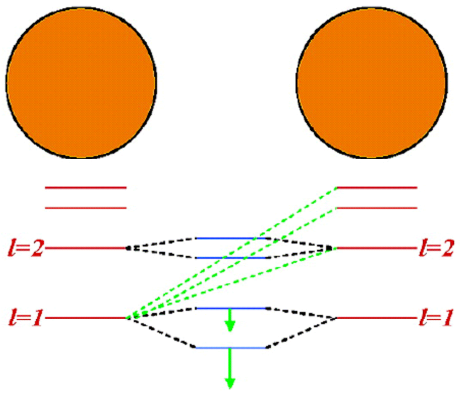

(a)

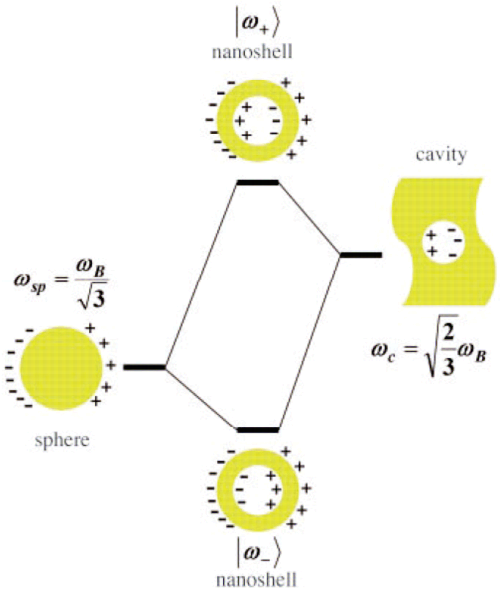

(b)

Figure 1.4: (a) Hybridized plasmon in nanoparticle dimer. l characterizes the angular momentum of the plasmon. (b) Hybridized plasmon in nanoshell. ω_B is the bulk plasmon prequency.

$$\omega_{\pm}^2 = \frac{\omega_B^2}{2}[1 \pm \frac{1}{2l+1}\sqrt{1+4l(l+1)(r_1/r_2)^{2l+1}}] \tag{1.2}$$

In the similar geometry of a flat metal thin film, the plasmons of the two surfaces also hybridize and the resulting plasmon frequencies are $\omega_{\pm} = \frac{\omega_B}{\sqrt{2}}(1 \pm e^{-qa})^{1/2}$, where q is the wave vector of the plasmon propagating along the surface, and a is the thickness of the thin film [2].

On the other hand, when nanoparticles are so close that they nearly touch each other, their electron waves will overlap and hybridize, which strongly modifies the electronic structure of the aggregates. Because of this modification, the plasmon energy becomes sensitive to the separation between the nanoparticles in the touching contact regime, as illustrated in Fig. 1.5 [33]. The theory of plasmon at touching contact can no longer be built within the classical electromagnetic frame and quantum mechanics has to be applied. So far, the studies all use jellium model and show significant difference from the classical results [15, 34].

1.4 Experimental Evidences of Surface-enhanced Raman Scattering (SERS)

Raman scattering by molecule is an inelastic scattering process for light [35,36]. Basically when the incident light impinges on a molecule, a fraction of scattered light will have a different frequency from the incident light. The difference in frequency between the incident and scattered light, also namely Raman shift, corresponds to the frequency of the vibrational mode of the molecule. Thus, Raman scattering is a very useful tool to investigate the structure of molecules and to identify them. However, it should be noted that the incident photon in the Raman process does not directly excite phonons, which is the elementary excitation of vibration, because the energy of photon is much higher than that of a phonon. In fact, the photon-phonon coupling is mediated by the electronic excitation between different energy levels of the molecule and so Raman scattering is a third order process. This leads to the fact that the Raman signal (measured by cross section) from molecules is usually very weak, rendering only the ensemble of a large number of molecules to be detected in reality. The simplest treatment of the Raman process considers the dependence of the molecular

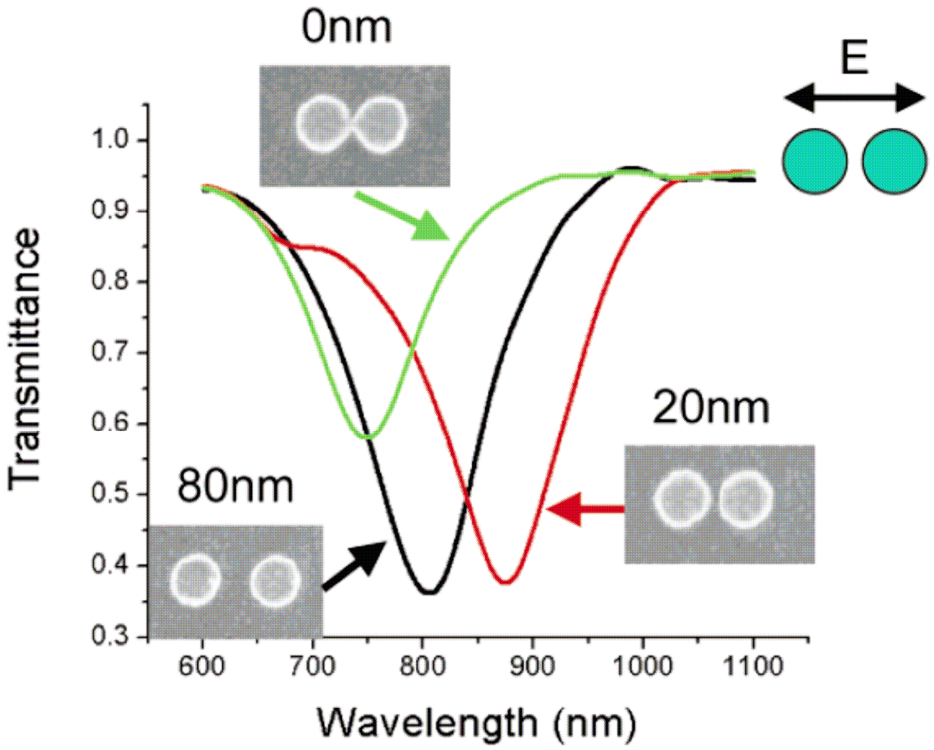

Figure 1.5: Polarized transmittance spectra in periodic arrays of pairwise interacting gold nanodisks. The gap size of the nanodisk dimer is $80nm$, $20nm$ and $0nm$ (touching contact) for black, red and green curves respectively. The plasmon energy correspond to the lowest value of transmittance in the figures, where incident light energy is converted into plasmon energy.

dynamic polarizability $\alpha_m(\omega, Q)$ on the vibrational normal mode Q. When the molecule is excited by incident light with electric field E_{ext}, the dipole moment induced in the molecule is,

$$p(\omega) = \alpha_m(\omega, Q)E_{ext} \approx \alpha_m(\omega, 0)E_{ext} + \alpha'_m(\omega, 0)QE_{ext} \tag{1.3}$$

where the first term in the expansion gives rise to the elastic scattering (Rayleigh scattering), while the second term describes the Raman scattering, and the Raman cross section is proportional to $|\alpha'_m(\omega, 0)|^2$. The molecular electronic excitation process is reflected in the polarizability α_m and its derivative.

In 1974, Fleischmann *et al.* discovered that when Raman active molecules are adsorbed on roughened metal surfaces, the Raman signal can be enhanced by a factor of $10^5 - 10^6$ compared to the case when they are alone (such as in the gaseous phase) [37]. Nobel metals, such as silver, gold and copper, are usually advantageous for SERS. This extraordinarily large signal strength cannot be due to the increase of surface area that adsorbs more molecules [38]. In fact, not only the Raman signal is higher, but the peak position is shifted in the Raman spectra, which indicates the interaction between the molecule and metal substrate. Fig. 1.6 shows the Raman spectra of pyradine adsorbed on the silver film and in the liquid form [1]. This phenomenon is namely surface-enhanced Raman scattering (SERS), and the relative technique has been used widely in a wide range of field, such as chemistry and biology.

In the 1990s, it was realized that extremely large SERS enhancement with the factor of over 10^{10} could be achieved, which pushes to the limit of single molecule sensitivity [39, 40]. It was further established that the giant SERS factor is associated to the nanogap effect, i.e., the Raman active molecule needs to be trapped in the gap region between two closely aggregated nanoparticles, as illustrated in Fig. 1.7(a) [41–43]. In addition to the very low concentration of the molecule, the temporal fluctuation of the SERS spectra, as shown in Fig. 1.7(b), also proves that this spectra is not the ensemble average of a large number of molecules. The dataset 1 and 2 are Raman spectra of hemoglobin (Hb) trapped in the nanogap of silver nanoparticle dimers, taken every 30 seconds.

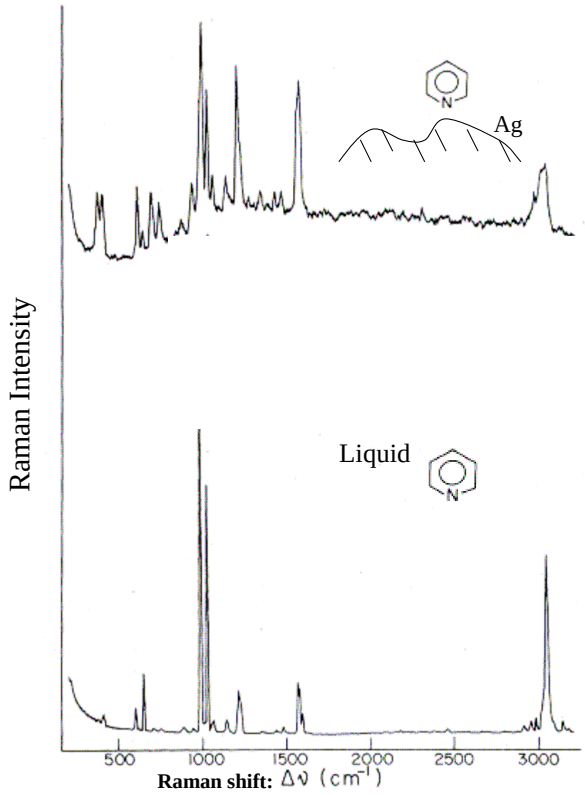

Figure 1.6: Raman spectra of pyradine adsorbed on the silver film (top) and in the liquid form (bottom).

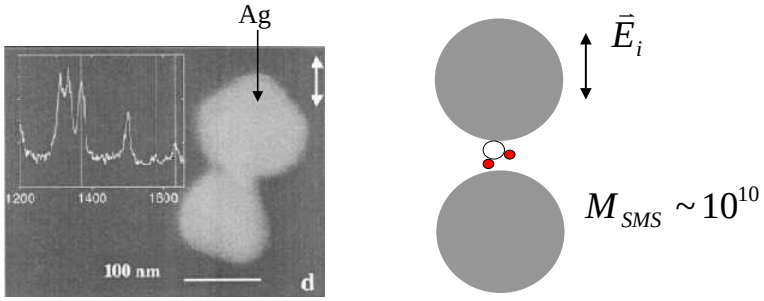

(a)

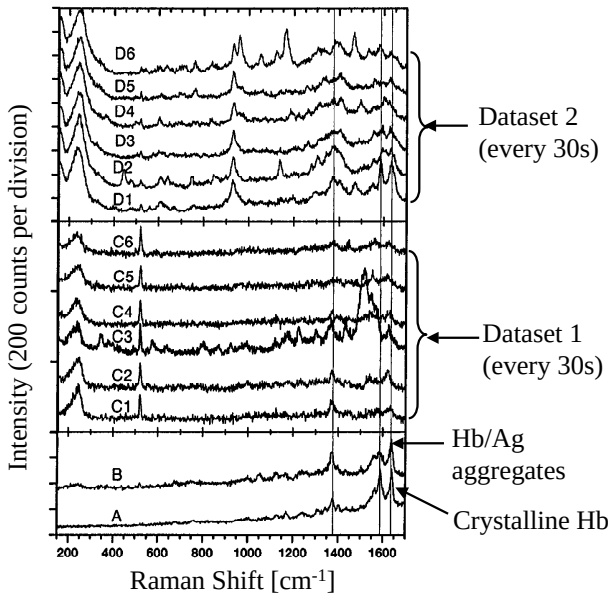

(b)

Figure 1.7: (a) SEM image (left) and model (right) of silver nanoparticle dimers that gives 10^{10} SERS enhancement (b) Confocal Raman spectra of crystalline met-Hb (A), dense layer of Hb/Ag aggregates (B), and two time series (C1-C6 and D1-D6) obtained at the single molecule detection limit.

Another interesting discovery is that even on the atomically flat metal surface, the SERS enhancement still exists. The enhancement factor is about 10-100, which provides direct evidence of chemical enhancement to be discussed in section 1.6 [8–10].

1.5 Electromagnetic Effect for SERS

As mentioned in section 1.2, the EM field incident on a curved metal substrate, especially that of nanoparticles, is focused due to the effect of (L)SP. At the "hot spots" where the EM field is highly focused, the greatly enhanced field intensity leads to the EM effect for SERS [1, 41, 43]. The contribution to the SERS from EM effects can be written as $M_{em}(\omega) \approx [|\vec{E}_{loc}(\omega)|^2/|\vec{E}_i(\omega)|^2] \cdot [|\vec{E}_{loc}(\omega \pm \nu)|^2/|\vec{E}_i(\omega \pm \nu)|^2]$, where ω is the incident light frequency, ν is the vibrational frequency of the molecule, $\vec{E}_i$ is the electric field of incident light, while $\vec{E}_{loc}$ is the electric field at the hot spots. Generally, $\vec{E}_{loc} = \vec{E}_i + \vec{E}_s$, where $\vec{E}_s$ is the electric field scattered by the metal substrate. The first part in the multiplication refers to the enhancement of EM field intensity "felt" by the molecule adsorbed at the hot spots, while the second part is the further enhancement of the Raman-scattered field intensity by the metal substrate. Since the $\nu << \omega$, the EM effect is usually estimated as $M_{em}(\omega) \approx [|\vec{E}_{loc}(\omega)|^4/|\vec{E}_i(\omega)|^4]$ in theoretical studies. The peaks of the spectra $M_{em}(\omega)$ correspond to plasmon frequencies of the substrate, which should be tuned to be equal or close to the frequency that excites the Raman process in the molecule. To tune the plasmon frequency, one may change the geometry of the substrate, or change the material of the substrate and surrounding environment.

Nanoparticles can produce strong EM enhancement, due to their curved surface. Using the Drude model, we can do the simplest estimate for a spherical nanoparticle: its dynamic polarizability in the Drude model is written as $\alpha(\omega) = R^3[1 - \frac{\omega}{\Omega}(\frac{\omega}{\Omega} + i\frac{\gamma}{\Omega})]^{-1}$, where R is the radius of the nanoparticle, ω is the incident light frequency, $\Omega = \omega_B/\sqrt{3}$ is the plasmon frequency of the nanoparticle, and γ represents the effective damping of the plasmon. When a molecule is adsorbed on the nanoparticle surface, the dipolar field of the nanoparticle "felt" by the molecule is $\vec{E}_{loc}(\omega) = \vec{E}_i(\omega)[1 - \frac{\omega}{\Omega}(\frac{\omega}{\Omega} + i\frac{\gamma}{\Omega})]^{-1}$. Since the damping $\gamma \approx 0.1\Omega$, at resonance when $\omega = \Omega$,

the EM enhancement M_{em} is estimated to be 10^4. When nanoparticles are aggregated, the hybridized plasmon of the aggregates will give rise to extremely strong EM enhancement, which is believed to be the orgin of the nanogap effect [41, 43]. Since the smallest aggregate that has a nanogap is a dimer, which is a pair of closely packed nanoparticles, extensive studies have been focused on the EM enhancement in dimers. Since the major part of the problem is to calculate the EM field distribution, many existing techniques are used, such as Mie theory [44,45] and finite-difference time-domain (FDTD) [46], etc. Fig. 1.8 shows the M_{em} spectra of single nanoparticles and dimers [42]. Obviously, the enhancement factor is sensitive to the field polarization direction relative to the dimer axes.

It should be noted that the classical description of the dimer effect is valid only when the gap size between nanoparticles is large enough, because as mentioned in section 1.1, after entering the touching contact regime, the physical properties can be substantially different. In fact, when the gap is small, electrons tunnel across the dimer junction and screen, significantly modifying the optical response and reducing the EM enhancement relative to classical predictions [34]. Using quantum mechanical jellium model, it has been shown that when the gap dimension is smaller than a few Å, this tunneling effect cannot be ignored; while if the gap size is larger, the dimer plasmon can be well described by classical EM theory. This result is illustrated in Fig. 1.9 [34].

1.6 Chemical Effect for SERS

As mentioned in section 1.4, SERS with an enhancement factor of 10-100 has been observed when the metal substrate is atomically flat. Since the EM field cannot be enhanced by a flat surface, the enhancement can only be due to the modification of electronic structure of the molecule, arising from the chemical binding between the molecule and substrate.

It has been estimated theoretically that the charge transfer between the molecule and substrate indeed leads to an enhancement around 10^2 [47]. As depicted in Fig. 1.10, a resonant level of the molecule is broadened when the molecule binds to the metal surface, and the consequent charge transfer from molecule to metal leaves the molecule energy level only partially filled. The effective

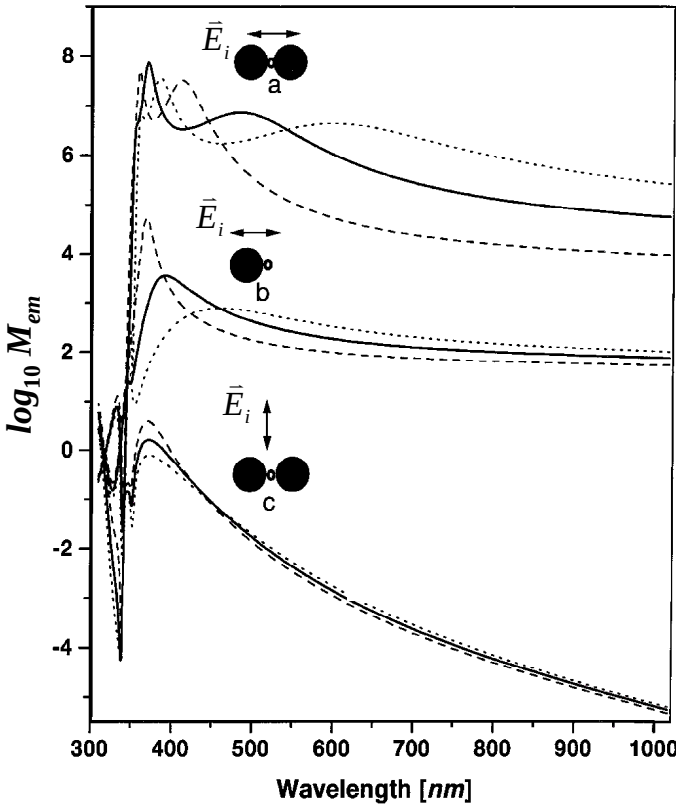

Figure 1.8: EM enhancement M_{em} for the midpoint between two silver nanoparticles separated by $d = 5.5nm$ and for a point $d/2$ outside a single nanoparticle. The calculation has been performed for spheres for diameters D=60 (dashed curves), 90 (solid curves) and 120 nm (dotted curves).

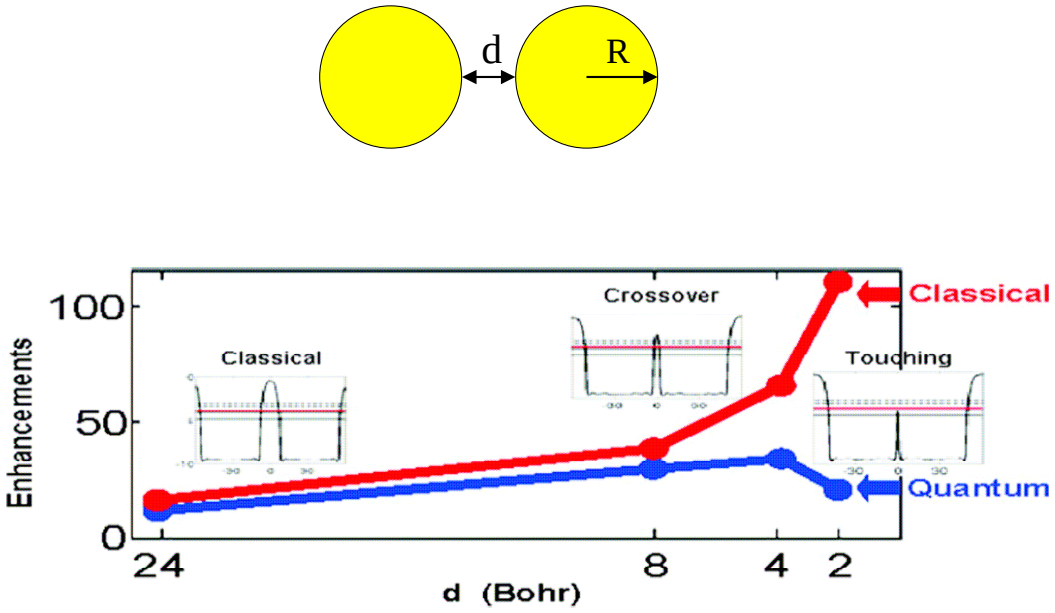

Figure 1.9: Comparison of the maximum electromagnetic field enhancements in the gap of nanoparticle dimers, calculated using classical plasmon hybridization method (red) and quantum mechanical theory (blue) based on jellium model respectively.

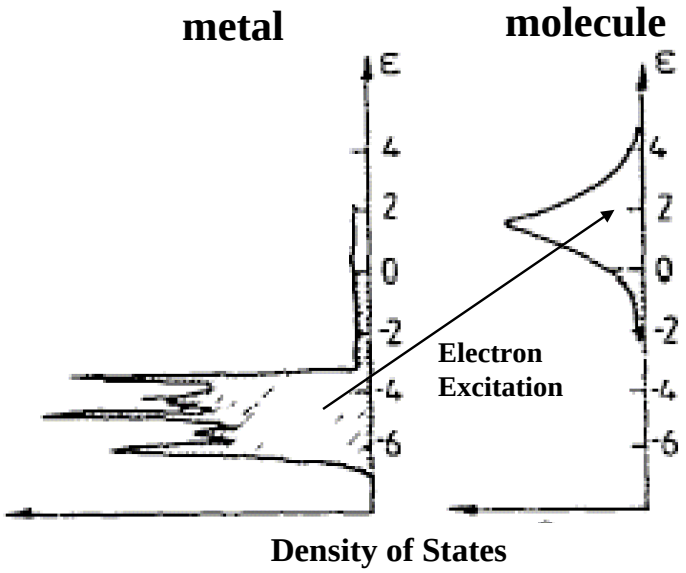

Figure 1.10: Electron excitation from the Fermi sea of metal substrate to the empty state of molecule, where the broadened level of molecule is a result of chemical binding of the molecule on the metal surface.

photon-phonon coupling mediated by electronic excitation from metal to molecule is significantly higher than that by the excitation between different levels of the molecule alone, leading to a significantly enhanced Raman signal. It should be noted that the chemical effect for SERS is less understood than the EM effect.

1.7 Outline of Thesis

In this thesis, electronic, optical and magnetic properties of low-dimensional metal systems, and their interaction with molecules are investigated across multiple scales using a variety of theoretical and computational techniques.

Chapter 2 is about a new chemical effect for SERS. This study considers molecules adsorbed on a single nanoparticle surface, and microscopic phenomenological model is employed to discover a new mechanism responsible for the chemical enhancement.

Inspired by the dimer effect for single molecule SERS and LSP, my colleagues and I also used *ab initio* density functional theory (DFT) to study the electronic structure and response to electric field in small nanoparticle dimers. While the previous studies of this kind only used simplified models such as the jellium model, our study considers real atoms. The *ab initio* DFT study is completely quantum mechanical that very well describes the variety of phenomena associated to the nanogap, which has the scale of only a few Å. Although our study only considers static electrical response, the relative conclusions such as bond breaking between nanoparticles are enlightening to a large number of SP and SERS problems, such as plasmon frequency shift at the touching contact limit. Chapter 3 investigates the electric linear response, while Chapter 4 considers nonlinear response.

Despite its accuracy, the heavy computational load renders *ab initio* DFT to be impossible to describe plasmon and SERS for large nanoparticles used in real-life experiments. But on the other hand, for large enough gap size, the results obtained from classical electromagnetics agree pretty well with those from DFT [34]. In chapter 5, I shall present the EM enhancement for SERS arising from collective plasmon interaction in one and two-dimesional nanoparticle dimer arrays, using classical EM theory. The nanoparticles have the scale comparable to those in real-life experiments,

and the gap sizes considered are no smaller than $1nm$, which should be compatible with classical EM theory.

Chapter 6 is a perspective of the studies that are expected to be taken in the near future, which contains several points: 1. A multiscale approach is proposed, which concurrently solves the complex system involving both molecule and real-life sized nanoparticle dimers; 2. The issue of chemical effect regarding the molecule trapped in the gap region between two metal nanostructure is presented, and the corresponding microscopic phenomenological model is proposed; 3. Based on the unexpected magnetic properties presented in Chapter 3, spin polarized transport through quantum point contact is expected.

Chapter 7 concludes the major contribution which my colleagues and I have been working on in the past few years during my Ph.D study.

Chapter 2

Chemical Effect for SERS

As mentioned in Chapter 1, SERS with an enhancement factor of 10-100 has been observed when the metal substrate is atomically flat. Since the EM field cannot be enhanced by flat surface, the enhancement can only be due to the modification of electronic structure of the molecule, arising from the chemical binding between the molecule and substrate. This effect is generally called chemical effect for SERS.

2.1 Standard Charge Transfer Model for SERS

Earlier, Persson proposed a mechanism, namely charge transfer model, for this chemical effect of SERS [47]. The Persson model is an extension of the well-known Anderson model [48] When a molecule with an orbital $|a>$ and energy level ϵ_a approaches a metal surface, its originally sharp density of states (DOS) at level ϵ_a is broadened by the fact that the tunneling of electrons between the molecular orbital $|a>$ and the metal gives it a finite lifetime and hence a halfwidth 2Γ. In Persson's charge transfer model for SERS, the broadened local DOS (DOS projected on orbital $|a>$) is assumed to be a Lorentzian function:

$$\rho_a^{adsorbed}(\epsilon) = \pi^{-1} \frac{\Gamma(\epsilon)}{[\epsilon - \widetilde{\epsilon}_a]^2 + \Gamma^2(\epsilon)} \tag{2.1}$$

where the $\widetilde{\epsilon}_a$ is the center of broadened molecular level, which is shifted from the original ϵ_a.

If the broadened level of the molecule $\rho_a(\epsilon)$ is located in the vicinity of the Fermi energy of the metal, charge is transfered between the molecule and the metal, and as a result, the level is only partially filled, as shown in Fig. 1.10. The partially filled level allows electrons to be excited from the Fermi sea of the metal to the empty part of the molecular level by incident light. The effective photon-phonon coupling mediated by this electronic excitation can be significantly stronger than that by the excitation between different levels of the molecule alone (the relative theory was briefly presented in Chapter 1). There are also other charge transfer models that involve two molecule levels, but the essential idea is the same [49,50]. So in what follows, only Persson's model involving one molecular level is presented.

The Hamiltonian for the charge transfer mechanism in Persson's model is:

$$H = [\epsilon_a(Q) - edE_z]\hat{n}_a + \sum_k \epsilon_k a_k^+ a_k + \sum_k (V_{ak} a^+ a_k + h.c.) + \hbar\Omega b^+ b + H_{EM} \tag{2.2}$$

where Q is the displacement associated with a vibrational mode of the molecule and $\epsilon_a(Q)$ is the resonant level (close to the Fermi energy of the metal substrate) of the molecule. ϵ_k is a set of energy levels for the electrons in the metal and V_{ak} describes the hopping of an electron between the molecule and the metal, giving rise to the charge transfer. a^+ and a are creation and annihilation operators of the molecule, while a_k^+ and a_k are those of the metal. The last two terms in Eq. 2.2 are energy associated with the vibrational and electromagnetic degrees of freedom alone. b^+ and b are creation and annihilation operators of molecule vibration, and H_{EM} is the photon energy. The coupling between the molecule and the light is described by the term $-edE_z\hat{n}_a$ where d is the distance between the "center of charge" of the orbital $|a>$ and the image plane in the metal.

The Hamiltonian 2.2 is decomposed into two parts in order to describe the SERS process:

$$H = H_0 + V \tag{2.3}$$

with H_0 involving only uncoupled electron, photon and phonon degrees, and written as:

$$H_0 = \sum_\alpha \epsilon_\alpha c_\alpha^+ c_\alpha + \hbar\Omega b^+ b + H_{EM} \tag{2.4}$$

where

$$\sum_{\alpha} \epsilon_{\alpha} c_{\alpha}^{+} c_{\alpha} = \epsilon_a(0) a^{+} a + \sum_{k} \epsilon_k a_k^{+} a_k + \sum_{k} (V_{ak} a^{+} a_k + h.c.) \tag{2.5}$$

is the electronic degree of the metal-molecule system, at the vibrational equilibrium position. c_{α}^{+} and c_{α} are the creation and annihilation operators of electron in the whole system.

The term

$$V = [\epsilon_a'(0) Q - e d E_z] \sum_{\alpha\beta} < \beta | a >< a | \alpha > c_{\beta}^{+} c_{\alpha} \tag{2.6}$$

describes the coupling between electron and photon, and coupling between electron and phonon. So the term V gives rise to the photon-phonon coupling mediated by electron excitation and the Raman process.

The charge transfer models, including Persson's model estimate that the chemical enhancement factor is around 10-100, which agrees well with experiments.

2.2 Diffusive-like Surface Scattering

When an electric field is applied parallel to the metal surface, a process namely diffusive-like electron scattering by the surface exists, as illustrated in Fig. 2.1. A molecule adsorbed on the metal surface, on the other hand, can modify the diffusive-like electron scattering cross section, and thus the dielectric response of the metal [51, 52]. The similar mechanism is also responsible for the surface resistivity, which is the modification of electric resistivity along the metal surface by adsorbed molecule [53]. It can be imagined that the modified dielectric response of the metal-molecule complex is modulated by the vibrational motion (phonon) of the adsorbate molecule, which in turn is coupled to the photon. In what follows, we will show that this coupling is stronger than the photon-phonon coupling within an isolated molecule, leading to a new mechanism for SERS.

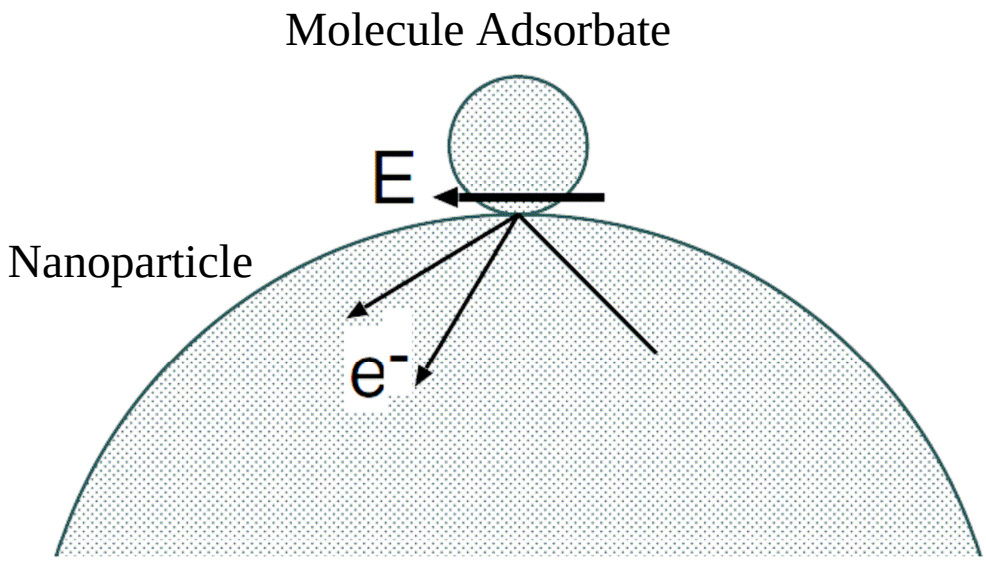

Figure 2.1: Diffusive-like scattering of electron at the metal surface, involving only parallel electric field at the molecule spot.

2.3 New Chemical Effect for SERS with Molecules Bound to a Nanoparticle

Consider a metal nanoparticle with radius R and without molecule adsorbed on it. If R is much smaller than the wavelength of the incident light, then we can treat the particle within the dipole approximation where the elctric field on the surface of the particle is of order p/R^3, where the induced dipole $p = \alpha_p E_i$, α_p is the polarizability of the particle and E_i is the electric field of the incident light (in this chapter, the directions of the vectors, such as electric field and dipole moment, are not explicitly indicated). For a free-electron-like metal and considering the Drude model, the polarizability of the particle is given by

$$\alpha(\omega) = R^3[1 - \frac{\omega}{\Omega}(\frac{\omega}{\Omega} + i\frac{\gamma}{\Omega})]^{-1} \tag{2.7}$$

where R is the radius of the nanoparticle, ω is the incident light frequency, $\Omega = \omega_B/\sqrt{3}$ is the plasmon frequency of the nanoparticle, and γ measures the effective damping of the plasmon. When a molecule is adsorbed on the nanoparticle surface, the dipolar field of the nanoparticle "felt" by the molecule is

$$E_{loc}(\omega) = E_i(\omega)[1 - \frac{\omega}{\Omega}(\frac{\omega}{\Omega} + i\frac{\gamma}{\Omega})]^{-1} = K(\omega)E_i(\omega) \tag{2.8}$$

The EM enhancement is $M_{em}(\omega) \approx |K(\omega)|^4$.

When the molecule is adsorbed on the nanoparticle surface, it will modify the dielectric response of the metal by changing the damping γ. For a metal with or without a molecule adsorbate, we write

$$\gamma = \gamma_0 + Cv_F/R \tag{2.9}$$

γ_0 which is the electron scattering in the metal bulk, as usually described by a Drude relaxation time τ_D via $\gamma_0 = 1/\tau_D$; and Cv_F/R is the diffusive-like scatttering of the electrons from the surface of the nanoparticle, where v_F is the Fermi velocity. The prefactor C can be enhanced

significantly for a metal surface covered by molecule adsorbates, as compared to that without a molecule adsorbate. For a silver nanoparticle in vacuum, $C \approx 0.3$ as obtained theoretically and also measured experimentally. When the molecule CO or C_2H_4 are adsorbed on the silver nanoparticle, the prefactor C is increased to $C \approx 1.0$ and $C \approx 0.7$ respectively. The enhancement of C is due to fact that molecules interact chemically with the silver nanoparticle surface and give rise to a large effective cross sections to scatter the silver metal electrons nonspecularly. On the other hand, very inert molecule adsorbates such as the light noble gas atoms Ne and Kr do not interact chemically with silver and have very weak influence on the scattering of the metal electrons from the silver particle surface.

It has been shown that the enhancement of the prefactor C due to the presence of a molecule is [52]

$$\Delta C = \frac{3}{8} n_a \sigma_{diff}(\omega) \tag{2.10}$$

where n_a is the number of adsorbed molecules per unit area, and $\sigma_{diff}(\omega)$ is the effective cross section (at the exciation frequency ω) for diffusive-like scattering of metal electrons from the adsorbed molecule. The function $\sigma_{diff}(\omega)$ depends on the nature of the chemical bond between the molecule and the substrate. Again, consider the case of one broadened molecular level centered around the Fermi level of the metal, we have

$$\sigma_{diff} = \frac{\sigma_0 \pi \Gamma}{4\epsilon_F \hbar\omega} \int_{\epsilon_F - \hbar\omega}^{\epsilon_F} d\epsilon [\epsilon \rho_a(\epsilon + \hbar\omega) + (\epsilon + \hbar\omega)\rho_a(\epsilon)] \tag{2.11}$$

where σ_0 depends on the electron density of the metal substrate and on the symmetry of the resonant state. for the $2\pi^*$ state of CO on Ag, $\sigma_0 \approx 50$ Å^2. In what follows, we are only interested in $\omega \approx \Omega$ and the frequency dependence of σ_{diff} will not be stated explicitly. For CO and C_2H_4, σ_{diff} is of order 5-10 Å^2. If only one molecule is adsorbed on the nanoparticle, then $n_a = (4\pi R^2)^{-1}$ and

$$\Delta C = \frac{3}{32\pi R^2} \sigma_{diff} \tag{2.12}$$

As mentioned above, the theory for the adsorbate contribution to C is very similar to the theory used to calculate the influence of adsorbates on the surface resistivity of metals [53]. In fact, the main difference is that in the present case, the cross section σ_{diff} corresponds to the frequency of incident light, while in surface resistivity applications only the zero frequency cross section enters. For molecules such as CO or C_2H_4 chemisorbed on silver, $\sigma_{diff}(\Omega) \approx 10\sigma_{diff}(0)$. This large enhancement comes from the fact that the relevant adsorbate induced resonant states involved in the electron scattering process are centered a few electron volts (eV) above the Fermi energy of metal and hence can be nearly resonantly occupied at optical frequencies, while at very low frequencies only the tail of the resonant state at the Fermi energy can be involved in the scattering process.

For a metal nanoparticle with a single adsorbed molecule, the cross section σ_{diff}, and hence the parameter C, depend on the chemisorption bond between the metal nanoparticle and the molecule adsorbate. The chemisorption bond will change when the nuclear positions of the atoms in the adsorbate change. Thus, σ_{diff} (and C) can be viewed to depend parametetrically on the vibrational normal mode Q of the adsorbed molecule, leading to $\sigma_{diff}(Q) \approx \sigma_{diff}(0) + \sigma'_{diff}(0)Q$. Substituting this in 2.12, and using 2.9 and 2.7 gives, to leading order in Q,

$$\alpha_p(\omega, Q) \approx KR^3 + K^2 \frac{3iv_F}{32\pi\Omega}\sigma'_{diff}(0)Q \tag{2.13}$$

Thus in this case, the Raman dipole is:

$$p_{Raman} = iK^2 D\sigma'_{diff}(0)QE_i \tag{2.14}$$

where $D = 3v_F/(32\pi\Omega)$. On the other hand, the Raman dipole of a molecule in gaseous phase is $p_{Raman} = \alpha'_m(0)QE_i$, where $\alpha'_m(0)$ is the derivative of the polarizability α_m of the molecule with respect to Q (see Chapter 1). Since the Raman intensity is proportional to the square of p_{Raman}, separating out the EM enhancement K^4, the ratio between the SERS cross section with

and without the chemical contribution is

$$\left|D\sigma'_{diff}(0)\right|^2 : \left|\alpha'_m(0)\right|^2 \tag{2.15}$$

It is assumed that the adsorbed molecule has an electronic resonant state centered a few eV above the metal Fermi level. The resonant state is derived from some molecular energy level ϵ_a, and we assume that the only dependence of σ_{diff} on Q comes from the dependence of $\widetilde{\epsilon}_a(Q)$ on Q. For example, for CO chemisorbed on silver, the $2\pi^*$ level in the gas phase molecule shifts below the vacuum energy upon adsorption, forming a $\Gamma \approx 1$eV wide resonant state about 2-3eV above the silver Fermi energy [54, 55]. For the CO $2\pi^*$ level, $\epsilon'_a(0) \approx -11\text{eV/Å}$. For this case, under optimal conditions where the excitation energy $\hbar\Omega$ corresponds to roughly the separation between the metal Fermi energy and the center of the adsorbate induced resonant state, we get $\sigma'_{diff}(0) \approx \sigma_0\epsilon'_a/(2\hbar\Omega)$, where $\sigma_0 \approx 50\text{Å}^2$ for silver. Thus we expect $\sigma'_{diff} \approx 10^2\text{Å}$ for adsorbates such as CO and C_2H_4.

For typical SERS molecules such as CO or C_2H_4 one expects from dimensional arguments and also from experiment, that $\alpha'_m(0) \approx 1\text{Å}^2$. For the surface plasmon excitation of a small silver nanoparticle, $D = 3v_F/(32\pi\Omega) \approx 0.1\text{Å}^2$. Taking $\sigma'_{diff} \approx 100\text{Å}$, the Raman cross section ratio $\left|D\sigma'_{diff}(0)\right|^2 : |\alpha'_m(0)|^2$ becomes 100:1, i.e., the SERS chemical enhancement factor is predicted to be of order 10^2.

2.4 New Chemical Effect for SERS with Molecules Bound to a Flat Substrate

Since the chemical effect is most well defined when the substrate metal is flat, we also studied this case. The simplest treatment of the influence of adsorbed molecules on the optical properties of semi-infinite metals in the frequency region of the so-called anomalous skin effect, which is of interest here, is the "slab model" [56]. In this model, the surface region of the metal is treated as a slab with the thickness $d = \delta$ given by the so-called skin depth $\delta = c/\omega_p$, where c is the light

velocity and ω_p the plasmon frequency. The polarizaibility per unit surface area of this region is given by

$$\chi = -\frac{\omega_p^2 d}{4\pi\omega(\omega + i\gamma)} \tag{2.16}$$

Similar to the nanoparticle, the damping γ has a contribution γ_1 derived from electron scattering from bulk phonons or defects, and another contribution from electron scattering from adsorbed molecules:

$$\gamma = \gamma_1 + \frac{3}{16}\frac{v_F}{d} n_a \sigma_{diff} \tag{2.17}$$

Let us assume that (on average) there is one adsorbed molecule within the surface area A_0, so that $n_a A_0 = 1$. The polarizability of the volume dA_0 is thus

$$\alpha = \chi A_0 = -\frac{\omega_p^2 dA_0}{4\pi\omega(\omega + i\gamma)} \tag{2.18}$$

Expanding σ_{diff} and α to linear order in Q, we get

$$\alpha = -\frac{\omega_p^2 dA_0}{4\pi\omega(\omega + i\gamma_0)}[1 + \frac{3}{16}\frac{1}{i\omega}\frac{v_F}{d} n_a \sigma'_{diff}(0)Q] \tag{2.19}$$

Thus, the Raman contribution to the dipole $p = \alpha E$ is

$$p_{Raman} = \frac{i\omega_p^2}{4\pi\omega(\omega + i\gamma_0)}\frac{3}{16}\frac{v_F}{\omega}\sigma'_{diff}(0)QE \tag{2.20}$$

Assuming $\gamma_0 << \omega$ we get the chemical enhancement,

$$\left|D(\omega)\sigma'_{diff}(0)\right|^2 : \left|\alpha'_m(0)\right|^2 \tag{2.21}$$

where

$$D(\omega) = (\frac{\omega_p}{\omega})^2 \frac{3}{64\pi}\frac{v_F}{\omega} \tag{2.22}$$

Using the plasmon frequency $\hbar\omega_p = 9$eV gives for $\hbar\omega$ =2.5eV the chemical enhancement as high as ~ 6000.

The model studies above predicts that the *parallel* electric field can also give rise to Raman scattering from adsorbate vibrations. Thus, if Raman scattering could be detected from, e.g., the C-O stretch vibration (for CO adsorbate on a flat silver surface), using an s-polarized electromagentic field, it would be a direct and stringent test of the theory presented here. Such an indirect excitation mechanism with an s-polarized field has its close analogy in IR measurements of dipole forbidden adsorbate vibrations [57, 58] and surface resistivity [53].

Chapter 3

Electronic Coupling and Optimal Gap Size Between Metal Nanoparticles

3.1 Metal Nanoparticle at Touching Contact

As mentioned in Chapter 1, many interesting phenomena have been observed when nanoparticles are closely aggregated and start to interact with each other [13–15]. Therefore, a solid understanding of the inter-particle coupling is of tremendous significance in both fundamental studies and applications of nanotechnology.

A nanoparticle dimer provides the simplest system to investigate how the inter-particle coupling depends on the system geometry and how it affects the physical properties of the system. The majority of existing theoretical studies assumes a classical electromagnetic coupling between the particles [41–43, 59, 60]. It has led to the prediction of a monotonic increase of the static polarizability and local field enhancement with decreasing dimer gap size. However, at shorter distances, in particular when nanoparticles are in touching contact [33, 61, 62], this treatment is bound to fail because the nanoparticles can also be coupled due to the overlap of wavefunctions from neighboring particles [63]. While recent studies focused on simplified models [15, 64], a quantum mechanical treatment based on real atoms is crucial in order to accurately describe the touching contact limit.

This study represents the first comprehensive study of the electronic coupling between two metal nanoparticles using *ab initio* density functional theory (DFT) with real atoms, and silver nanoparticles of varying sizes as prototype systems. We find that the coupling between the nanoparticles shows a strong dependence on the dimer gap size and relative orientation of the particles. When two particles are separated from touching contact, the dimer undergoes a bond-breaking step, and the coupling strength crosses over from the strong to weak regime. This transition step also establishes the striking existence of an optimal gap size (OGS), defined by a maximum in the static (in both this chapter and the next, only static electric field is considered) polarizability of the dimer, an important finding in sharp contrast to the monotonic decrease predicted by classical theories. Moreover, depending on the particle size and their orientation, the electronic coupling before the bond breaking can be strong enough to give rise to a net magnetic moment of the dimer, even though the isolated particles are nonmagnetic. These findings may prove to be instrumental in understanding and controlling various physical and chemical properties of closely-packed nanoparticle aggregates, as revealed by our discussions of their potential impact on SERS from nanoparticle arrays and quantum transport in related systems. The relative work has been published [65].

3.2 Model Dimer Systems

We choose silver nanoparticle dimers as our representative systems. We have studied four distinctive configurations of dimers, as illustrated in Fig. 3.1. These dimers are referred to as $(Ag_n)_2$ where n is the number of atoms within each particle. We have chosen $n = 14$ and 18, and two different orientations of the nanoparticles, namely, tip-tip (t-t) [Figs. 3.1 (a) and (c)] and plane-plane (p-p) [Figs. 3.1 (b) and (d)].

3.3 Density Functional Theory

DFT is a very useful method to study the electronic properties of many-electron systems. Within DFT, the electron density of a system in a nondegenerate ground state completely determines all aspects of its electronic structure. In 1964, Hohenberg and Kohn developed an exact theoretical

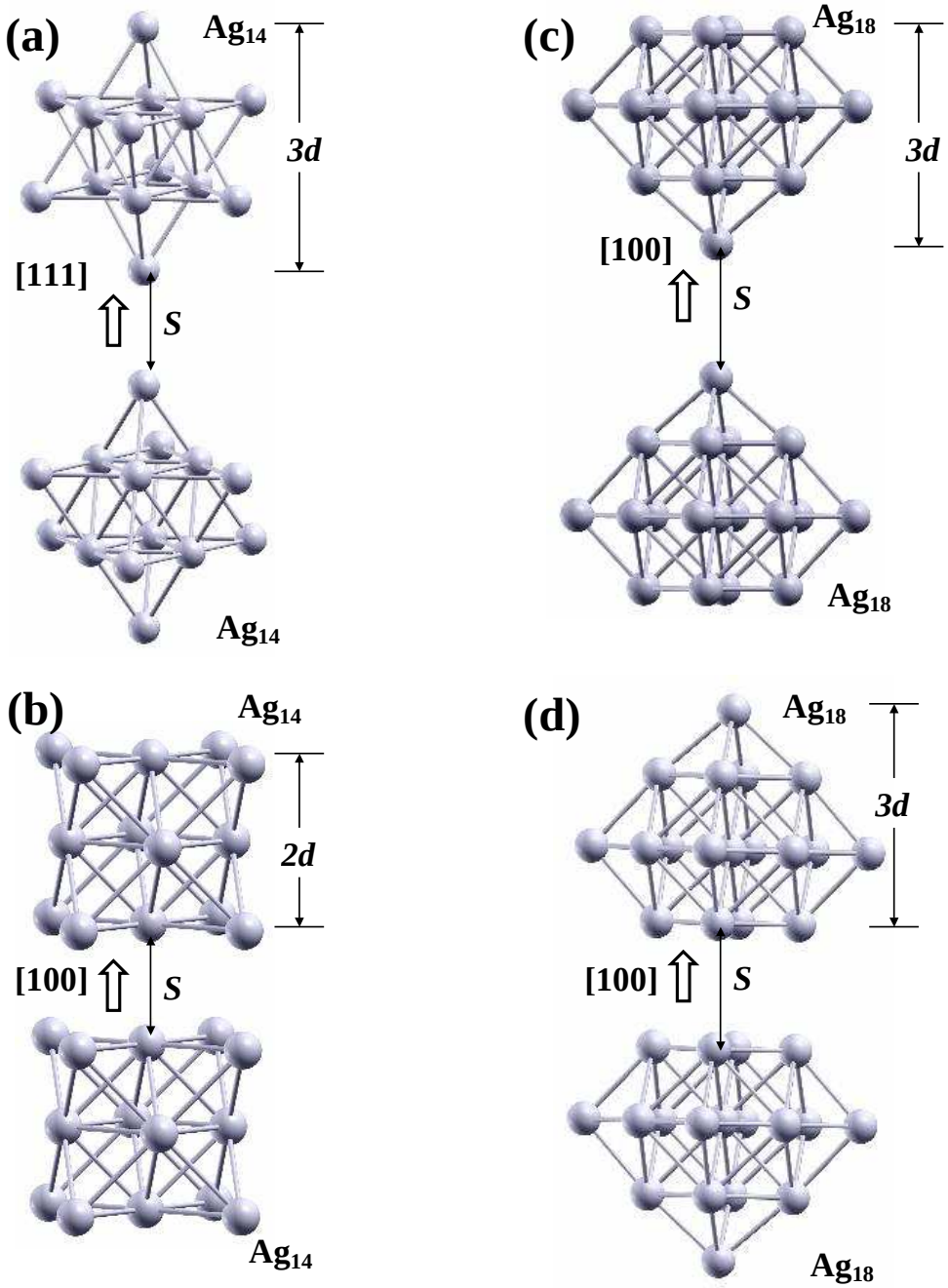

Figure 3.1: Structures of dimers of silver nanoparticles. (a)(c) $(Ag_n)_2$ $(n = 14, 18)$ with t-t orientation, (b)(d) $(Ag_n)_2$ $(n = 14, 18)$ with p-p orientation. $d = 2.2$ Å for $(Ag_{14})_{2,t-t}$, 2.0 Å for $(Ag_{14})_{2,p-p}$, and 1.9 Å for $(Ag_{18})_2$ along both orientations. The dimer axis is along [111] in the t-t and [100] in the p-p orientation of $(Ag_{14})_2$, and [100] in both the t-t and p-p orientations of $(Ag_{18})_2$.

foundation for dealing with interacting electronic systems in their ground satate in terms of the density [66]. They derived a stationary expression for the energy of a system as a functional of the density $\rho(\vec{r})$. The central theorem of DFT states that, apart from an unimportant additive constant, the external potential is uniquely determined by the ground state charge density. The theory implies that the ground state energy of the system is determined by its charge density. Therefore, the correct energy and charge distribution of the ground state can be found by minimizing the energy functional with respect to the charge density.

The energy functional can be written as

$$E[\rho] = \int \rho(\vec{r})v(\vec{r})d^3r + \frac{1}{2}\int\int \frac{\rho(\vec{r})\rho(\vec{r}')}{|\vec{r}-\vec{r}'|}d^3rd^3r' + G[\rho] \tag{3.1}$$

where the first term describes the energy of an electron gas in an external potential $v(\vec{r})$, the second term describes the classical coulomb electron-electron interaction, and the third term is the sum of the kinetic, exchange, and correlation energies.

Based on the energy variational principle of Hohenberg and Kohn, Kohn and Sham derived a set of self-consistent one-particle equations to describe electronic ground states. These equations replace a system of interacting electrons with a gas of noninteracting particles, moving in an effective potential. The effective one-particle potential, $v_{eff}(\vec{r})$, formally takes into account all many-body effects, and it depends on the entire density distribution, $\rho(\vec{r}')$. The total charge density of the system is calculated as the sum of the individual electronic charge densities over all occupied single particle states,

$$\rho(\vec{r}) = \sum_i |\psi_i(\vec{r})|^2 \tag{3.2}$$

where $\psi_i(\vec{r})$ are single wave functions of the noninteracting electron gas. The Kohn and Sham self-consistent one particle equations can be written as follows,

$$(-\frac{\nabla^2}{2} + v_{eff}[\rho(\vec{r})])\psi_i(\vec{r}) = \epsilon_i\psi_i(\vec{r}) \tag{3.3}$$

where the effective potential $v_{eff}[\rho(\vec{r})]$ is given by

$$v_{eff}[\rho(\vec{r})] = v(\vec{r}) + \int \frac{\rho(\vec{r}')}{|\vec{r} - \vec{r}'|} d^3r' + \frac{\delta E_{xc}[\rho]}{\delta \rho(\vec{r})} \tag{3.4}$$

In this equation, the first term represents the external nulcear potential, the second term represents the coulomb potential from the repulsion between electrons, and last term is the exchange-correlation potential. Since the exchange-correlation potential depends on the complicated way on the entire density distribution $\rho(\vec{r}')$, appoximation must be made in order to solve the Kohn-Sham equation. One of the most useful and widely used has been the local density approximation (LDA). The LDA replaces the exchange-correlation potential by one that depends by a simple manner only on the local density $\rho(\vec{r})$ at the point $\vec{r}$. Within the LDA, the exchange-correlation energy functional of the inhomogeneous electron gas is constructed from a parameterized form of the exchange-correlation energy of a homogeneous electron gas with the same charge density. The exchange-correlation energy is written as

$$E_{xc}[\rho] = \int \rho(\vec{r}) \epsilon_{xc}[\rho(\vec{r})] d^3r \tag{3.5}$$

where $\epsilon[\rho(\vec{r})]$ is the exchange and correlation energy per particel of an uniform electron gas. The exchange energy per particle, $\epsilon[\rho(\vec{r})]$, can be approximated by the analytical expression for the homogeneous electron gas [67],

$$\epsilon_x[\rho_\sigma(\vec{r})] = -\frac{3}{4\pi}(6\pi^2 \rho_\sigma(\vec{r}))^{1/3}, \sigma = (\uparrow, \downarrow). \tag{3.6}$$

the correlation energy, $\epsilon_c[\rho(\vec{r})]$, can be constructed on the basis of Monte-Carlo simulations. The calculations presented in thesis used the Perdew-Zunger parameterization of the correlation functional computed by Ceperley and Alder [68].

All-electron calculations are a cumbersome and expensive computational problem, even when using approximate methods such as local density approximation. In order to help reduce the computational burden, one can consider only those electrons that are directly involved in the chemical

bonding. The exclusion of core electrons, which are tightly bound to the nucleus and do not participate in bonding, greatly reduces the number of electrons used in the calculation. In the pseudopotential approximation the effect of core electrons is replaced with an effective potential. Not only does the computational effort get reduced by explicitly dealing only with the outer valence electrons, but the resulting potential is weak and smoothly varying. The Phillips-Kleinman cancellation theorem states that the stong attractive potential between the valence and the core electrons cancels the strong repulsive potential originating from the orthogonality requirements between the valence and the core states [69]. The superposition of the attractive and repulsive contribution results in a relatively weak effective pseudopotential. As the resulting pseudopotential is weak, smoothly varying and has no singularities, it is amenable to simple basis like plane waves or finite difference real-space methods. These properties also facilitate applications to local density calculations because of the absence of rapid changes in the charge density distribution. Computational methods using LDA and the pseudopotential approach are among the most promising techniques for electronic structure calculations [70].

Most of the pseudopotentials used in electronic structure caluculations are generated from all-electron atomic calculations. Using DFT and assuming a spherical screening approximation, this can be done by self-consistently solving the radial Kohn-Sham equations [66]:

$$(-\frac{1}{2}\frac{d^2}{dr^2} + \frac{l(l+1)}{2r^2} + v_{eff}[\rho(r)])rR_{nl}(r) = \epsilon_{nl}rR_{nl}(r) \tag{3.7}$$

where $v_{eff}[\rho(r)]$ is the self-consistent one electron potential, $v_{eff}[\rho(r)] = \frac{Z}{r} + v_H[\rho(r)] + v_{xc}[\rho(r)]$. $v_H[\rho(r)]$ is the Hartree potential, and $v_{xc}[\rho(r)]$ is the local density approximation of the exchange-correlation potential. $R_{nl}(r)$ are the radial wave functions, and $\rho(r)$ is the radial charge density, calculated by summing the electronic charge densities of all occupied states.

In order to construct the pseudopotential, we start by solving the Kohn-Sham equations for the all-electron wavefunction fo the atom. Once the all-electron wave function is obtained, we build the pseudo wave function for the valence electrons. This is done by imposing four general conditions on the pseudo wavefunction. The first condition is that the valence radial pseudo wavefunction

generated from the pseudopotential should be nodeless. Second, the normalized atomic radial pseudo wavefunction should be identical to the normalized radial all-electron wavefunction (for each lth angular momentum state) beyond a chosen cutoff radius r_{cl} [71],

$$R_l^{(pseudo)}(r) = R_{nl}^{(all-e)}(r), r > r_{cl}. \tag{3.8}$$

Third, the integral of the pseudocharge density within r_{cl} should equal to the integral of the all-electron charge density [72],

$$\int_0^{r_{cl}} |R_l^{(pseudo)}(r)|^2 r^2 dr = \int_0^{r_{cl}} |R_{nl}^{(all-e)}(r)|^2 r^2 dr \tag{3.9}$$

The last condition is that the valence all-electron and the pseudopotential eigenvalues must be equal,

$$\epsilon_l^{(pseudo)} = \epsilon_{nl}^{(all-e)} \tag{3.10}$$

The pseudopotentials that meet these conditions are called "norm-conserving pseudopotentials" [72].

We then calculate the pseudopotential from the pseudo wavefunction by inverting the Schrodinger equation:

$$v_l[\rho(r)] = \epsilon_l - \frac{l(l+1)}{2r^2} + \frac{1}{2rR_l^p(r)} \frac{d^2}{dr^2} rR_l^p(r) \tag{3.11}$$

the ionic pseudopotential, $v_{ion,l}(r)$, with different orbital momenta l is obtained by subtracting the Hartree and exchange-correlation potentials for the valence electrons from the total screened potential, $v_l[\rho(r)]$,

$$v_{ion,l}(r) = v_l[\rho(r)] - v_H[\rho^{(pseudo)}(r)] - v_{xc}[\rho^{(pseudo)}(r)] \tag{3.12}$$

The resulting ionic pseudopotential has contributions only from the nucleus and the frozen core elctrons. Within the pseudopotential method the ion core is chemically inert, so this part of the potential can be transfered.

There are many methods for constructing a LDA pseudopotential [71–75]. The flexibility in their construction arises from the fact that the construction for the region $r < r_{cl}$ is not unique. This flexibility can be used to optimize the convergence of the pseudopotentials for the basis fo interest. The calculations presented in this thesis used improved Troullier-Martins potential, generated from the $4d^{10}5s^{1}5p^{0}$ configuration.

Combining pseudopotentials with plane wave basis has proved to be one of the most successful methods for calculating structural and elctronic properties of crystalline materials. However, for localized materials such as clusters, the application of this method is not trivial since their lack of periodicity invalidates the Bloch's theorem. One way of overcoming this difficulty is to use the "supercell" method [76]. In this method, the cluster is isolated in a large cell, and this cell is artificially replicated to impose periodicity on the system. There are several disadvantages in using this method. The plane wave basis not only has to replicate the electronic states of the cluster, but also the vacuum regions imposed by the supercell geometry. Replicating the vacuum can be as expensive as replicating the "real" part of the wavefunction. Other issues to take into account when using this method are the cell-cell interactions and the treatment of charged systems. In the work presented in this thesis, we used a method that combines a higher order finite difference method with the pseudopotential method in real-space without the explicit use of a basis set. It presents numerous advantages for the electronic structure calculations of localized systems such as clusters since no artifacts such as supercell geometries need to be introduced. It is very easy to implement and it offers flexibility in choosing the boundary conditions. Real-space calculations use approximate numerical expressions for space derivatives. On a uniform three dimensional space grid, the derivatives can be respresented by higher order finite difference expansions. A finite difference expansion replaces the derivative of a function with a weighted sum of the function values at neighboring grid points.

An order-N finite difference expansion for the k-th derivative of an arbitary function $f(x)$ is given by [77, 78]

$$\frac{\partial^k f(x)}{\partial x^k}|_x = x_0 \approx \frac{1}{h^k} \sum_{n=-N}^{N} C^k_{N,n} f(x_0 + nh) \tag{3.13}$$

where $C^k_{N,n}$ are the weight coefficients and h is the grid spacing. The weight coefficents are chosen as to minimize the total error of the approximation, assuming that $f(x)$ can be expanded by a power series in h. The coefficients are obtained by representating the function $f(x)$ as a Taylor power series near the point x_0,

$$f(x) = \sum_{i=0}^{\infty} a_i (x - x_0)^i \tag{3.14}$$

The k-th derivative at x_0 is

$$\frac{\partial^k f(x)}{\partial x^k}|_{x=x_0} = k! a_k \tag{3.15}$$

In order to solve the electronic structure problem in real space, the Kohn-Sham equation is set up on a simple uniform three-dimensional grid within a spherical domain. The grid points are described by their coordinates, (x_i, y_i, z_i). Outside the sphere, the electronic wave functions are required to vanish. We use a higher order finite difference expansion to describe the kinetic part fo the Hamiltonian, which contains the Laplacian operator. We approxmiate $\partial^2\Psi/\partial x^2$ at (x_i, y_i, z_i) by [79, 80]

$$\frac{\partial^2 \psi}{\partial x^2} = \sum_{n=-N}^{N} C_n \psi(x_i + nh, y_i, z_i) + O(h^{2N+2}) \tag{3.16}$$

where $N$is the finite difference expansion and h is the grid spacing.

The wave function on the grid, $\psi(x_i, y_i, z_i)$ can be obtained by solving the following secular equation:

$$-\frac{\hbar^2}{2m}[\sum_{n_1=-N}^{N} C_{n_1}\psi_n(x_i+n_1h,y_j,z_k)+\sum_{n_2=-N}^{N} C_{n_2}\psi_n(x_i,y_j+n_2h,z_k)+$$

$$\sum_{n_3=-N}^{N} C_{n_3}\psi_n(x_i,y_j,z_k+n_3h)]+[v_{ion}(x_i,y_j,z_k)+v_H(x_i,y_j,z_k)+ \tag{3.17}$$

$$v_{xc}(x_i,y_j,z_k)]\psi_n(x_i,y_j,z_k)=E_n\psi_n(x_i,y_j,z_k)$$

where v_{ion} is the nonlocal ionic pseudopotential, v_H is the Hartree potential, and v_{xc} is the local density expression of the exchange-correlation potential.

For a given dimer, each of the particles is structurally relaxed so that the maximum magnitude of the force on any atom is smaller than 0.07 eV/Å.

3.4 Electronic Coupling

The strength of the electronic coupling can be measured by the planar charge density λ at the center of the nanogap, defined by $\lambda = |q|/\Delta|_{\Delta\to 0}$, where q is the total charge in the infinitely large slab shown in the inset of Fig. 3.2, and Δ is the thickness of the slab. Fig. 3.2 shows λ as a function of the gap size S, which is measured in the units of the average layer thickness d of the nanoparticle throughout this paper (see Fig. 1). For both particle sizes, the t-t orientation gives a significantly smaller charge density than the p-p orientation. This is because in the former case, only one atom at the tip of each nanoparticle directly faces each other; while in the latter, there are more than one atom. The weakest coupling in $(Ag_{14})_{2,t-t}$ among all four configurations results in its significant differences from others in various physical properties, as illustrated later.

3.5 Optimal Gap Size for Static Polarizability

The linear response of the dimers to an external electric field is expected to be strongly influenced by the coupling between the two nanoparticles. In our study, the response is measured by the static polarizability given by $\alpha_{zz} = \partial P_z(\vec{E})/\partial E_z|_{\vec{E}=0}$, where P_z is the dipole moment of the system along the dimer direction, and $\vec{E} = E_z\hat{e}_z$ is the external electric field. We only consider the α_{zz}

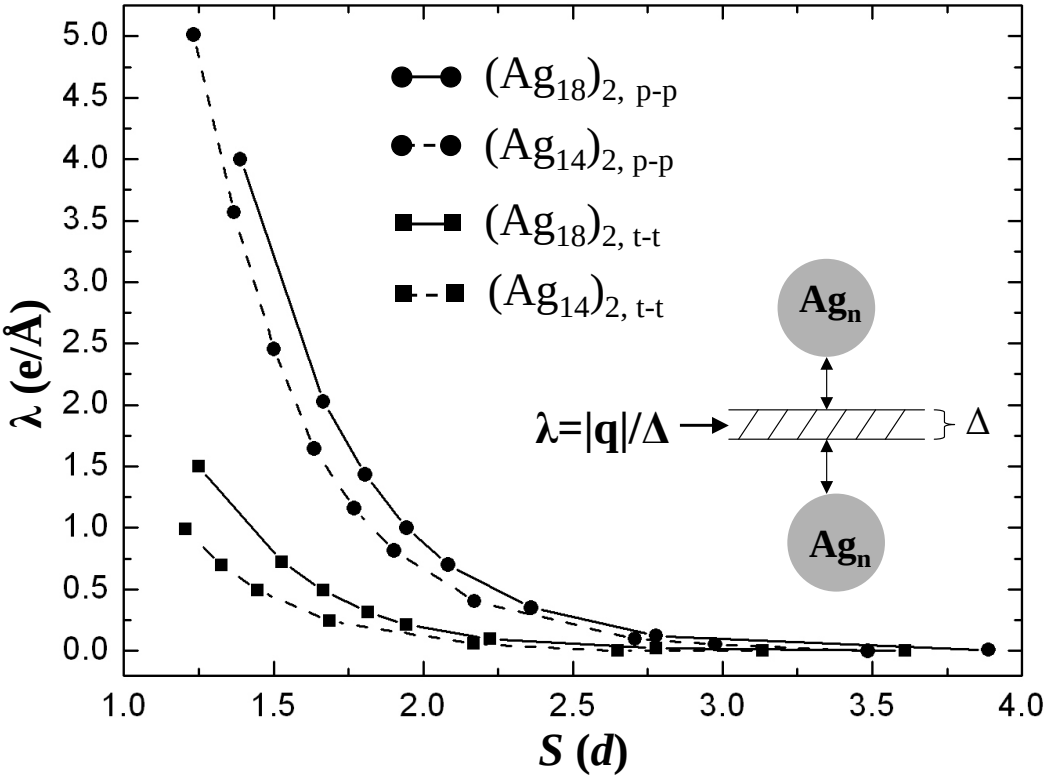

Figure 3.2: Planar charge density λ in the nanogap of $(Ag_n)_2$ ($n = 14, 18$), for various gap sizes S in terms of the average layer thickness d of the corresponding nanoparticle.

component because it is most sensitive to the dimer gap size among all the components. The polarizability was calculated using a finite field method, and the electric field was chosen to be sufficiently small so that the response is in the linear regime (We found that for $(Ag_{18})_2$, when the gap size is large, the response of the system becomes nonlinear even for the smallest field within numerical accuracy. To ensure a linear-response calculation, we have fixed the occupation numbers in each spin component. A study of the nonlinear regime will be presented in the next chapter.) Surprisingly, the polarizability of a single Ag_{14} nanoparticle is almost identical along both the [111] and [100] directions, despite the anisotropic shape of the nanoparticles.

Fig. 3.3 shows α_{zz} as a function of the gap size S, which displays a pronounced peak at the OGS for all four dimer configurations. However, unlike the isolated particle case, the orientation dependence becomes significant when the particles form a dimer: for the same particle size, the t-t orientation gives a significantly higher value of the maximum polarizability and a smaller OGS.

The physics behind this striking result, and the very existence of the OGS is as follows: a bond breaking occurs during the transition from strong to weak electronic coupling between the two nanoparticles as they become far apart. Here the bond refers to the channel for the charge flow between two nanoparticles. When two nanoparticles are very close to each other, a strong bond connecting them exists and charge can flow freely from one particle to the other. In this strong coupling regime, the trend of the polarized charge to recombine decreases with an increasing gap size S, leading to an increasing polarizability. When S continues to increase, the bond breaks down and the flow of charge is discounted, eventually to zero. For a dimer in this regime, the contribution of the classical electromagnetic coupling becomes dominating, leading to the monotonic decrease of the polarizability.

To demonstrate the above argument, we have calculated the transferred charge Q between the nanoparticles as a function of S, as shown in Fig. 3.4 for $(Ag_{18})_{2,t-t}$. As we can see, when S is smaller than the OGS, Q maintains a relatively constant value, while beyond the OGS, Q decreases sharply and eventually turns to zero. On the other hand, Q is clearly nonzero even at 2.5 d, indicating the remaining of a weak bond at this large gap size. The insets of Fig. 3.4 are the corresponding spatial distributions of the induced charge density in the (100) lattice plane containing the dimer axes,

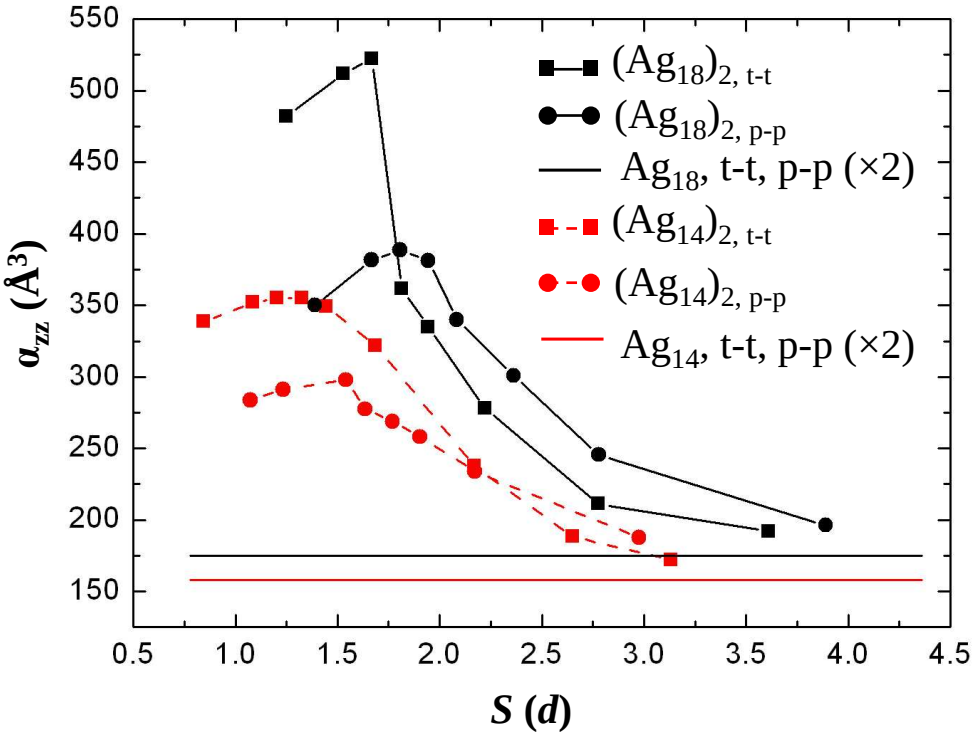

Figure 3.3: Static polarizability α_{zz} of $(\mathrm{Ag}_n)_2$ $(n = 14, 18)$ as a function of S.

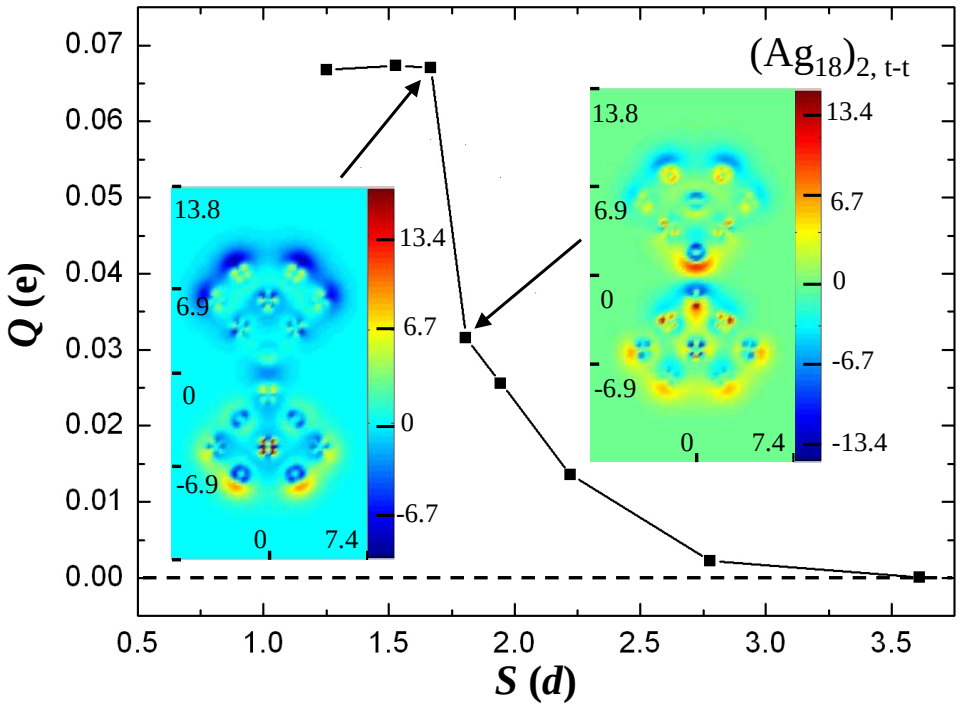

Figure 3.4: Transferred charge Q from one nanoparticle to the other as a function of S in $(Ag_{18})_{2,t-t}$. The magnitude of the applied electric field is 0.013 eV/Å/e. Q is measured in units of e, the charge of an electron. Insets: spatial distributions of the induced charge density in the (100) lattice plane containing the dimer axes, at the OGS and right beyond it. The unit is Å for the spatial coordinates (left) and e/Å^3 for the color bar (right).

at the OGS and right beyond it. There is a dramatic redistribution of charge density when the gap size is beyond the OGS with appreciable amount of charges accumulating near the gap region, which is consistent with our argument that beyond the OGS, the charge ceases to flow between two nanoparticles. Dramatic charge redistributions were also seen in $(Ag_{18})_{2,p-p}$ and $(Ag_{14})_{2,p-p}$. A similar charge redistribution has been reported in a previous study based on the jellium model [15]. On the other hand, we found that unlike $(Ag_{14})_{2,p-p}$, the charge redistribution in $(Ag_{14})_{2,t-t}$ is always a gradual process. Such an orientation dependence is absent in the jellium model.

3.6 Nonmagnetic-magnetic Transition

The electronic coupling not only affects the electronic but also the magnetic properties of the dimer. Fig. 3.5 shows the net magnetic moment μ of the dimer as a function of the gap size S. The distinct feature of all the dimers except for $(Ag_{14})_{2,t-t}$, is the sudden occurrence of a net moment as the two nanoparticles approach each other, although both isolated Ag_{14} and Ag_{18} are nonmagnetic. We note that the net moment emerges at the OGS, beyond which the induced charge density dramatically redistributes.

To understand the appearance of the magnetic moment, we have plotted energy levels near the HOMO-LUMO gap as a function of S for $(Ag_{14})_{2,p-p}$ in Fig. 3.6(a), and $(Ag_{14})_{2,t-t}$ in Fig. 3.6(b). When S is large, the HOMO is at least four-fold degenerate: two are from the spin degrees of freedom and the other two account for the number of identical particles.

As the particles approach each other, the HOMO-LUMO gap decreases and these energy levels split into different branches with the spin degeneracy intact. This splitting is due to the increased coupling between the two particles, corresponding to a bond formation process. When the gap size further decreases, the electronic coupling becomes even stronger, which splits the energy levels into spin-resolved levels, and the original HOMO and LUMO cross each other. In the end, there are three occupied spin-up levels and one occupied spin-down level, giving rise to a net magnetic moment of $2\mu_B$. The splitting into spin-resolved energy levels is in direct analogy with the Heitler-London model for diatomic molecules [81]. On the other hand, in the case of $(Ag_{14})_{2,t-t}$, although

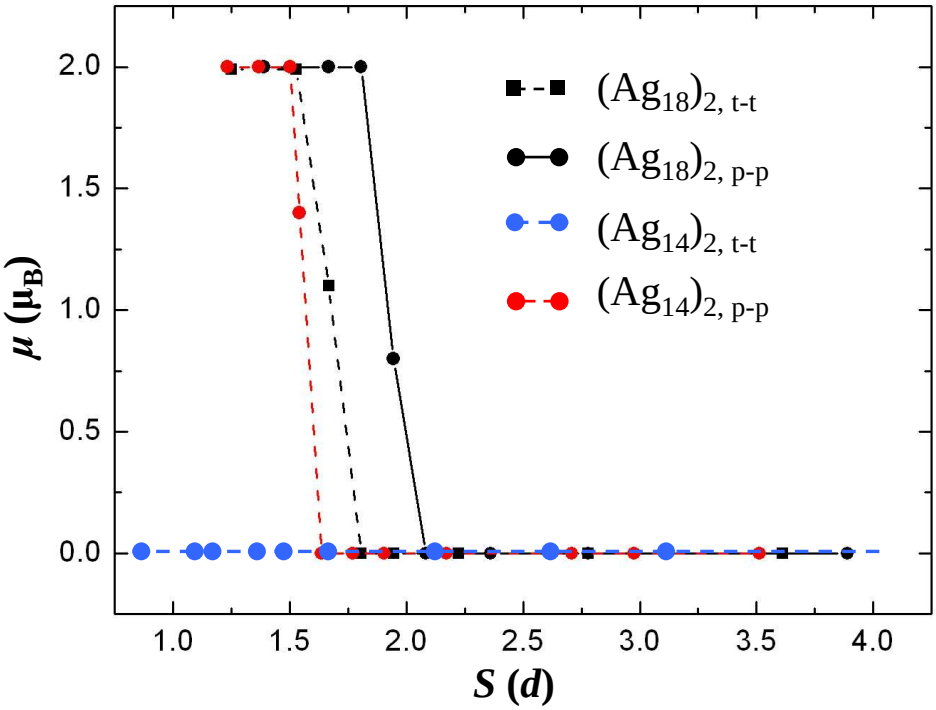

Figure 3.5: Net magnetic moment of $(Ag_n)_2$ $(n = 14, 18)$ with various gap sizes S.

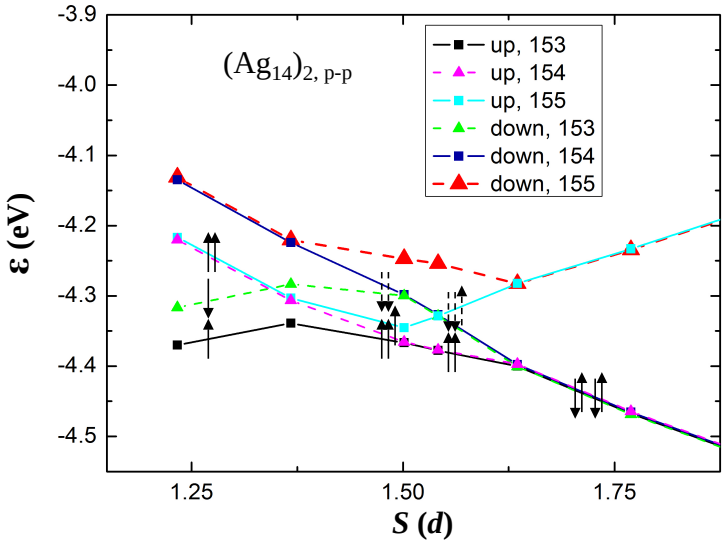

(a)

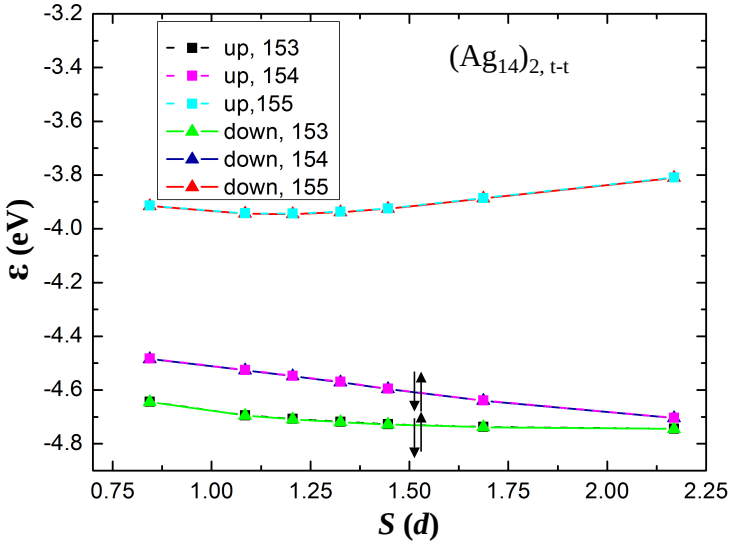

(b)

Figure 3.6: (a) Energy levels around HOMO-LUMO gap of $(Ag_{14})_{2,p-p}$. (b) Energy levels around HOMO-LUMO gap of $(Ag_{14})_{2,t-t}$. In both (a) and (b), a solid arrow pointing up (down) means a spin up (down) level has an occupation of one, while a dotted arrow indicates a fractionally occupied level. The numbers following "up" and "down" in the legends of both (a) and (b) index the electron energy levels.

the HOMO splits into two branches because of the electronic coupling, it is never strong enough (see Fig. 3.2) to lift the spin degeneracy. This is why in this case we observe no appearance of a net magnetic moment.

The simultaneous appearance of magnetic moment and the dramatic redistribution of induced charge density for $(Ag_{14})_{2,p-p}$ and $(Ag_{18})_2$ is not a coincidence. Let us consider a process in which the particles are pulled away from each other. Below and beyond the OGS, the HOMO-LUMO gap remains finite and the occupied wavefunction under external field changes adiabatically with the gap size S. Around the OGS, the HOMO and LUMO cross each other, which breaks the adiabaticity and changes the characteristic of the occupied wavefunction, leading to a dramatic change of the charge density. In the case of $(Ag_{14})_{2,t-t}$, because the HOMO and LUMO do not cross each other, such a dramatic redistribution is absent.

3.7 Implications

The bond breaking picture discussed above is expected to be enlightening in understanding various physical and chemical properties of closely-packed nanoparticle aggregates. One example is SERS [1, 18, 41–43, 59, 60]. As demonstrated above, the electronic coupling can strongly affect the static polarizability of a dimer by modifying its energy spectrum. We expect similar effect on the dynamic polarization as well, which characterizes the optical response of the system. It can be generalized to the SERS when a molecule is trapped in the dimer gap. By changing the gap size, the electronic coupling between the molecule and the nanoparticles can be tuned to make the energy levels match the optical resonance condition, hence the enhanced Raman signal.

The bond breaking also has important implications in transport phenomena. The fact that even at $S = 2.5d$ the electronic coupling is still relevant suggests that a nanowire can be stretched to more than its bulk lattice spacing yet still conducts. Indeed, there are experimental reports of similar phenomena for atomic chains [82, 83, 86]. In addition, the appearance of a net magnetic moment, and particularly the level crossing effect, points out a possible way to generate spin-polarized current in these nanostructures.

Chapter 4

Tunability of the Magnetic Properties of Metal Nanoparticle Dimers in a Nonlinear Dielectric Response Regime

4.1 Motivations

As mentioned in Chapter 3, many interesting phenomena have been observed when nanoparticles are closely aggregated and start to interact with each other [13–15]. Therefore, a solid understanding of the inter-particle coupling is of tremendous significance in both fundamental studies and applications of nanotechnology. A nanoparticle dimer provides the simplest system to investigate how the inter-particle coupling depends on the system geometry and how it affects the physical properties of the system.

Some theoretical studies that focus on the electronic coupling between two metal nanoparticles has been reported recently [15, 63, 64]. However, relatively little has been explored regarding the tunability of external fields on nanoparticle pairs [84, 85]. As described in Chapter 3, we have recently pointed out that the electronic environment in the gap separating a metal nanoparticle dimer gives rise to physics which cannot be surmised from either atomic or bulk phenomenologies [65]. For example, the existence of an optimal gap size (OGS), for which the polarizability of

the dimer takes on a maximum, was established. An issue that immediately comes up is that the presence of an external electric field introduces a new relevant energy scale, which feeds back to the dimer-intrinsic length scale: the Stark shift of the HOMO-LUMO gap. Clearly, if this gap takes on a critical value, the magnetic (spin) degrees of freedom may display unusual properties. Most importantly, the very concept of the OGS leads to the expectation that unique interplay between spin and electronic degrees of freedom may result from tuning the strength of the electric field polarizing the dimer.

This study provides novel insights into the electronic and magnetic degrees of freedom of a metal nanoparticle dimer under the influence of an applied electric field. We establish the existence of a critical separation between the nanoparticles for which the dielectric response switches to its nonlinear regime. The critical values of the field strength and of the nanoparticle separation for which this transition occurs depend strongly on the size of the nanoparticles, as well as on the relative orientation between them. Once the dimer is in the nonlinear regime, its net magnetic moment can be easily tuned by the electric field. This effect is triggered when the Stark-shifted HOMO-LUMO gap reaches a threshold value. Remarkably, even very small fields can change the properties of the dimer dramatically. Therefore, the applied electric field emerges as a new variable to tune the electronic and magnetic properties of nanomaterials, making these systems ideal candidates for constructing multiferroics at the nanoscale.

4.2 Model Dimer System and Approaches

We chose the four types of silver nanoparticle dimers same as those in Chapter 3, as illustrated in Fig. 3.1. We still use DFT as described in section 3.3 of Chapter 3. The interlayer spacing d serves as the unit of length.

4.3 Nonlinear Electric Response

To study the nonlinear electric response, we calculated P_z/E_z, where P_z is the dipole moment of the dimer along the dimer axis direction, and $\vec{E} = E_z\hat{e}_z$ is the external electric field; we only

apply the field along the dimer direction because it is the most sensitive to the dimer gap size. We calculate P_z/E_z for several gap sizes S, and several values of the electric field. For the case of $(Ag_{18})_{2,t-t}$, we found that for modest values of the electric field the system exhibits a linear response to the electric field up to a critical separation, $S = 1.67d$, and beyond that separation, within the numerical accuracy of our method, it switches abruptly to the nonlinear regime, as seen in Fig. 4.1(a). This sudden switch to the nonlinear regime can also be observed from the behavior of P_z/E_z vs. S for different values of E_z, as shown in Fig. 4.1(b) for the case of $(Ag_{18})_{2,t-t}$. As a reference we also calculate the values of P_z/E_z for the linear regime [65]. From these curves it can be observed that the response of the system deviates from the linear regime at a critical separation, $S = 1.67d$. A similar behavior is observed for other types of dimers, such as $(Ag_{14})_{2,t-t}$ in Fig. 4.2.

The nanoparticle dimers exhibit a clear transition to the nonlinear regime which depends on two variables: the separation between the particles, and the value of the electric field. The interplay of these two variables can be seen from a plot of the critical field, E_c, which is the minimum field needed for the system to enter the nonlinear regime at a given separation, as a function of S, as shown in Fig. 4.3. For the case of $(Ag_{18})_{2,t-t}$, the transition to the nonlinear regime is very sharp, and beyond a critical separation, $S = 1.67d$, the response of the system to the electric field is nonlinear, even for the smallest field we can calculate within the numerical accuracy of the method.

We know from the Stark effect observed in atoms, that the electric field causes changes in the energy spectrum. Therefore, we looked at the energy levels of the dimers with different applied electric fields to investigate the effect of the electric fields on the dimer systems. Fig. 4.4 shows the energy levels around the HOMO for $(Ag18)_{2,t-t}$ for E=0 and for E=0.026 eV/Å/e respectively. When we focus on $S = 1.95d$, the HOMO-LUMO gap changes from finite to practically zero when the electric field changes from E=0 to 0.026 eV/Å/e. This change of HOMO-LUMO gap results in the occupation of the LUMO to be changed from zero to finite, and so the response of the dimer to external field is nonlinear. Similar changes in the HOMO-LUMO gaps as a function of the applied electric field are observed for (Ag14)2 p-p, (Ag18)2 p-p, and (Ag14)2 t-t, as these dimers enter the nonlinear regime.

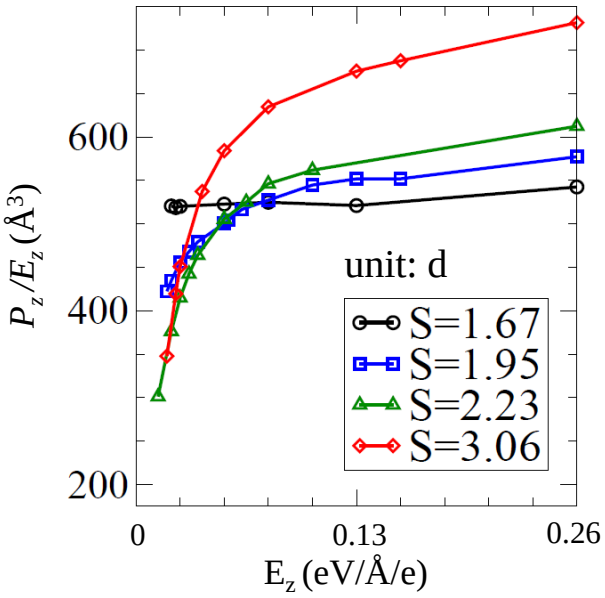

(a)

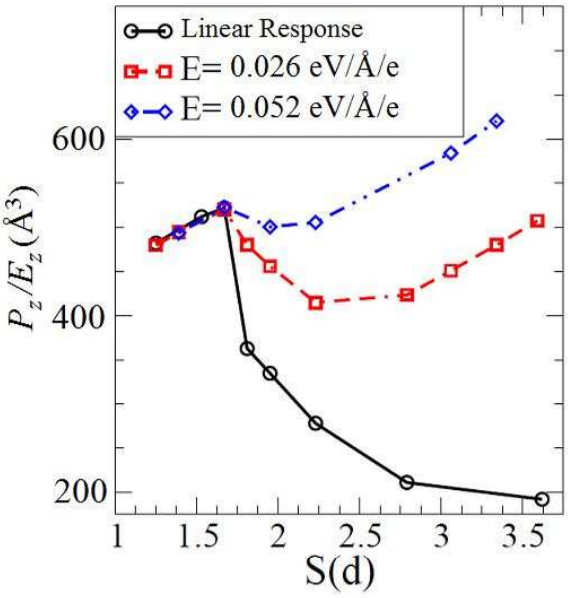

(b)

Figure 4.1: Dipole moment divided by the strength of external electric field $\vec{E} = E_z\hat{e}_z$ of silver nanoparticle dimer $(Ag_{18})_{2,t-t}$ (a) versus electric field for different gap size S (b) versus gap size S for different electric field strength $E = |\vec{E}|$.

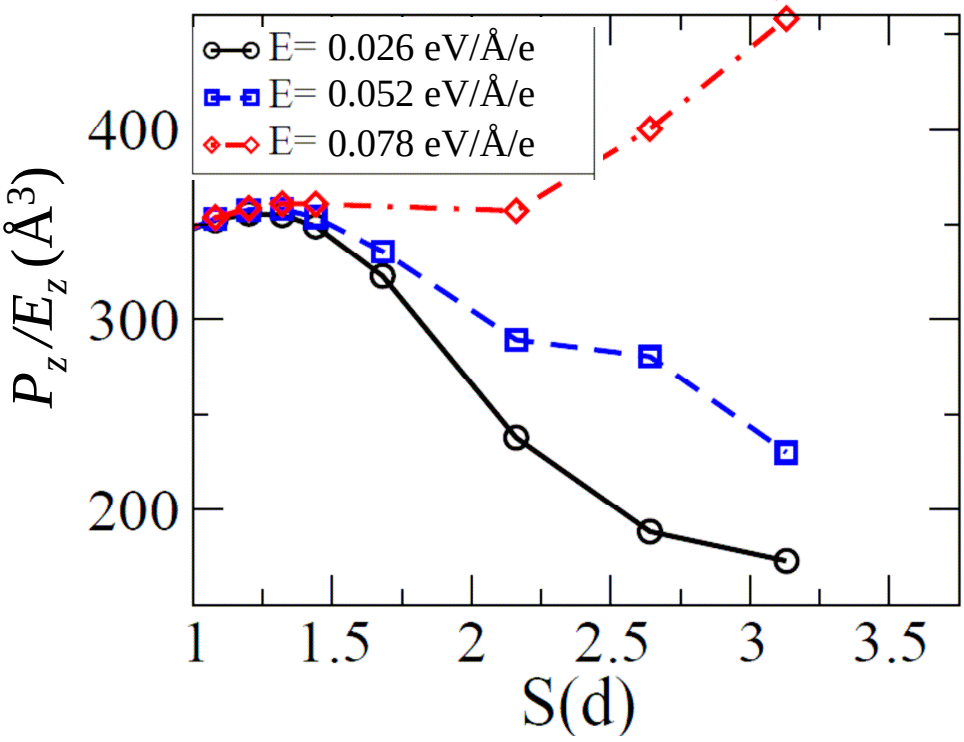

Figure 4.2: Dipole moment divided by the strength of external electric field $\vec{E} = E_z\hat{e}$ of silver nanoparticle dimer $(Ag_{14})_{2,t-t}$ as a function of gap size S for different electric field strength.

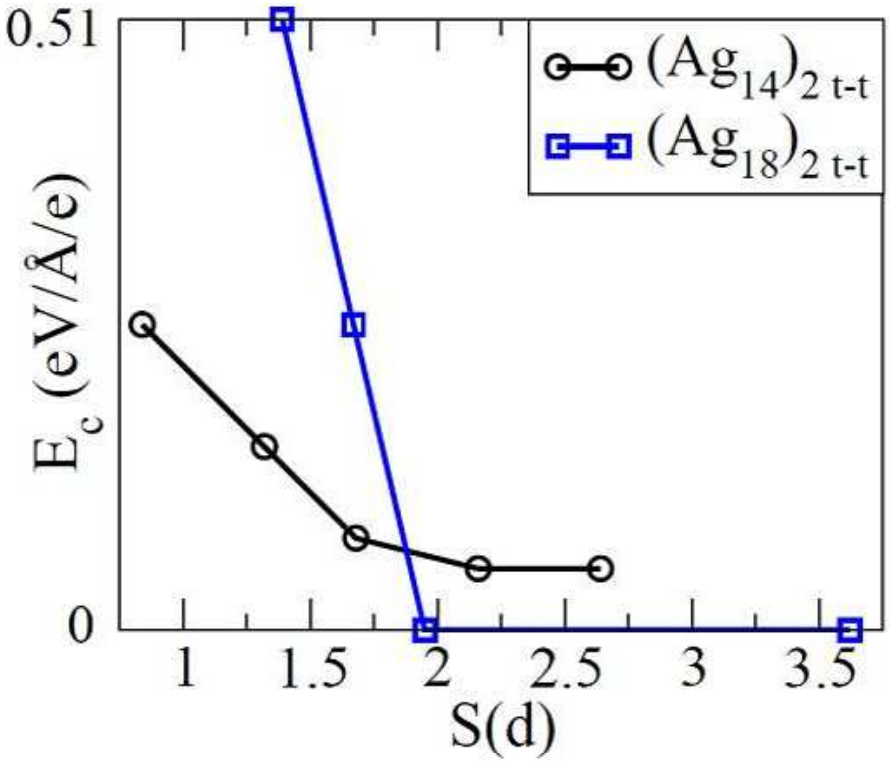

Figure 4.3: Critical electric field E_c separating linear and nonlinear response as a function of gap size S for silver nanoparticle dimers $(Ag_{14})_{2,t-t}$ and $(Ag_{18})_{2,t-t}$.

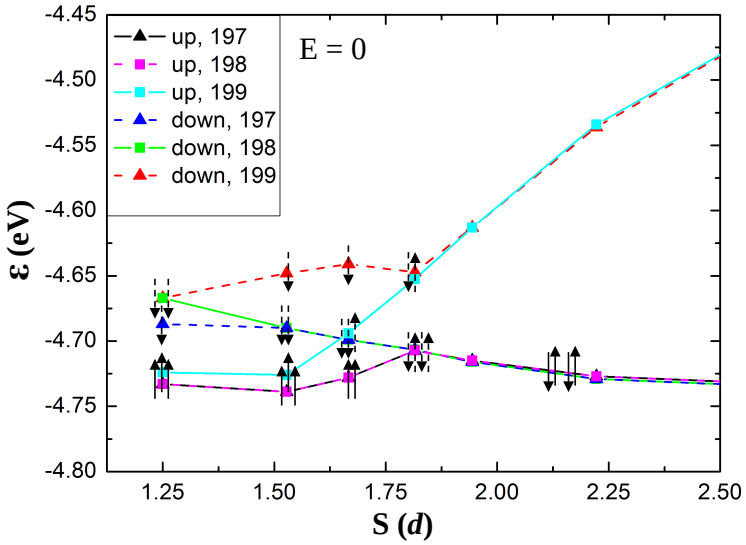

(a)

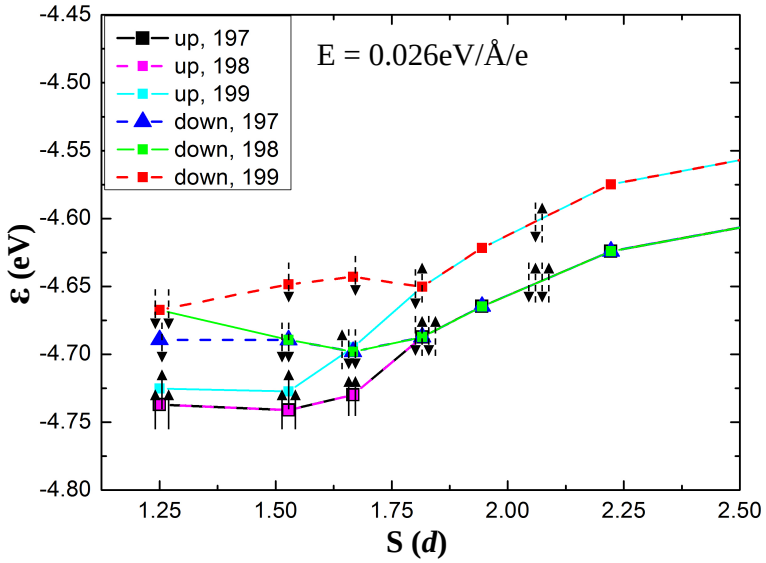

(b)

Figure 4.4: Energy levels around HOMO-LUMO gap of $(Ag_{18})_{2,t-t}$, for (a) without electric field (b) with electric field. In both (a) and (b), a solid arrow pointing up (down) means a spin up (down) level has an occupation of one, while a dotted arrow indicates a fractionally occupied level. The numbers following "up" and "down" in the legends of both (a) and (b) index the electron energy levels.

4.4 Magnetic Property

The changes in the electronic structure induced by the electric field can affect many physical properties of the dimer, in particular, the magnetic properties. Since the net magnetic moment of a nanoparticle depends sensitively on the value of its HOMO-LUMO gap, the magnetic properties may be tuned by varying the strength of the electric field polarizing the dimer. In the absence of an external field, the electronic coupling between the nanoparticles affects the magnetic properties of the dimer [65]. While each isolated nanoparticle has zero net magnetic moment, there is a sudden occurrence of the magnetic moment at the OGS between the nanoparticles. The magnetic moment of the dimer can then be changed from zero to two by varying the gap size between the nanoparticles [65]. The external electric field constitutes a new variable to tune the magnetic moment of the system. In the linear regime, for a given gap size, the dimer has a constant value of the magnetic moment, and it is not dependent on the value of the applied field. However, the net magnetic moment of the system exhibits remarkable changes when the system enters the nonlinear regime. Fig. 4.5(a) shows the net magnetic moment of $(Ag_{18})_{2,t-t}$ as a function of the applied electric field for two separations for which the dimer is in the nonlinear regime even for the smallest fields we can calculate, $S = 1.95d$ and $S = 2.23d$. In Fig. 4.5(a) is also shown as a reference the magnetic moment for a separation in which the dimer is in the linear regime, $S = 1.39d$, for the values of the electric field used here. From Fig. 4.5(a), it can be seen that when the dimer is in the linear regime, ($S = 1.39d$), the net magnetic moment remains constant at a value of two for all the values of the applied electric field. For $S = 1.95d$ and $2.23d$, the net magnetic moment changes as a function of the applied field, going from zero at E=0 to two at E=0.26 eV/Å/e.

The changes of the magnetic moment with the varying electric field are a consequence of the changes in the energy spectrum as a function of the electric field. For a certain value of S, a sufficiently large field can split the spin energy levels and causes the crossing of spin up(down) LUMO and spin down(up) HOMO, which is shown in Fig. 4.5(b). This will change the occupation of different spin levels, and consequently the value of the net magnetic moment changes. The ability of tuning the magnetic moment by applying modest values of the electric field is a unique

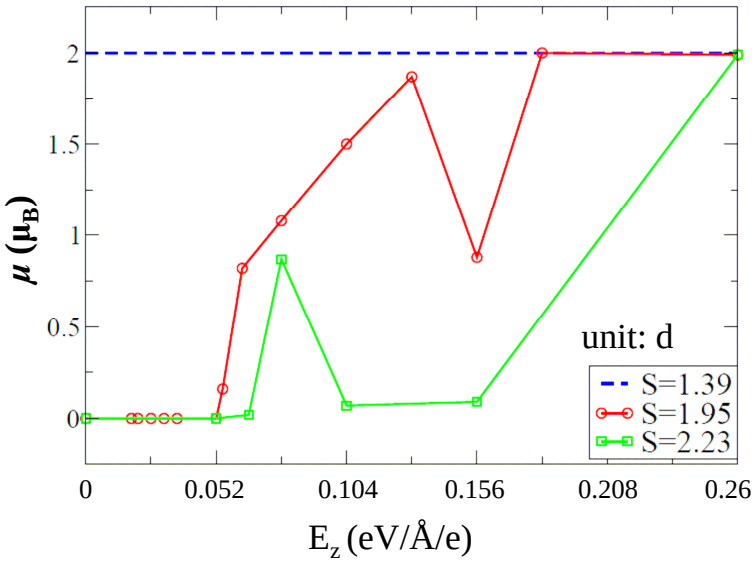

(a)

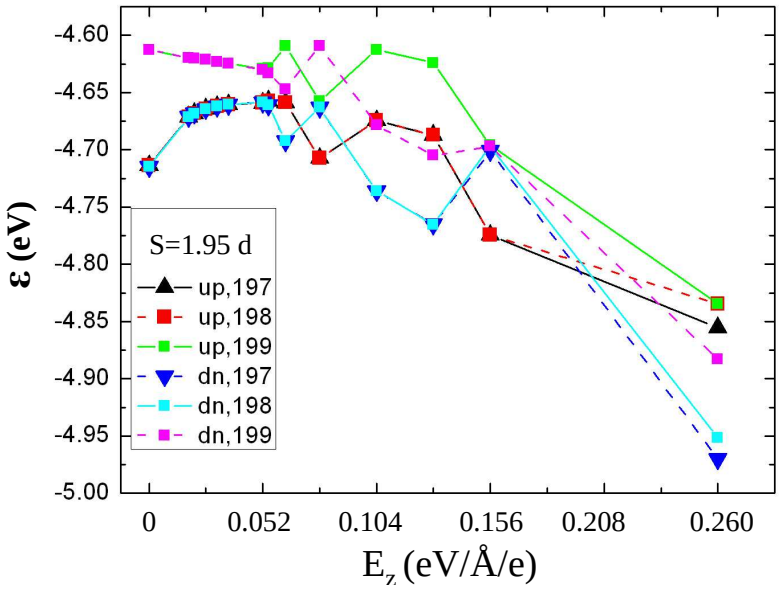

(b)

Figure 4.5: (a) Net magnetic moment of $(Ag_{18})_{2,t-t}$ vs external electric field, for different gap sizes S. (b) The energy levels corresponding to S=1.95d.

property of the dimer made possible by the weak electronic coupling between the nanoparticles. The field-induced changes in the energy spectrum of the dimer, and therefore in its HOMO-LUMO gap can have dramatic changes in the physical and chemical properties of the system, which can be enlightening for making new tunable multifunctional devices [89, 90]. For instance, the tunability of the magnetic moment of the dimer by an applied electric field makes nanoparticle aggregates appealing candidates for the construction of spin-based electronic devices. Also, nanoparticles offer several advantages over the conventional bulk materials due to the extra degrees of freedom they posses, such as the size of the nanoparticles, their relative orientation, and the gap size. It is important to note that the possibility of tuning the magnetic moment only occurs when the system is in the nonlinear regime, because they are all rooted in the change of occupation number at the LUMO or HOMO.

Chapter 5

Electromagentic Enhancement From Nanoparticle Dimer Arrays

5.1 Ordered Scalable SERS

To date, single molecule SERS has been mostly obtained experimentally only from a few Raman active metal nanoparticle (solid or shell) dimers randomly distributed among large ensembles of nanoparticels; therefore, only random spatial correlation exists among the dimers. However, as the field of nanofabrication advances, highly ordered metal nanoparticle dimer arrays with delicate tunability in geometry have started to emerge [91–96]. The ordered spatial correlation among the dimers are expected to produce collective phenomena of plasmon among all the dimers in the array. Thus, such ordered dimer arrays not only offer new opportunities to expand fundamental studies of SERS, but also broaden the range of SERS application, particularly in chemical and biological sciences.

To study the collective phenomena of plasmon, my colleagues and I investigated both one-dimensional (1D) and two-dimensional (2D) dimer arrays composed of solid nanoparticles and nanoshells, as illustrated in Fig. 5.1. The 2D array illustrated in Fig. 5.1(b) consists of geometrically identical 1D dimer arrays aligned parallel to each other. For clarity, each 1D array in the 2D arrays will be called a chain with a given chain number. The total chain number in the 2D array is taken

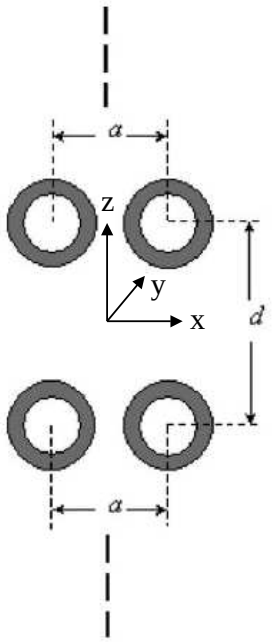

(a)

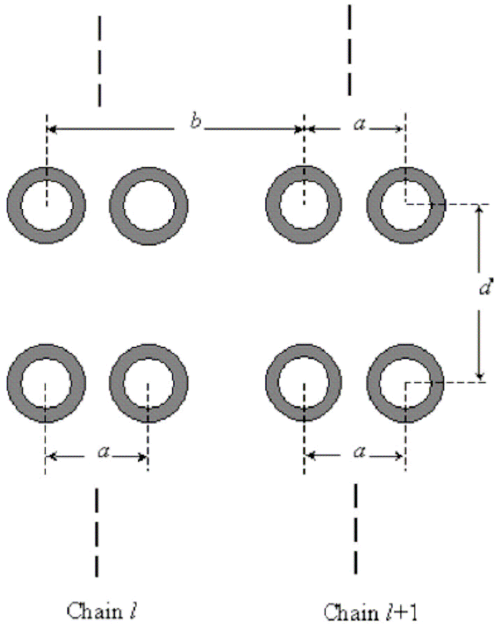

(b)

Figure 5.1: (a)1D and (b)2D nanoparticle dimer arrays. The dielectric core has a radius of r_1, and the metal shell has an inner and outer radius of r_1 and r_2. The solid nanoparticle corresponds to $r_1 = 0$.

to be sufficiently large, so that each chain can be regarded as identical in its optical response. The polarization of the incident light is parallel to the dimer axes, and the wave vector $\vec{k}$ is perpendicular to both the dimer axes and the array (1D) or chain (2D) direction. $\omega = ck$ is the frequency where c is the light speed in vacuum, and the wavelength $\lambda = 2\pi/k$. The investigation is within the frame of classical electromagnetics and shows that as a result of photonic effect, which arises from long-range electromagnetic interaction between the dimers in the array: (I) the EM enhancement alone can reach up to 10^{14}, which is two orders higher than the corresponding isolated dimer; (II) finite size effects exist in 1D arrays. The finite size effects refer to two aspects: (I) EM enhancement at the center of a given dimer oscillates with the length of a 1D array, and (II) for a given 1D array with a fixed length, the EM enhancement oscillates along the array. However, finite size effects do not exist in 2D arrays.

5.2 Generalized Mie Theory

To investigate the EM enhancement in dimer arrays illustrated in Fig. 5.1, we used the highly accurate generalized Mie theory [44, 45], combined with coupled dipole approximation (CDA) (to be explained in the next section) [97, 98].

The Mie theory was developed by Mie in 1908, which analytically describes the scattering of electromagnetic wave by spherical structures [12]. The basic idea of Mie theory is to decompose the field into normal modes namely vectorial spherical harmonics, which are constructed by the traditional spherical harmonics [12, 44, 45]:

$$\vec{M}_{mn}^{(j)}(\vec{r}) = (\hat{r},\hat{\theta},\hat{\phi}) \begin{pmatrix} 0 \\ \frac{1}{sin\theta}\frac{\partial}{\partial\phi} \\ -\frac{\partial}{\partial\theta} \end{pmatrix} z_n^{(j)}(kr) Y_n^m(\theta,\phi)$$

$$\vec{N}_{mn}^{(j)}(\vec{r}) = (\hat{r},\hat{\theta},\hat{\phi}) \begin{pmatrix} n(n+1)z_n^{(j)}(kr) \\ \frac{\partial}{\partial r}\left\{rz_n^{(j)}(kr)\right\}\frac{\partial}{\partial\theta} \\ \frac{\partial}{\partial r}\left\{rz_n^{(j)}(kr)\right\}\frac{1}{sin\theta}\frac{\partial}{\partial\phi} \end{pmatrix} \frac{1}{kr} Y_n^m(\theta,\phi) \tag{5.1}$$

where $z_n^{(j)}$ corresponds to j_n,y_n,$h_n^{(1)}$,$h_n^{(2)}$ for $j = 1,2,3,4$ respectively [29]. For an isolated spherical structrue, when the incident field is one of the normal modes with the angular momentum (n,m), the scattered field is another normal mode with the same angular momentum (n,m), multiplied by a coefficient namely Mie scattering coefficient [99]. Note here that we take the center of the sphere as the origin of $\vec{r}$, and $k = \frac{\omega}{c}$.

For the plane wave $\vec{E}_p(\omega,\vec{r}) = \vec{E_0} \cdot e^{i\vec{k}\cdot\vec{r}}$ as the incident wave, the normal modes serving as the basis of decomposition are $\vec{M}_{mn}^{(1)}$ and $\vec{N}_{mn}^{(1)}$:

$$\vec{E}_p(\omega,\vec{r}) = \sum_{n=1}^{\infty}\sum_{m=-n}^{n}\left[p_{mn}^0\vec{N}_{mn}^{(1)}(\vec{r}) + q_{mn}^0\vec{M}_{mn}^{(1)}(\vec{r})\right] \tag{5.2}$$

Since the mode $N_{mn}^{(1)}$ is scattered to $N_{mn}^{(3)}$, and $M_{mn}^{(1)}$ is scattered to $M_{mn}^{(3)}$, the wave scattered by an isolated sphere is written as [45]:

$$\vec{E}_{psc}(\omega,\vec{r}) = \sum_{n=1}^{\infty}\sum_{m=-n}^{n}\left[v_n \cdot p_{mn}^0\vec{N}_{mn}^{(3)}(\vec{r}) + u_n \cdot q_{mn}^0\vec{M}_{mn}^{(3)}(\vec{r})\right] \tag{5.3}$$

where v_n and u_n are Mie scattering coefficients [99].

When the plane wave is scattered by an aggregate of spheres, the effective incident field for one sphere is the summation of the plane wave and the scattered field from all other spheres. To apply Mie theory to the aggregate of spheres, we focus on one sphere at one time and perform a coordinate transformation for the scattered field from other spheres to this particular sphere [100]:

$$\vec{N}^{(3)}_{mn}(\vec{r}_s) = \sum_{\nu=1}^{\infty}\sum_{\mu=-\nu}^{\nu}[A^{\mu\nu}_{mn}(s,t)\vec{N}^{(1)}_{\mu\nu}(\vec{r}_t) + B^{\mu\nu}_{mn}(s,t)\vec{M}^{(1)}_{\mu\nu}(\vec{r}_t)]$$
$$\vec{M}^{(3)}_{mn}(\vec{r}_s) = \sum_{\nu=1}^{\infty}\sum_{\mu=-\nu}^{\nu}[B^{\mu\nu}_{mn}(s,t)\vec{N}^{(1)}_{\mu\nu}(\vec{r}_t) + A^{\mu\nu}_{mn}(s,t)\vec{M}^{(1)}_{\mu\nu}(\vec{r}_t)] \tag{5.4}$$

where $\vec{r}_s$ and $\vec{r}_t$ are the same spatial point but in the coordinate system of sphere s and t respectively. This approach is called generalized Mie theory (GMT).

Specifically when applying GMT to dimer arrays shown in Fig. 5.1, my colleagues and I studied one special case: ideally infinitely long 1D array with translational symmetry. We used this special case to show that when dimers are far away from each other, CDA may be used to study problems computationally too demanding for GMT, such as finite size effects discussed in later sections.

For the 1D dimer array containing infinite number of dimers, the scattered field decomposed into vectorial spherical harmonics is written as:

$$\vec{E}_{sc}(\omega,\vec{R}) = \sum_{\eta=1,2}\sum_{n=1}^{\infty}\sum_{m=-n}^{m=n}\sum_{l=1}^{N\to\infty}[\alpha^{\eta}_{mn}(l)\cdot\vec{N}^{(3)}_{mn}(\vec{r}^{\eta}_l) + \beta^{\eta}_{mn}(l)\cdot\vec{M}^{(3)}_{mn}(\vec{r}^{\eta}_l)] \tag{5.5}$$

where η represents different spheres in each individual dimer, l is the index of each dimer, $\alpha^{\eta}_{mn}(l)$ and $\beta^{\eta}_{mn}(l)$ are expansion coefficients, N is the total number of dimers in the array and approaches to infinity in this special case. $\vec{R}$ is defined relative to the center of the whole array (see Fig. 5.1(a)), and $\vec{r}^{\eta}_l = \vec{R} + (N/2 - l + 0.5)d\cdot\hat{z} + (\eta - 1.5)a\cdot\hat{x}$ is defined relative to the center of the ηth sphere in the lth dimer. Invoking the periodic boundary condition, we have $\gamma^{\eta}_{mn}(l) = \sum_h \widetilde{\gamma}^{\eta}_{mn}(h)\cdot exp(ihld)$, where $\gamma = \alpha, \beta$, while $h = (2\pi/Nd)s$ is the wave vector defined within the first Brillouin zone, and s is given by $-N/2 \le s < N/2$ (here we have assumed N is even for convience).

The expansion coefficients $\widetilde{\alpha}^{\eta}_{mn}(h)$ and $\widetilde{\beta}^{\eta}_{mn}(h)$ are further determined by:

$$\widetilde{\alpha}^{\eta}_{mn}(h) = v_n\{p^0_{mn}\delta_{0,h} + \sum_{\nu=1}^{\infty}\sum_{\mu=-\nu}^{\nu}[\widetilde{\alpha}^{\eta}_{\mu\nu}(h)\cdot(\sum_{\bar{l}} exp(ih\bar{l}d)\cdot A^{\mu\nu}_{mn}(\bar{l},\eta\eta))$$
$$+\widetilde{\beta}^{\eta}_{\mu\nu}(h)\cdot(\sum_{\bar{l}} exp(ih\bar{l}d)\cdot B^{\mu\nu}_{mn}(\bar{l},\eta\eta)) + \widetilde{\alpha}^{\xi}_{\mu\nu}(h)\cdot(\sum_{\bar{l}} exp(ih\bar{l}d)\cdot A^{\mu\nu}_{mn}(\bar{l},\eta\xi))$$
$$+\widetilde{\beta}^{\xi}_{\mu\nu}(h)\cdot(\sum_{\bar{l}} exp(ih\bar{l}d)\cdot B^{\mu\nu}_{mn}(\bar{l},\eta\xi))]\}$$

$$\widetilde{\beta}^{\eta}_{mn}(h) = u_n\{q^0_{mn}\delta_{0,h} + \sum_{\nu=1}^{\infty}\sum_{\mu=-\nu}^{\nu}[\widetilde{\alpha}^{\eta}_{\mu\nu}(h)\cdot(\sum_{\bar{l}} exp(ih\bar{l}d)\cdot B^{\mu\nu}_{mn}(\bar{l},\eta\eta))$$
$$+\widetilde{\beta}^{\eta}_{\mu\nu}(h)\cdot(\sum_{\bar{l}} exp(ih\bar{l}d)\cdot A^{\mu\nu}_{mn}(\bar{l},\eta\eta)) + \widetilde{\alpha}^{\xi}_{\mu\nu}(h)\cdot(\sum_{\bar{l}} exp(ih\bar{l}d)\cdot B^{\mu\nu}_{mn}(\bar{l},\eta\xi))$$
$$+\widetilde{\beta}^{\xi}_{\mu\nu}(h)\cdot(\sum_{\bar{l}} exp(ih\bar{l}d)\cdot A^{\mu\nu}_{mn}(\bar{l},\eta\xi))]\} \tag{5.6}$$

where $A^{\mu\nu}_{mn}(\bar{l},\eta\xi)$ and $B^{\mu\nu}_{mn}(\bar{l},\eta\xi)$ are the coefficients of the coordinate transform fron the origin of the ξth sphere in the lth dimer to the ηth sphere in the lth dimer, with $\eta,\xi = 1,2$ and $\bar{l} = l' - l$ summing over all the relative positions of the spheres. $A^{\mu\nu}_{mn}(\bar{l},\eta\xi)$ and $B^{\mu\nu}_{mn}(\bar{l},\eta\xi)$ have the same meaning as the coefficients in Eq. 5.4, just written differently. Note that by definition, $A^{\mu\nu}_{mn}(0,\eta\eta) = 0$ and $B^{\mu\nu}_{mn}(0,\eta\eta) = 0$. In our calculations, n and ν are truncated to the maximum multipole value of L, and $\bar{l}$ is truncated to the maximum number of neighboring dimers. Detailed tests show that the choices of $L = 20$ and $\bar{l} = 200$ will guarantee adequate numerical convergence in most cases.

5.3 Coupled Dipole Approximation

When the incident light wavelength and separation between dimers in an array are much larger than the spatial dimension of the dimers, the interaction between dimers can be described by dipole-dipole coupling. Using CDA, the photonic effect due to the long-range EM interaction between dimers can be separated out in the study of EM enhancement of the whole array.

In CDA, the optical response of an array to the incident light is represented by the excited electric dipole $\vec{p}_n$ associated with individual dimer n, pointing to the polarization direction of the

incident light which is also the dimer axes. Referring $\alpha(\omega)$ as the $\alpha_{zz}(\omega)$ component of the dynamic polarizability tensor of the identical dimers in an array, we have

$$\vec{p}_n(\omega) = \alpha(\omega) \cdot \vec{E}^n_{tot}(\omega) \tag{5.7}$$

where $\vec{E}^n_{tot}(\omega)$ is the total electric field acting on the dimer given by the superposition of dipolar fields from all other dimers and the incident field $\vec{E}^n_i(\omega)$. Further more, we have for $\vec{E}^n_{tot}$,

$$\vec{E}^n_{tot} = \vec{E}^n_i + \sum_{m \neq n} \frac{e^{ik \cdot r_{nm}}}{4\pi\epsilon_0 r^3_{nm}} \{k^2 \vec{r}_{nm} \times (\alpha \vec{E}^m_{tot}) \times \vec{r}_{nm} + \frac{1 - ikr_{nm}}{r^2_{nm}} [3\vec{r}_{nm}(\vec{r}_{nm} \cdot \alpha \vec{E}^m_{tot}) - r^2_{nm} \alpha \vec{E}^m_{tot}]\} \tag{5.8}$$

where $k = 2\pi/\lambda$, $\vec{r}_{nm}$ is the displacement vector from the center of dimer m to n, $r_{nm} = |\vec{r}_{nm}|$, ϵ_0 is the permittivity of free space, and m runs through all the dimers except n. The individual terms in the summation represent the dipolar field propagating from dimer m to n.

For the 1D dimer arrays in Fig. 5.1(a), we obtain from Eq. 5.8:

$$\vec{E}^n_{tot} - \sum_{m \neq n} R_{nm}(\omega) \cdot \vec{E}^m_{tot} = \vec{E}^n_i \tag{5.9}$$

$$R_{nm}(\omega) = \frac{\alpha(\omega) \cdot e^{i\omega|n-m|d/c}}{4\pi\epsilon_0} [(\frac{\omega}{c})^2 \frac{1}{|n-m|\, d} + i(\frac{\omega}{c})(\frac{1}{|n-m|\, d})^2 - (\frac{1}{|n-m|\, d})^3] \tag{5.10}$$

In Eq. 5.10, $n, m = 1, 2, ..., N$. On the right hand side of Eq. 5.10, the first term dominates in the regime $|n-m|\, d << \lambda$, the third term dominates in the regime $|n-m|\, d >> \lambda$, while in the regime $|n-m|\, d \approx \lambda$, all three terms are important.

When applying CDA to 2D array illustrated in Fig. 5.1(b), the term $\sum_{m\neq n} R_{nm}(\omega)\cdot\vec{E}^m_{tot}$ in Eq. 5.9 is replaced by $\sum_{m\neq n} R_{nm}(\omega)\cdot\vec{E}^m_{tot}+\sum_m \Delta R_{nm}(\omega)\cdot\vec{E}^m_{tot}$, where

$$\Delta R_{nm}(\omega)=2\sum_{l>0}\frac{\alpha(\omega)}{4\pi\epsilon_0}e^{i\frac{\omega}{c}\sqrt{(lb)^2+(m-n)^2d^2}}\times\{(\frac{\omega}{c})^2\frac{(m-n)^2d^2}{[(lb)^2+(n-m)^2d^2]^{3/2}} \tag{5.11}$$

$$-i(\frac{\omega}{c})(\frac{[2(lb)^2-(m-n)^2d^2]}{[(lb)^2+(m-n)^2d^2]^2}+\frac{[2(lb)^2-(m-n)^2d^2]}{[(lb)^2+(n-m)^2d^2]^{5/2}}\}$$

Note that the term $\sum_m \Delta R_{nm}(\omega)\cdot\vec{E}^m_{tot}$ represents the propagation of electric dipolar field from dimers in all other chains to dimer n in chain 0, and so $n=m$ is included in the term.

5.4 Combine GMT and CDA

As mentioned in section 5.3, CDA can be used to separate out the long-range photonic effect when dimer arrays are studied. On the other hand, the intrinsic optical response from each of the individual dimer can be studied using GMT, as mentioned in section 5.2. The EM enhancement of a dimer within an array can be calculated by a two step process, which reflects the superposition of the photonic effect on top of the intrisic enhancement associated with an isolated dimer. In the first step, GMT is used to calculate the enhancement $M_i(\omega)$ and dynamic polarizability $\alpha(\omega)$ of an isolated dimer, while in the second step, CDA is used to calculate the additional enhancement $M_a(\omega)=\left|\vec{E}_{tot}(\omega)\right|^4/\left|\vec{E}_i(\omega)\right|^4$. The total EM enhancement from an array is $M_{em}(\omega)=M_i(\omega)\times M_a(\omega)$, because $M_i(\omega)=\left|\vec{E}_{loc}(\omega)\right|^4/\left|\vec{E}_{tot}(\omega)\right|^4$. This approach is highly accurate as long as the incident light wavelength and separation between dimers are much larger than the spatial dimension of the dimer, which is verified by a full GMT calculation applied to ideally infinite 1D dimer arrays as mentioned in section 5.2.

5.5 Giant Electromagnetic Enhancement from Nanoshell Dimer Arrays

As mentioned in section 5.1, nanoparticle dimer arrays can have giant EM enhancement much higher than the corresponding isolated dimer. On the other hand, as mentioned in chapter 1, nanoshell consisting of a thin metal film wrapping a dielectric core can be more advantageous than solid nanoparticle in terms of EM enhancement. So in our study, we focus on nanoshell dimer arrays, but will also compare them to the arrays of solid nanoparticles. The dielectric core of the nanoshell is chosen to be silica, with a dielectric constant of $\epsilon = 2.56$. The materials of the shell is silver, which is widely used for surface plasmon and SERS. The frequency dependence of the dielectric function of the silver is approximated by the experimental data for bulk silver unless otherwise specified [101]. This approximation is supported by recent experimental data [102], though the imaginary part of the dielectric function of a metal shell can be different from its bulk value due to factors such as electron scattering at the interfaces [103].

Fig. 5.2(a) shows the EM enhancement M_{em} versus wavelength λ at the location half way between the shell centers of a dimer in a 1D nanoshell array with the fixed shell geometry of $(r_1 = 35nm, r_2 = 38nm)$ but different inter-dimer distances d. The surface-surface distance between the two spheres of an individual nanoshell dimer is $1nm$ here. For every d, there are multiple enhancement peaks. The number of dimers in the arrays is ideally infinite, and Fig. 5.2(a) is calculated soly by GMT described by Eq. 5.6. The maximum enhancement of $M = 4.5 \times 10^{13}$ is obtained for the optimal inter-dimer distnace of $d = 950nm$, above which the enhancement factor decreases from the maximum value. Note that, as d changes from 216 to 950 nm, the maximum enhancement peak also exhibits a weak red shift resulting from a delicate long-range collective photonic effect.

For comparison, the intrinsic EM enhancement of an isolated dimer with the same shell geometry as that of the dimers in the array, is shown in Fig. 5.2(a). The maximum enhancement of $M_i = 5 \times 10^{12}$ for the isolated dimer is about one order of magnitude smaller than the enhancement for the optimal dimer array. In general, for each nanoshell dimer geometry of (a, r_1, r_2), one can

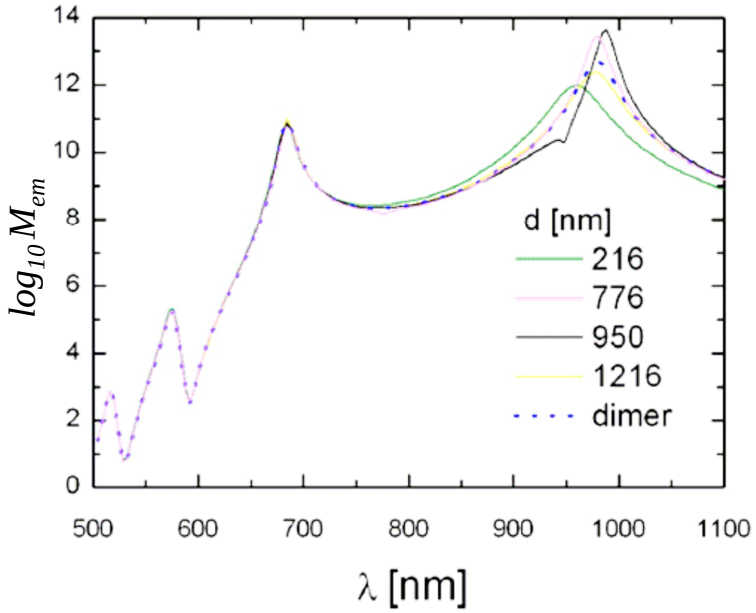

(a)

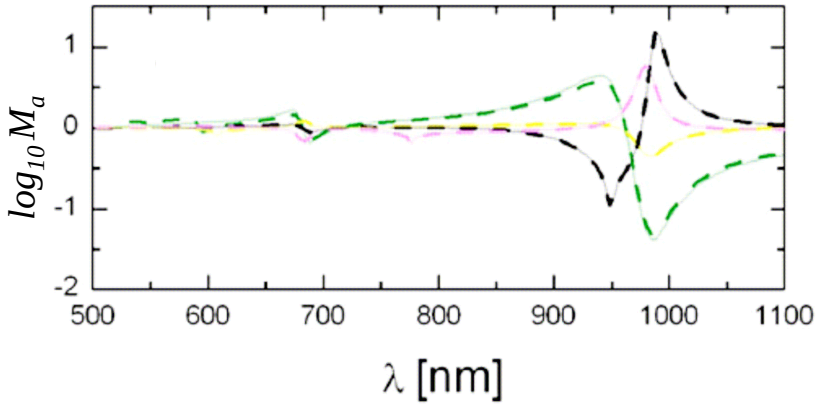

(b)

Figure 5.2: (a) EM enhancements vs the wavelength of the incident light at the location half way between the two centers of a metal nanoshell dimer in dimer arrays of different inter-dimer distances.(b) The additional enhancements due to long-range photonic effect.

always optimize the inter-dimer distance in the array structure to gain 1-2 orders of magnitude of additional enhancement on top of that from the isolated dimer. The additional enhancement is shown in Fig. 5.2(b) for different array geometries. When the additional enhancement is sufficiently large and also near the resonant wavelength for maximum enhancement from the isolated dimer, a net enhancement over the isolated dimer value can be achieved from the array, as in the case of $d = 776$ and $950nm$. Such additional enhancement is due to the long-range photonic effect mentioned in section 5.3. Due to its far-field nature, the additional enhancement is substantially smaller in magnitude than the intrinsic enhancement from the isolated dimer itself. Nevertheless, since the resonant wavelength for the additional enhancement is not necessarily the same as that for the intrinsic enhancement of an isolated dimer, a shift in the resonant wavelength of the whole array from that of the isolated dimer may occur, as shown in Fig. 5.2(a),for the cases $d = 216$ and $960nm$.

It has been shown previously that the plasmon resonance frequency of an isolated metal nanoshell strongly depends on its geometry. Since the plasmon modes are largely responsible for the EM enhancement in SERS, we expect additional tunability in the SERS resonance frequency due to the shell geometry of a nanoshell dimer array. Fig. 5.3 shows the EM enhancement in arrays of nanoshell dimers with the same inner radius of $r_1 = 35nm$ but with different outer radii of $r_2 = 38$, 40, and $43nm$. The corresponding optimal inter-dimer distances are determined to be $d = 950$, 785, and $701nm$, respectively. The resonant wavelength has a blue shift of about $260nm$ when the outer radius of the shell increases from $r_2 = 38nm$ to $r_2 = 43nm$. The typical EM enhancement of around 10^{13} achievable within a broad region of the resonant frequency is a very appealing feature of the shell arrays as templates for SERS measurements with single molecule sensitivity. In particular, as shown in Fig. 5.3(b), the effective "hot volume", define by the collection of the hot spots in the nanogap region with an enhancement factor of 10^{10} or higher, is about $1713nm^3$ for $r_2 = 38nm$, thereby providing a great potential for ultra-sensitive molecular spectroscopy by SERS.

We also compared the results from nanoshell dimer arrays with those from other related arrays structures. Fig. 5.4 contrasts our simulation results for an array of solid silver dimers with identical dimer geometry of ($a = 77nm, r_2 = 38nm$) as for the dimer shells, except for the value r_1 (0

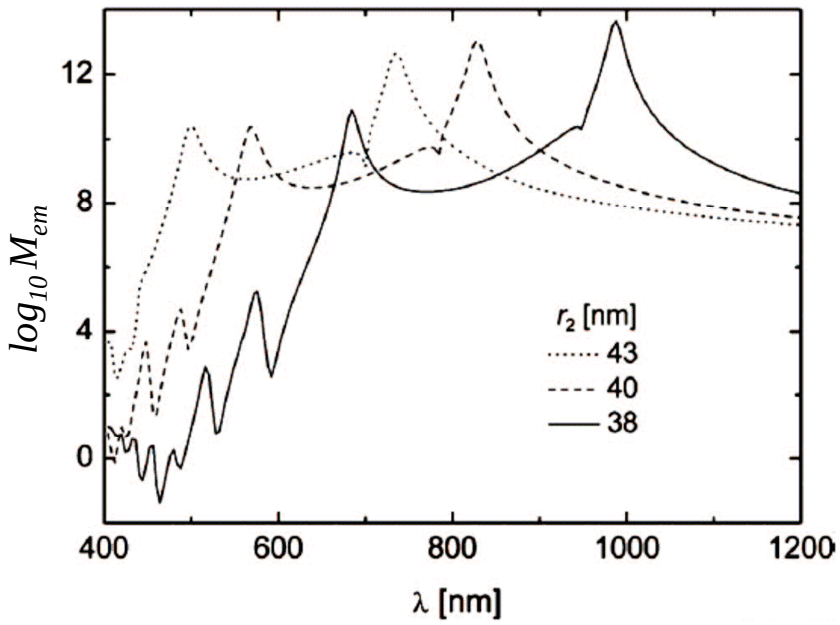

(a)

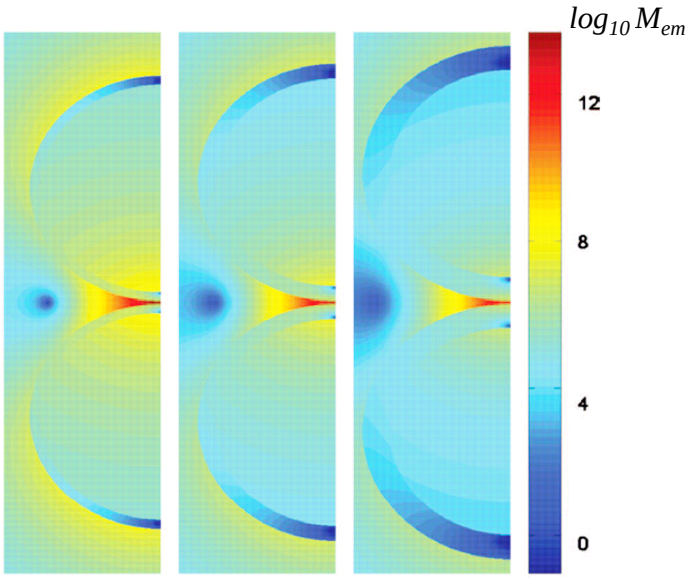

(b)

Figure 5.3: (a) Same as in 5.2, but with different outer radii of the nanoshells.(b) Color illustration of the EM enhancement in the symmetry plane defined by the dimer axes and the array direction, for the same geometries as in (a) (namely, $r_2 = 38nm$ (left),$40nm$ (middle), $43nm$ (right)), and at the different resonance wavelength of 988, 828 and 736 nm, respectively.

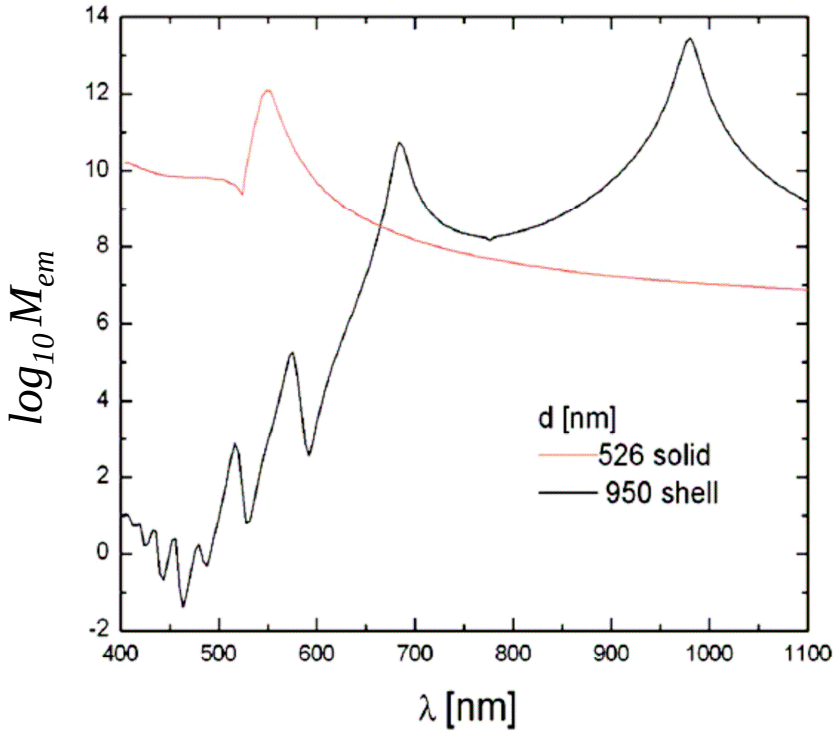

Figure 5.4: Comparison of the EM enhancement from a 1D array of solid spherical dimers and nanoshell dimers, respectively, as specified in the text. The different array structures require different inter-dimer distances for maximal enhancement, as indicated.

versus $35nm$), and different optimal inter-dimer distances for maximal enhancement. The nanoshell dimer array not only yields around 2 orders of magnitude higher enhancement than the solid dimer array, but also induces a dramatic shift in the resonance frequency. This result confirms the large enhancement discovered in nanoshell dimers. The dramatic shift in the resonance frequency also renders nanoshell desirable templates for SERS in the infrared range.

As mentioned above, since the dielectric function of a nanoshell can differ quantitatively from its bulk value because electron scattering at the interfaces may introduce additional broadening, we study here how the spectra is affected by such scattering. Empirically, using the Drude Model [103], the dielectric function of the nanoshell can be described based on the bulk dielectric function, $\epsilon_{Ag}(l,\omega) = \epsilon_{Ag}(\omega) + {\omega_B}^2/(\omega^2 + i\omega\Gamma_\infty) - {\omega_B}^2/[\omega^2 + i\omega(\Gamma_\infty + \Gamma_s)]$, where $\epsilon_{Ag}(\omega) = \epsilon_{Ag}(\omega)_{interband} + (1 - \omega_B^2/(\omega^2 + i\omega\Gamma_\infty))$ is the dielectric function of bulk silver. $\Gamma_\infty = v_F/l_\infty$ is the collision frequency of conduction electrons in bulk silver, with $v_F = 1.39 \times 10^6 m/s$ the Fermi velociy and $l_\infty = 52nm$ the bulk mean free path [104]. Γ_s is the added elecron collision frequency due to interface scattering. With no rigorous way to determine Γ_s at the present, we study quantitatively the effects of additional broadening on top of the standard bulk value by increasing the total electron collision frequency by 100% and 200% respectively. The results are shown in Fig. 5.5, for the nanoshell dimer array with radii ($r_1 = 35nm, r_2 = 38nm$) and optimal inter-dimer distances. When compared with the results for $\Gamma = 0$, the maximum enhancement is lowered by 1 and 1.5 orders of magnitude for doubled and tripled broadening, respectively. Nevertheless, the maximum enahncement for either case is still well above 10^{11}. We therefor stress that, whereas such additional broadening would indeed lower the overall enhancement factor as expected, the two most salient features associated with the nanoshell dimer array geometry, namely, the distinct shift of resonant frequency into near infrared region and the collective photonic effect, remain valid.

We also considered the case where the geometry of the nanoshells is unchanged ($r_1 = 35nm, r_2 = 38nm$), but the nanoneck distance is increased from 1 to $3nm$. Detailed calculations show that, at this larger gap separation, the maximum enhancement is decreased to $M_{em} = 3.7 \times 10^{11}$, but the effective "hot volume" remains essentially the same (namely, changed from 1713-1730nm^3). Such a

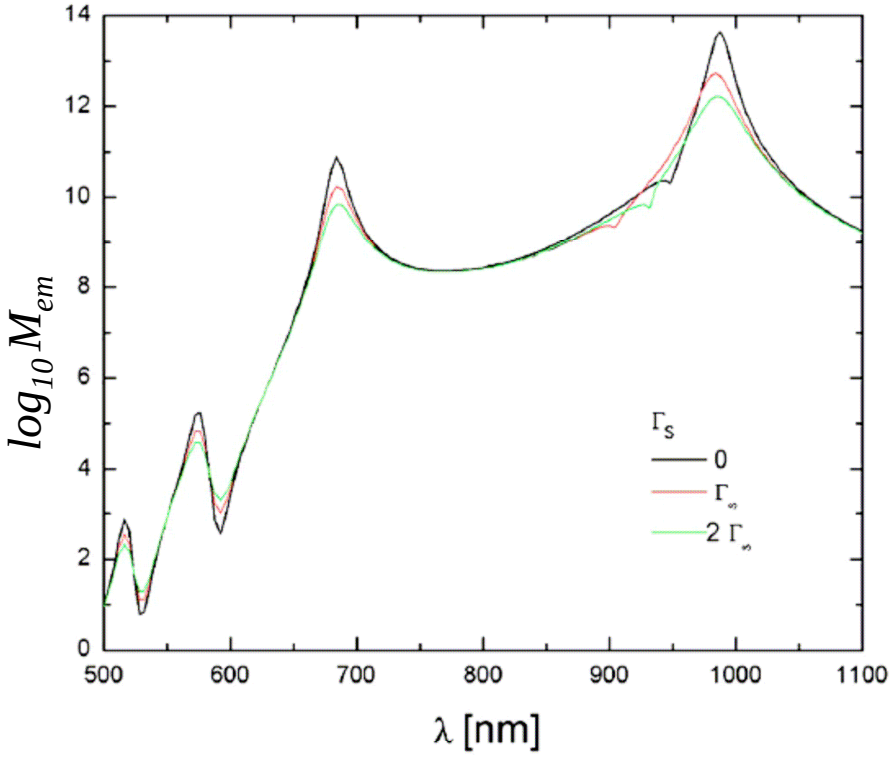

Figure 5.5: EM enhancement vs wavelength for different broadening in the nanoshell dimer arrays, with shell geometry given by ($r_1 = 35nm, r_2 = 38nm$). For $\Gamma_s = 0, \Gamma_\infty, 2\Gamma_\infty$, the optimal interdimer distance is $d = 950$, 906 and $932nm$, respectively.

large hot volume at the $3nm$ gap separation makes the structures even more appealing for potential applications in ultra-sensitive molecular spectroscopy by SERS.

When our study extended to 2D nanoshell dimer arrays, as illustrated in Fig. 5.1(b), we found that the EM enhancement can be even higher than 1D arrays, reaching a value over 10^{14}. Fig. 5.6 displays the EM enhancement M_{em} vs wavelength for the 2D array, which contains dimers with a geometry identical to that of Fig. 5.2(a).

5.6 Finite Size Effect on Electromagnetic Enhancement in Dimer Arrays

As mentioned in section 5.1, the finite size effect exists in 1D dimer arrays. Fig. 5.7 shows the results for the maximum EM enhancement at the center of the central dimer of a 1D array with a varying total number of nanoshell dimers N in the array. All the nanoshells in the arrays are identical to the and have the same inner radius of $35nm$ and outer radius of $38nm$. The center-to-center distance within a dimer is $a = 77nm$, while the inter-dimer distance is $d = 990nm$. The resonant wavelength is found to be exclusively around $996nm$ for all the arrays of different N. The enhancement shows distinct oscillatory behavior with respect to the dimer number N, and the oscillation period is about $\Delta = 350$ dimers. Fig. 5.8(a) and 5.8(b) display the EM enhancements along a given dimer array of a fixed total length $N = 195, 370, 545$ and 2570, respectively. Here the enhancements are again oscillatory, but with a period roughly half of that shown in Fig. 5.7. The oscillation period in Fig. 5.8(a) is $\Delta' = 173$ dimers for $N = 370$ and 545, while in Fig. 5.8(b) the oscillations are well described with a period of $\Delta' = 166$ dimers as long as they are away from either end of the dimer array.

The oscillation period in Fig. 5.7 can be semi-quantitatively explained by applying the translational invariance approximation to Eqs. 5.9 and 5.10. It has been checked that at the center of the array, the translational invariance approximation gives essentially the same EM enhancements as directly obtained from Eqs. 5.9 and 5.10. With the translational invariance, we have

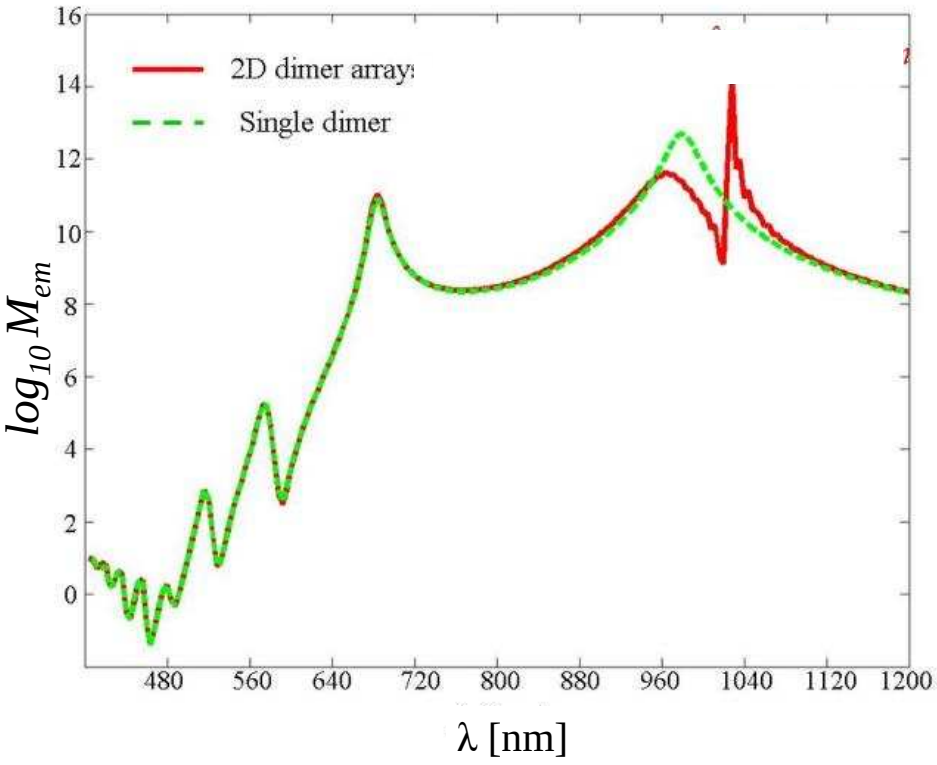

Figure 5.6: EM enhancement from 2D nanoshell dimer array. Each dimer has the same geometry as those in Fig. 5.2(a). The separation between adjacent dimers d is $1020nm$, and the separation between adjacent arrays b is $720nm$.

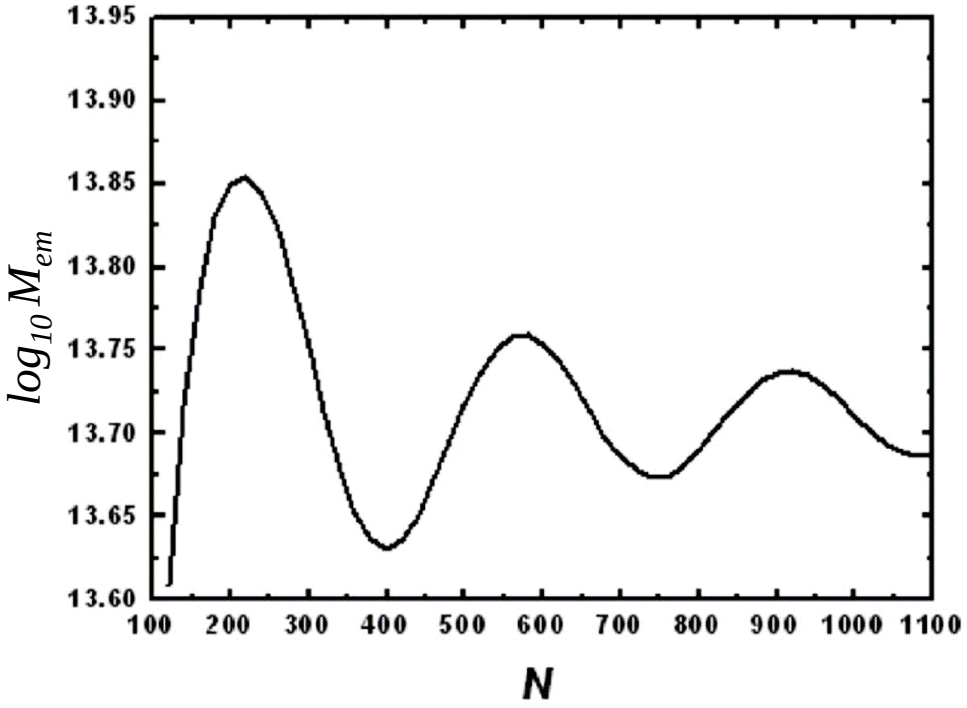

Figure 5.7: Oscillatory EM enhancements vs total dimer number N from 1D nanoshell dimer arrays, all with the same interdimer spacing of $990nm$ and at the resonant wavelength of $996nm$.

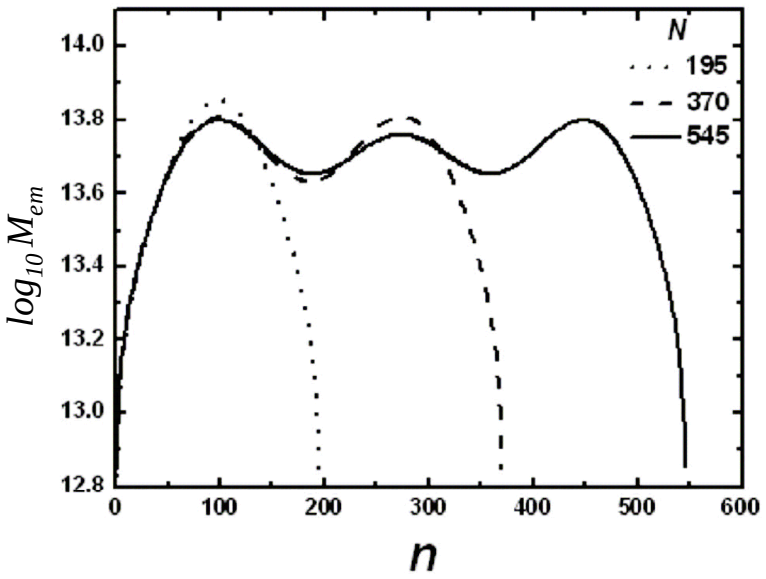

(a)

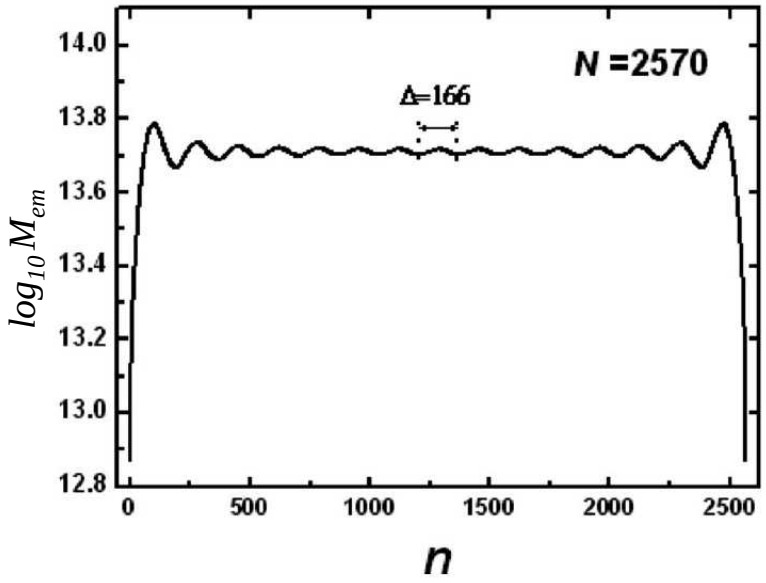

(b)

Figure 5.8: Oscillatory EM enhancements from 1D nanoshell dimer arrays, all with the same interdimer spacing of $990nm$ and at the resonant wavelength of $996nm$. (a) and (b) Variations along the dimer array, but with different total dimer numbers. n refers to the individual dimer in a particular array.

$\vec{E}^{n}_{tot}(\omega_{res}) = \vec{E}^{0}_{tot}(\omega_{res})$ for all n, where ω_{res} is the resonant frequency, and the additional EM enhancement on each dimer can be written as

$$M_a(\omega_{res}) = \frac{1}{|1 - 2 \cdot \sum_{m=1}^{(N-1)/2} R_{m0}(\omega_{res})|^4} \tag{5.12}$$

where the summation in Eq. 5.12 is given by

$$\begin{aligned}
\sum_{m=1}^{(N-1)/2} R_{m0}(\omega_{res}) &= \sum_{m=1}^{(N-1)/2} \frac{\alpha(\lambda_{res}) \cdot e^{i2\pi \cdot md/\lambda_{res}}}{4\pi\epsilon_0} [(\frac{1}{\lambda_{res}})^2 \frac{1}{m \cdot d} + i\frac{1}{\lambda_{res}}(\frac{1}{m \cdot d})^2 - (\frac{1}{m \cdot d})^3] \\
&\approx \sum_{m=1}^{(N+2\lambda_{res}/\delta-1)/2} \frac{\alpha(\lambda_{res}) \cdot e^{-i2\pi \cdot m\delta/\lambda_{res}}}{4\pi\epsilon_0} [(\frac{1}{\lambda_{res}})^2 \frac{1}{m \cdot d} + i\frac{1}{\lambda_{res}}(\frac{1}{m \cdot d})^2 - (\frac{1}{m \cdot d})^3]
\end{aligned} \tag{5.13}$$

From the upper limit of the summation in the last line of Eq. 5.13, we see that the slight mismatch δ between the inter-dimer distance d and resonant wavelength λ_{res} results in the oscillatory EM enhancements with a period $\Delta \approx 2(\lambda_{res}/\delta)$ in N where $\delta = \lambda_{res} - d$. Given $(\delta/\lambda_{res}) = (6/996) = (1/166)$, we have $\Delta \approx 332$, while its difference from the period 350 shown in Fig. 5.7 comes from the parts other than the exponential factor in $R_{m0}(\omega_{res})$ and the edge effect of the finite array. Similarly, the ratio $(\delta/\lambda) = (1/166)$ is also reflected in the periodic distribution of the enhancement along the 1D arrays shown in Figs. 5.8(a) and 5.8(b). The above explanation is further validated by the observation that in Fig. 5.8(b), the oscillation period $\Delta' = 166$ is well defined near the central part of sufficiently long dimer array. It should be noted that the oscillation periods in Figs. 5.8(a) and 5.8(b) are only roughly half of that in Fig. 5.7. In fact, the oscillations in Figs. 5.8(a) and Figs. 5.8(b) are understood directly from Eqs. 5.9 and 5.10, with $\Delta' \approx (\lambda_{res}/\delta)$ as the period of enhancement withine an array of a fixed length; while those in Fig. 5.7 are understood from Eqs. 5.12 and 5.13, with $\Delta \approx 2(\lambda_{res}/\delta)$ as the period. This conclusion is generic for a variety of 1D nanoparticle arrays that are similar to the specific type studied here.

However, the oscillation does not exist in 2D arrays. Fig. 5.9 shows the EM enhancement at the center of the central dimer in each chain of the 2D arrays for varying number of dimers in each chain, all at the resonant frequency. In these calculations, we have truncated $l = 200$ where l is the chain index in Eq. 5.11. The convergence with respect to the truncation of l has been checked. We observe oscillatory enhancements when the total number of dimers in each chain is rather small ($N < 400$), mainly due to edge effects. When $N > 400$, the oscillatory nature disappears, and the EM enhancment factor is essentially a constant of 9×10^{13}, higher than the maximum enhancement from the 1D arrays studied above.

The absense of oscillatory EM enhancement in the 2D case results from the nonlinear dependence of the phase interference on the distance between dimers of different chains. Specifically, when translational invarieance is also applied in the chain direction similar to the semi-quantitative analysis in the 1D case, the exponential factor in Eq. 5.11 can be written as

$$e^{i\frac{\omega}{c}\sqrt{(lb)^2+(md)^2}} = e^{i2\pi\sqrt{(l\frac{b}{\lambda})^2+(m\frac{d}{\lambda})^2}} \neq e^{i2\pi\pm\sqrt{(l\frac{b}{\lambda})^2\pm(m\frac{\delta}{\lambda})^2}}, (l \pm 0) \qquad (5.14)$$

Because of the existense of $l(b/\lambda)$ arising from the coupling between dimers belonging to different 1D chains, the oscillatory nature no longer exists.

We stress here that the oscillatory behavior revealed in the present sutdy for nanoshell dimer arrays should also be expected to exist in other related array structures, such as solid nanoparticle dimer arrasy considered in several recent studies [105,106]. We have chosen to focus on the nanoshell dimer arrasy as a class of examples in the present study, because their giant EM enhancement and additional tunability over that of solid nanoparticle arrays render them to be appealing templates for potential SERS applications with ultrasensitivity.

In principle, the oscillation period of 1D arrays can be tuned by varying the resonant frequency of the arrays and subsequently λ_{res}/δ. It was shown before that the resonant frequency of a 1D array depends on the aspect ratio fo the nanoshell with a gap dimension of $1nm$, as well as the inter-dimer spacing [105]. Therefore the geometric parameters, such as the aspect ratio fo the nanoshell and inter-dimer spacing, can be varied to tune the oscillation period of the 1D arrays.

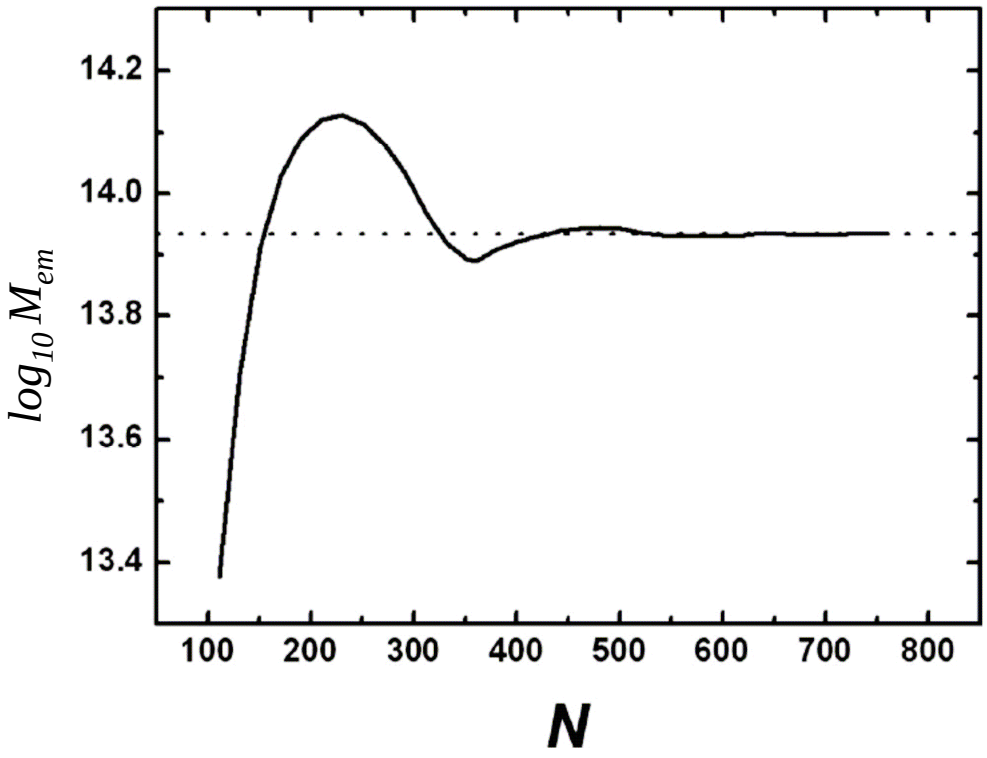

Figure 5.9: Variation of the EM enhancement with the total number of dimers in a dimer chain from a 2D nanoshell dimer array. The inter-dimer spacing d is $1020nm$, and the inter-array distance b is $720nm$. The resonant wavelength is $1028nm$. N refers to the total number of dimers ina chain of a particular 2D array.

Meanwhile, we note that our current study considers identical dimers in an array; while in experiments, inhomogeneities exist in the geometric parameters. Such inhomogeneities render $M_i(\omega)$, $\alpha(\omega)$ and the plasmon frequency of some dimers different from others, and as a result, the oscillation in $M_{em}(\omega)$ will exhibit some deviations from being periodic. Nevertheless, the primary feature, that there is an oscillatory dependence of the intensity enhancement on the array length, is expected to prevail, particularly when the geometrical fluctuations can be minimized as the state of the art of nanofabrication continues to advance.

Chapter 6

Perspective

6.1 Concurrent Multiscale Approach

As discussed in the previous Chapters, the systems involving different scales have become increasingly important. In SERS, for example, the nanoparticles have a typical dimension of tens of nanometers, while the Raman active molecule is usually less than $1nm$. When the nanoparticle and molecule form a complex system, any existing standalone approach, either in the classical or quantum regime, is restricted by one aspect or the other. So far, all the studies can only be qualitatively compared to experiments. The works presented in the previous chapters in this thesis followed an essentially sequential multiscale approach, which solves a hierachy of highly related model systems at different scales, and provides information of the physics at each scale.

On the other hand, concurrent multiscale approaches, which solve different parts of the complex system using different techniques and effectively couple them together, have emerged as promising tools to accurately describe the complex systems. For example, Lu *et al.* presented a multiscale modeling approach to concurrently couple quantum mechanical, classical atomistic, and continuum mechanical simulations in a unified fasion of metals [107]. My advisor and I proposed another concurrent multiscale approach to study dimer systems for SERS, with a molecule trapped in the nanogap of the dimer. The idea stems from the fact that since molecule is much smaller than the metal nanoparticles, the scattered EM field from the molecule is screened and will affect only

a small part of the nanoparticles. Thus we can still use classical EM techniques to describe the majority of the dimer, and use quantum mechanics to describe the molecule and small portion of the dimer near the nanogap, as illustrated in Fig. 6.1. The suitable quantum mechanical method for this problem is time-dependent density functional theory (TDDFT), which has the ability to calculate the optical response of a molecule attached to a few layers of metal atoms [108]. With the marching of the time, we only need to match the induced charge at the boundary separating the outer part of the dimer and the nanogap region, which serves as the boundary condition for both classical and quantum mechanical description.

6.2 Charge Transfer Model for Nanoparticle Dimers

Another intriguing work is to extend the charge transfer model describing the chemical effect for SERS to the nanoparticle dimer system, inspired by the single-molecule SERS. If the molecular vibration mode is polarized along the axis of the dimer, it will enhance the coupling with one particle while at the same time, weakens the coupling with the other. This process may induce a charge transfer from one nanoparticle to another through the molecule resonant level, which is expected to lead to consequences distinguished from the tranditional charge transfer process between only one nanoparticle and the molecule.

The key step would be to extend Persson's study [47] to paired metal substrates and only consider single resonant level for the molecule. The relative configuration is illustrated in Fig. 6.2. To incorporate the process mentioned above, we need not only to add additional terms to Persson's Hamiltonian (2.2), but also to consider the dependence of charge transfer term V_{ak} on the molecular vibration mode. The corresponding Hamiltonian is,

$$H = [\epsilon_a(Q) - edE_z]\hat{n}_a + \sum_{k_L} \epsilon_{k_L} a^+_{k_L} a_{k_L} + \sum_{k_R} \epsilon_{k_R} a^+_{k_R} a_{k_R} + \sum_{k_L} (V_{ak_L}(Q) a^+ a_{k_L} + h.c.)$$
$$+ \sum_{k_R} (V_{ak_R}(-Q) a^+ a_{k_R} + h.c.) + \hbar\Omega b^+ b + H_{EM} \tag{6.1}$$

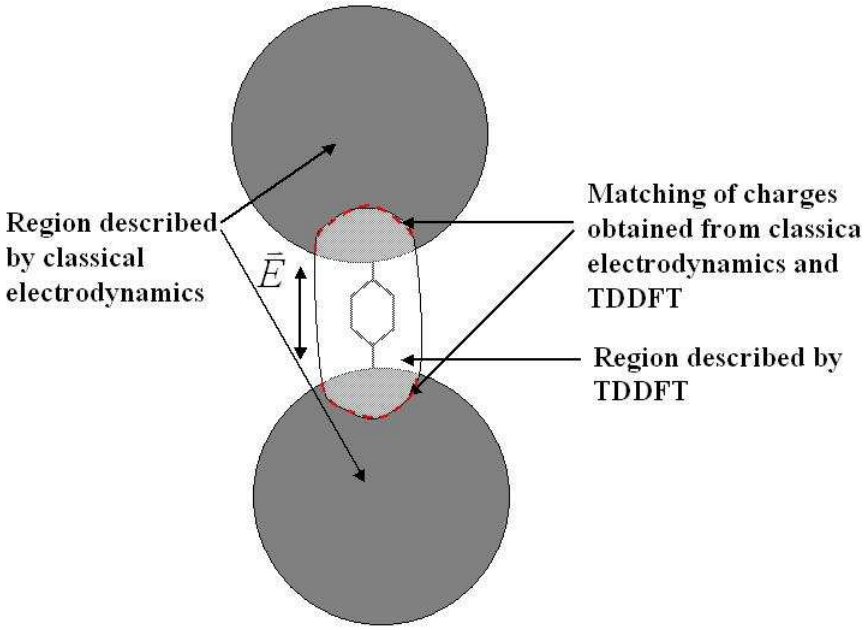

Figure 6.1: Illustration of concurrent multiscale approach for SERS. The two gray spheres represent nanoparticles, and a molecule is trapped in the gap region.

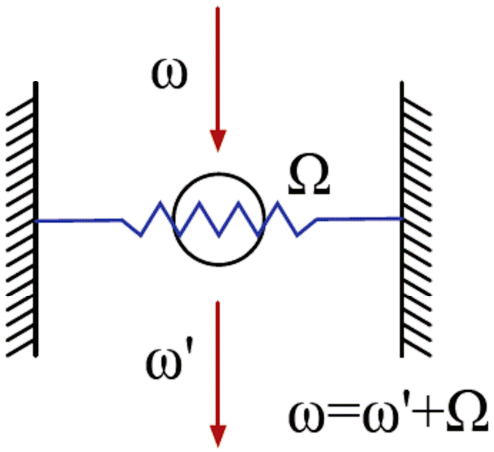

(a)

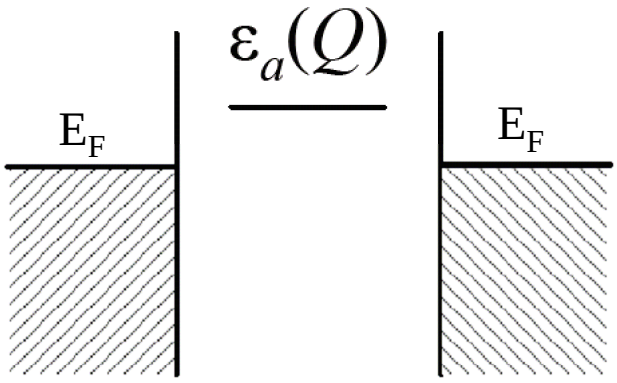

(b)

Figure 6.2: (a) Geometry of the model system with a molecule trapped between two metal substrates. The hollow circle represents the molecule, which has the normal mode with a frequency Ω. ω is the frequency of the incident light, while ω' is the frequency of the Raman scattered light (b) Energy level of the corresponding system. $\epsilon_a(Q)$ is the resonant energy level of the Raman active molecule, E_F is the fermi energy of the metal substrates (same for identical nanoparticles at the two sides).

where the L and R refer to the left and right side of the molecule.

6.3 Spin Polarized Transport and SERS

Another broad field that can be readily explored based on the series of studies in this thesis is the transport through nanoscale channels, such as quantum point contact [109] or molecular junction [110].

Quantum point contacts are structures (generally metallic) in which a 'neck' of atoms just a few atomic diameters wide (that is, smaller than or comparable to the conduction electrons' Fermi wavelength) bridges two electrical contacts. Such a system typically displays a conductance quantized in steps of $G_0 = 2e^2/h$ in the 'neck'. This universal value can be understood by the Landauer-Büttiker formula [111]. Fig. 6.3(a) shows the STM image and model of strands of atom chains suspended between electrodes that are pulled apart, while Fig. 6.3(b) shows the quantized conductance corresponding to different total number of strands [86]. This experiment verifies that the conductance of a single strand of atoms is $2e^2/h$ and that the conductance of a double strand is twice as large. On the other hand, the study of magnetic properties in Chapter 3 reveals a split of spin degree when two nanoparticles are close enough, which points out the possibility of generating spin-polarized current through the quantum point contact. Because the current is spin-polarized, the step of quantized conductance will change from G_0 to $G_0/2$ [111]. Similarly, the study in Chapter 4 implies that the step of quantized conductance can also be tuned by the strength of external electric field. Further microscopic phenomenologial modeling is expected for this investigation.

On the other hand, the conductance through molecular junctions not only have direct impact in the future molecular electronics, but also is related to SERS in a nanoparticle dimer. Their connection can be argued by the intimate relation between conductance G and dipole moment P, which characterizes the optical response in the Raman process. The phenomenological relation between G and P is that $G \propto \frac{dP}{dt}$, where t is time. Still, there are two different features between molecular junction transport and SERS, which deserve special attention in theoretical studies: one

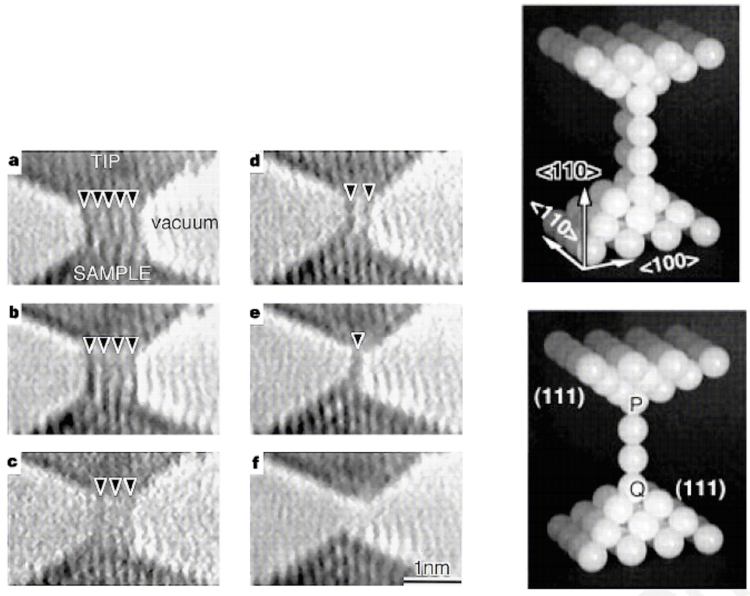

(a)

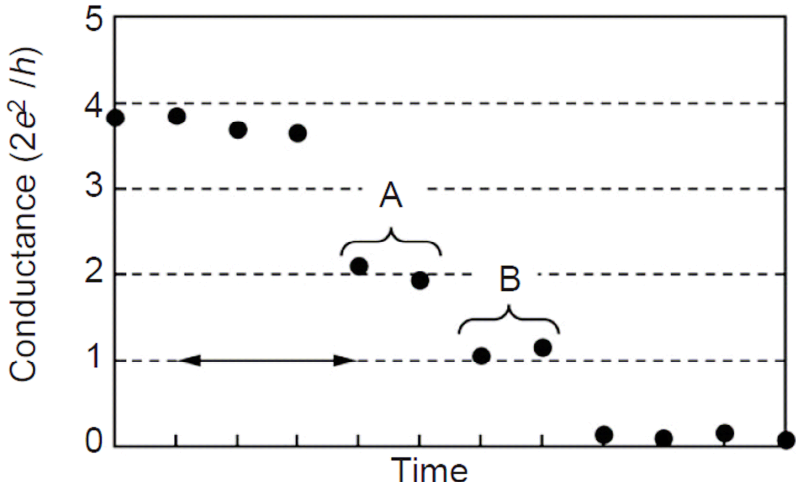

(b)

Figure 6.3: (a) Electron microscope images of a quantum point contact while withdrawing the tip. From **a** to **f**, the observation times are 0, 0.47, 1.23, 1.33, 1.80 and 2.17s, respectively. Dark lines indicated by arrowheads are strands of gold atoms. Models of single and double strand are shown to the right of the images. (b) Conductance change of a contact while withdrawing the tip.

is that SERS uses optical frequency electromagnetic excitation, while molecular transport normally uses dc or low frequency voltage; second is that SERS needs to consider the atomic movement in the molecule, while atoms are spatially fixed in molecular transport. The simultaneous consideration of SERS and nanoscale transport is expected to reveal their correlations and possibly point out new directions in both fields.

Chapter 7

Conclusions

Along the study of low-dimensional metal systems across different scales, my colleagues and I investigated electronic, optical and magnetic properties of nanoparticles and surfaces, using a variety of methods, including microscopic phenomenological model study, *ab initio* density functional theory and classical electromagnetics.

Using microscopic phenomenological model, we discovered a new mechanism for the chemical contribution to SERS, where the SERS intensity is determined by the parallel electric field. We have shown that the modulation of the polarizability of a small metal nanoparticle by the vibrational motion of an adsorbed molecule may enhance the Raman scattering by a factor of $\sim 10^2$. For adsorbates on a flat metal surface, the Raman scattering using the s-polarized field can be even more strongly enhanced and reach a factor $\sim 10^4$.

We also used *ab initio* DFT method to study the electronic coupling between two small silver nanoparticles, which are building blocks of nanoparticle aggregates. we have shown that the electronic coupling between two metal nanoparticles depends strongly on both the gap size and the relative orientation of the nanoparticles. As the gap size increases from touching contact, the dimer undergoes a bond-breaking step, which establishes the striking existence of an OGS for static polarizability. Moreover, depending on the particle size and orientation, the electronic coupling before the bond breaking can be strong enough to give rise to a net magnetic moment of the dimer,

even though the isolated particles are nonmagnetic. These findings may prove to be instrumental in understanding and controlling the optical, magnetic, electrical, and chemical properties of closely-packed nanoparticle aggregates.

While the above study was in the linear electric response regime, we also carried out a study in the nonlinear regime. We have shown that the strong electric field energy, which renders the dimer to enter nonlinear regime, is produced by either a strong field or large gap size of the dimer. The transition to the nonlinear regime emerges when the HOMO-LUMO gap is decreased by strong field energy to a certain limit. Also, the magnetic response of the dimer to the electric field is dramatically different when the system changes into the nonlinear regime. In the nonlinear regime, the net moment of the dimer can be tuned by the electric field, while in the linear regime, only a constant value occurs. Therefore, the electric field provides a new variable to tune the physical properties of nanomaterials. Our study may be enlightening to a variety of physical properties related to the nonlinear effects of nanoparticle aggregates.

At larger scales when the nanoparticles have the dimension comparable to those used in experiments, we studied the optical properties of ordered 1D arrays of silver nanoshell dimers using Mie theory, which is basically classical electromagnetics. We showed that the EM contribution to SERS can be as high as $\sim 4.5 \times 10^{13}$ for nanoshell dimer arrays with optimal geometry when additional broadening due to electron-interface scattering is not significant. The extraordinarily high enhancement is attributed to a long-range collective photonic effect associated with the array structure, constructively superposed onto the intrinsic enhancement associated with an isolated nanoshell dimer. The high EM enhancement, the large hot volume, and the sensitive tunability in the resonance frequency make such nanoshell array structures highly desirable templates for single molecule spectroscopy.

Combing Mie theory and coupled dipole approximation, we also discovered that huge EM enhancement oscillates nearly periodically with the length of a 1D nanoshell dimer array, and for an array of a fixed length the EM enhancement also oscillates along the array, but with a different periodicity. Both types of oscillations can be attributed to the interference effect of the dynamic dipole fields from different dimers within the array. The finite size effects in the optical properties

of nanoshell dimer arrays are expected to exist in other related array systems, and this finding should be instrumental in future design of SERS-active substrates with ultrhigh sensitivity.

When generalized to 2D arrays, EM enhancement higher than that of the 1D arrays can be obtained, and the constant magnitude of $\sim 10^{14}$ is advantageous to experimental realization of single-molecule SERS.

Bibliography

Bibliography

[1] M. Moskovits, Rev. Mod. Phys. **57**, 783 (1985).

[2] J. M. Pitarke, V. M. Silkin, E. V. Chulkov, and P. M. Echenique, Rep. Prog. Phys. **70**, 1 (2007).

[3] A. V. Zayats and I. I. Smolyaninov, J. Opt. A: Pure Appl. Opt. **5**, S16 (2003).

[4] M. Pelton, J. Aizpurua, and G. Bryant, Laser & Photon Rev. 2 **3**, 136 (2008).

[5] J. K. Norskov, T. Bligaard, J. Rossmeisl, and C. H. Christensen, Nature Chem. **1**, 37 (2009).

[6] M. Law, J. Goldberger, and P. D. Yang, Annu. Rev. Mater. Res. **34**, 83 (2004).

[7] A. N. Shipway, E. Katz, and I. Willner, ChemPhysChem **1**, 18 (2000).

[8] A. Campion, J. E. Ivanecky III, C. M. Child, and M. Foster, J. Am. Chem. Soc. **117**, 11807 (1995).

[9] P. Kambhampti, C. M. Child, and A. Campion, J. Chem. Soc. Faraday Trans. **92**, 4775 (1996).

[10] P. Kambhampti, C. M. Child, M. C. Foster, and A. Campion, J. Chem. Phys. **108**, 5013 (1998).

[11] H. Kuninaka and H. Hayakawa, Phys. Rev. E **79**, 031309 (2009)

[12] G. Mie, Ann. Phys. **25**, 377 (1908).

[13] S. N. Khanna and P. Jena, Phys. Rev. Lett. **69**, 1664 (1992).

[14] C. P. Collier, R. J. Saykally, J. J. Shiang, S. E. Henrichs, and J. R. Heath, Science. **277**, 1978 (1997).

[15] I. Grigorenko, S. Haas, A. Balatsky, and A. F. J. Levi, New. J. Phys. **10**, 043017 (2008).

[16] M. P. Marder, *Solid State Physics*, 1st Edition, Wiley, New York, 2000.

[17] W. L. Barnes, A. Dereux, and T. W. Ebbesen, Nature **424**, 824 (2003).

[18] M. Moskovits, J. Raman Spectrosc. **36**, 485 (2005).

[19] D. Pissuwan, S. M. Valenzuela, and M. B. Cortie, Trends Biotechnol. **24**, 62 (2006).

[20] T. Kalkbrenner, *et al.*, Phys. Rev. Lett. **95**, 200801 (2005).

[21] S. C. Kiston, W. L. Barnes, and J. R. Sambles, Phys. Rev. Lett. **77**, 2670 (1996).

[22] W. L. Barnes, T. W. Priest, S. C. Kiston, and J. R. Sambels, Phys. Rev. B **54**, 6227 (1996).

[23] W. L. Barnes, S. C. Kiston, T. W. Priest, and J. R. Sambels, J. Opt. Soc. Am. A **14**, 1654 (1997).

[24] S. Kawata, A. Ono, and P. Verma, Nat. Photonics **2**, 438 (2008).

[25] E. Kretschmann and H. Raether, Z. Naturforsch A. **23**, 2135 (1968).

[26] A. Otto, Z. Phys. **216**, 398 (1968).

[27] H. Ditlbacher, Appl. Phys. Lett. **80**, 404 (2002).

[28] R. H. Ritchie, E. T. Arakawa, J. J. Cowan, and R. N. Hamm, Phys. Rev. Lett. **21**, 1530 (1968).

[29] H. J. Weber and G. B. Arfken, *Mathematical Methods for Physicists*, 6th Edition, Academic Press, 2006.

[30] P. Nordlander, C. Oubre, E. P. Prodan, K. Li and M. I. Stockman, Nano Lett. **4**, 899 (2004).

[31] E. P. Prodan, C. Radloff, N. J. Halas, P. Nordlander, Science **302**, 419 (2003).

[32] C. E. Talley *et al.*, Nano Lett. **5**, 1569 (2005).

[33] T. Atay, J.-H. Song, and A. V. Nurmikko, Nano Lett. **4**, 1627 (2004).

[34] J. Zuloaga, E. Prodan, and P. Nordlander, Nano Lett. **9**, 887 (2009).

[35] D. J. Gardiner and P. R. Graves, *Practial Raman Spectroscopy*, 1st Edition, Springer, New York, 1989.

[36] D. A. Long, Proc. R. Soc. London, Ser. A **217**, 203 (1953).

[37] M. Fleischmann, P. J. Hendra, and A. J. Mcquillan, Chem. Phys. Lett. **26**, 163 (1974).

[38] D. L. Jeanmaire and R. P. Van Duyne, Electroanal. Chem. **84**, 1 (1977).

[39] K. Kneipp, Y. Wang, H. Kneipp, L. T. Perelman, and I. Itzkan, Phys. Rev. Lett. **78**, 1667 (1997).

[40] S. Nie and S. R. Emory, Science 275, 1102 (1997).

[41] A. M. Michaels, M. Nirmal, and L. E. Brus, J. Am. Chem. Soc. **121**, 9932 (1999).

[42] H. X. Xu, E. J. Bjerneld, M. Kall, and L. Borjesson, Phys. Rev. Lett. 83, 4357 (1999).

[43] H. X. Xu, J. Aizpurua, M. Kall, and P. Apell, Phys. Rev. E 62, 4318 (2000).

[44] P. C. Waterman, Phys. Rev. D **3**, 825 (1971).

[45] D. W. Mackowski, J. Opt. Soc. Am. A **11**, 2851 (1994).

[46] A. Taflove and S. C. Hagness, *Computational Electrodynamics: The Finite-Difference Time-Domain Method*, 3rd Edition, Artech House Publishers, 2005.

[47] B. N. J. Persson, Chem. Phys. Lett. **82**, 561 (1981).

[48] M. P. Marder, *Condensed Matter Physics*, Wiley-Interscience Publishers, 2000.

[49] J. R. Lombardi, R. L. Birke, T. H. Lu, and J. Xu, J. Chem. Phys. **84**, 4174 (1986).

[50] F. J. Adrian, J. Chem. Phys. **77**, 5302 (1982).

[51] E. Zaremba and B. N. J. Persson, phys. Rev. B **35**, 596 (1987).

[52] B. N. J. Persson, Surf. Sci. **281**, 153 (1997).

[53] B. N. J. Persson, J. Chem. Phys. **98**, 1659 (1993).

[54] D. Schmeisser, J. E. Demuth, and Ph. Avouris, Chem. Phys. Lett. **87**, 324 (1982).

[55] J. E. Demuth, D. Schmeisser, and Ph. Avouris, Phys. Rev. Lett. **47**, 1166 (1981).

[56] B. N. J. Persson, Phys. Rev. B **44**, 3277 (1991).

[57] Z. Y. Zhang and D. C. Langreth, Phys. Rev. B **39**, 10028 (1989).

[58] C. J. Hirschmugl *et al.*, Phys. Rev. Lett. **65** 480 (1990).

[59] A. M. Michaels, J. Jiang, and L. Brus, J. Chem. Phys. B **104**, 11965 (2000).

[60] J. Jiang, K. Bosnick, M. Maillard, and L. Brus, J. Chem. Phys. B **107**, 9964 (2003).

[61] M. Danckwerts and L. Novotny, Phys. Rev. lett. **98**, 026104 (2007).

[62] J. B. Lassiter *et al.*, Nano Lett. **8**, 1212 (2008).

[63] G. Schedelbeck, W. Wegscheider, M. Bichler, G. Abstreiter, Science **278**, 1792 (1997).

[64] P. Howard, A. Andreev, and D. A. Williams, Phys. Stat. Sol. (c) **5**, 3156 (2008).

[65] K. Zhao, M. C. Troparevsky, D. Xiao, A. G. Eguiluz, and Z. Y. Zhang, Phys. Rev. Lett. **102**, 186804 (2009).

[66] P. Kohenberg and W. Kohn, Phys. Rev. **136**, B864 (1964); W. Kohn and L. J. Sham, Phys. Rev. **140**, A1133 (1965).

[67] G. D. Mahan, *Many-Particle Physics*, 1st Edition, Plenum Press, New York 1981.

[68] D. M. Ceperley, Phys. Rev. B **18**, 3126 (1978); D. M. Ceperley and B. J. Alder, Phys. Rev. Lett. **45**, 566 (1980).

[69] J. C. Phillips and L. Kleinman, Phys. Rev. **116**, 287 (1959).

[70] A. Zunger, in *Quantum Theory of real Materials* edited by J. R. Chelikowsky and S. G. Louie, Kluwer Academic Publishers, Boston 1996.

[71] G. P. Kerker, J. Phys. C **13**, L189 (1980).

[72] D. R. Hamann, M. Schlüter and C. Chiang, Phys. Rev. Lett. **43**, 1494 (1979).

[73] D. Vanderbilt, Phys. Rev. B **32**, 8412 (1985).

[74] G. B. Bachelet, D. R. Hamann, and M. Schlüter, Phys. Rev. B **26**, 4199 (1982).

[75] N. Troullier and J. L. Martins, Phys. Rev. B **43**, 1993 (1991).

[76] W. Andreoni, in *The chemical Physics of Atomic and Molecular Clusters*, edited by G. Scoles, North-Holland, Amsterdam, 1990.

[77] G. D. Smith, *Numerical Solutions of Partial Differential Equations: Finite Difference Method*, 2nd Edition, Oxford, New York 1978.

[78] B. Fornberg and D. M. Sloan, *Acta Numerica*, 1994

[79] J. R. Chelikowsky, N. Troullier, and Y. Saad, Phys. Rev. Lett. **72**, 1240 (1994).

[80] J. R. Chelikowsky, N. Troullier, K. Wu, and Y. Saad, Phys. Rev. B **50**, 11355 (1994).

[81] M. P. Marder, *Condensed Matter Physics*, 1st Edition, Wiley, New York 2000.

[82] M. Kiguchi, R. Stadler, I. S. Kristensen, D. Djukic, and J. M. van Ruitenbeek, Phys. Rev. Lett. **98**, 146802 (2007).

[83] M. Strange, K. S. Thygesen, J. P. Sethna, K. W. Jacobsen, Phys. Rev. Lett. **101**, 096804 (2008).

[84] S. Ke, H. U. Baranger, and W. Yang, J. Chem. Phys. **126**, 201102 (2007).

[85] Y. Dakhnovskii, R. Bavli, and H. Metiu, Phys. Rev. B **53**, 4657 (1996).

[86] H. Ohnishi, Y. Kondo, and K. Takayanagi, Nature **395**, 780 (1998).

[87] K. Uchida, *et al.*, J. Opt. Soc. Am. B **11**, 1236 (1994).

[88] W. Chen and D. L. Mills, Phys. Rev. B **35**, 524 (1987).

[89] **Editorial**, Nat. Mater. **6**, 1 (2007).

[90] S.-W. Cheong and M. Mostovoy, Nat. Mater. **6**, 13 (2007).

[91] K.-H. Su, Q.-H. Wei, X. Zhang, J. J. Mock, D. R. Smith, and S. Schultz, Nano Lett. **3**, 1087 (2003).

[92] Y. Lei and W.-K. Chim, J. Am. Chem. Soc. **127**, 1487 (2005).

[93] W. Wang and B. H. Gu, Appl. Spectrosc. **59**, 1509 (2005).

[94] P. K. Jain and M. A. El-Sayed, Nano Lett. **7**, 2854 (2007).

[95] P. K. Jain, W. Huang, and M. A. El-Sayed, Nano Lett. **7**, 2080 (2007).

[96] W. Huang, W. Qian, P. K. Jain, and M. A. El-Sayed, Nano Lett. **7**, 3227 (2007).

[97] K. H. Fung and C. T. Chan, Opt. Lett. **32**, 973 (2007).

[98] L. L. Zhao, K. L. Kelly, and G. C. Schatz, J. Phys. Chem. B **107**, 7343 (2003).

[99] J. Sinzig and M. Quinten, Appl. Phys. A **58**, 157 (1994).

[100] O. R. Cruzan, Q. Appl. Math. **20**, 33 (1962).

[101] P. B. Johnson and R. W. Christy, Phys. Rev. B **6**, 4370 (1972).

[102] C. L. Nehl, N. K. Grady, G. P. Goodrich, F. Tam, N. J. Halas, and J. H. Hafner, Nano Lett. **4**, 2355 (2004).

[103] H. X. Xu, Appl. Phys. Lett. **87**, 066101 (2005).

[104] U. Kreibig and M. Vollmer, *Optical Properties of Metal Clusters*, 1st Edition, Springer, New York 1995.

[105] K. Zhao, H. X. Xu, B. H. Gu, and Z. Y. Zhang, J. Chem. Phys. **125**, 081102 (2006).

[106] S. L. Zou and G. C. Schatz, Chem. Phys. Lett. **403**, 62 (2005).

[107] G. Lu, E. B. Tadmor, and E. Kaxiras, Phys. Rev. B **73**, 024108 (2006).

[108] E. Runge and E. K. U. Gross, Phys. Rev. Lett. **52**, 997 (1984).

[109] R. A. Webb, S. Washburn, C. P. Umbach, and R. B. Laibowitz, Phys. Rev. Lett. **54**, 2696 (1985).

[110] M. A. Reed, C. Zhou, C. J. Muller, T. P. Burgin, and J. M. Tour, Science **278**, 252 (1997).

[111] H. Bruus and K. Flensberg, *Many-Body Quantum Theory in Condensed Matter Physics: An Introduction*, illustrated edition Edition, Oxford University Press, USA, 2004.

Appendix

Appendix

Publications:

1. M. Claudia Troparevsky, Ke Zhao, Di Xiao, Zhenyu Zhang, and Adolfo G. Eguiluz, "Tunability of the Magnetic Properties of Metal Nanoparticle Dimers in a Nonlinear Dielectric Response Regime", to be submitted to Nano Lett.

2. Ke Zhao, M. Claudia Troparevsky, Di Xiao, Adolfo G. Eguiluz, and Zhenyu Zhang, Phys. Rev. Lett. **102**, 186804 (2009). "Electronic coupling and optimal gap size between two metal nanoparticles".

3. Youlin Song, Ke Zhao, Yu Jia, Xing Hu, and Zhenyu Zhang, J. Chem. Phys. **129**, 204506 (2008). "Finite size effects on the electromagnetic field enhancement from low-dimensional silver nanoshell dimer arrays".

4. Bo N. J. Persson, I. M. Sivebaek, V. N. Samoilov, Ke Zhao, A. I. Volokitin, Zhenyu Zhang, J. Phys. Condens. Matter **20**, 395006 (2008). "On the origin of Amonton's friction law".

5. Ke Zhao, Hongxing Xu, Baohua Gu, and Zhenyu Zhang, J. Chem. Phys. **125**, 081102 (2006). "One-dimensional arrays of nanoshell dimers for single molecule spectroscopy via surface-enhanced raman scattering".

6. Bo N. J. Persson, Ke Zhao, and Zhenyu Zhang, Phys. Rev. Lett. **97**, 199702 (2006). Comment on "Chemical contribution to surface-enhanced Raman scattering"- reply.

7. Bo N. J. Persson, Ke Zhao, and Zhenyu Zhang, Phys. Rev. Lett. **96**, 207401 (2006). "Chemical contribution to surface-enhanced Raman scattering".

Vita

Ke Zhao was born at Nanjing, China on Dec. 30, 1980. After graduating from Jinling high school, he entered department of physics, Nanjing University at Nanjing, where he spent four years as an undergraduate student and one year as a graduate student. In January of 2004, he came to the University of Tennessee to pursue Ph.D in physics. He started as a teaching assistant, and in fall of 2004, he joined Prof. Zhenyu Zhang's group to work on a series of thesis projects. He completed his Doctor of Philosophy degree in 2009.